UNIVERSITY OF CALIFORNIA

Santa Barbara

The Late Quaternary Evolution of the Southern California Coast: Sea-Level Change, Storms, and Subsidence

A dissertation submitted in partial satisfaction of the

requirements for the degree Doctor of Philosophy

in Geological Sciences

by

Laura Conners Reynolds

Committee in charge:

Professor Alexander R. Simms, Chair

Professor Lorraine Lisiecki

Professor Edward Keller

March 2018

The dissertation of Laura Conners Reynolds is approved.

_____

Lorraine Lisiecki

_____

Edward Keller

_____

Alexander Simms, Committee Chair

January 2018

ACKNOWLEDGEMENTS

This document can only begin to capture the knowledge and experience gained over the course of a PhD, as I can only begin to thank the individuals and communities that have facilitated my research and personal growth. I would like to start by thanking the extraordinary community of the UCSB Earth Science Department. It has been a joy to learn from and work with the warm, gregarious staff, students, and faculty these past five years.

I was fortunate enough to receive funding for my studies and research from the National Science Foundation (Graduate Research Fellowship Program DGE-1144085, Graduate Research Opportunities Worldwide), the Southern California Earthquake Center, the Santa Barbara Long Term Ecological Research project, the UCSB Earth Research Institute, and the UC Natural Reserve System (UCNRS) Mildred Mathias Graduate Research Grant. This research could not have been accomplished without this generous support.

My research has been built on the foundation of other scientists who have studied Carpinteria Marsh and the surrounding region, including Wayne Ferren, Robert Yeats, and many others. Thank you to Andy Brooks and the rest of the UC Natural Reserve System staff for allowing access to the reserve. Thanks also to the folks who live along Sand Point Road, who have let me tramp around their backyards for many years without complaint.

I would like to thank my collaborators, especially Ana Ejarque, Scott Anderson, Tom Rockwell, and Yusuke Yokoyama for their insight, patience, and encouragement through many (many) iterations of the Carpinteria manuscripts. I would also like to thank my various committee members Ed Keller, Lorraine Lisiecki, and David Lea, who have helped me think more expansively and critically about my research.

I would also like to thank the Simms lab for wading/crawling through muck to collect my cores, helping to (continuously) rehab and improve lab and field gear, and always

challenging and inspiring me to be a better scientist and teacher. Special thanks to my academic siblings Lauren Simkins, Daniel Livsey, Baird King, Elisabeth Steel, Julie Zurbuchen, and Zack Nelson.

I am incredibly grateful for the support of my adviser, Alex Simms. For five years, he has consistently demonstrated the kind of creativity, integrity, and work ethic I hope to emulate as a scientist, as well as a regular person. I couldn't have asked for a better adviser and mentor.

And finally, my family. To my mother, Kathleen Conners, thank you for encouraging curiosity in whatever odd, messy direction it took me, and for teaching me how to speak up and lean in. To my father, Michael Reynolds, thank you for teaching me how to be a useful contrarian, and showing me the puns and poetry written into the fabric of daily life. And to my sister, Kara Reynolds, my friend and first teacher: I would still be writing my z's backwards if it weren't for you, and then where would I be? To all my loving family, anything I accomplish in this life belongs as much to you as it does to me.

Lastly, strange as it may seem, I'd like to thank my little marsh, and all its critters I have (temporarily) disturbed over the last few years during fieldwork. Thank you for allowing me to steal a bit (okay, a lot) of your mud to decipher the incredible changes you've been witness to over the last 7000 years. I hope I've done your story justice, and I'm looking forward to the work of future graduate students, and the many stories yet to be unearthed.

VITA OF LAURA CONNERS REYNOLDS

January, 2018

EDUCATION

2018
University of California, Santa Barbara, CA
Ph.D. in Geological Sciences
Adviser: Dr. Alexander Simms
Thesis: The Late Quaternary Evolution of the Southern California Coast: Sea-Level Change, Storms, and Subsidence

2011
Dartmouth College, Hanover, NH
B.A. in Earth Sciences, cum laude; English (Creative Writing) Minor
Adviser: Dr. Meredith Kelly
Honors Thesis: Pollen, charcoal, and macrofossil analysis of the Occom Pond core and surficial geology of the surrounding area.

ACADEMIC PUBLICATIONS

Reynolds, L.C., Simms, A.R., Ejarque, A., King, B., Anderson, R.S., Carlin, J., Bentz, R.M., Rockwell, T.K., Peters, R (2018). Coastal Flooding and the 1861-2 California Storm Season. *Marine Geology*, in press.

Reynolds, L.C., Simms, A.R., Rockwell, T.K., Yokoyama, Y., Mijairi, Y., Hangsterfer, A. Holocene coseismic subsidence along a non-subducting active margin. Submitted.

Simms, A. R., **Reynolds, L. C.**, Bentz, J. M., Roman, A., Rockwell, T. K., & Peters, R. B. (2016). Tectonic subsidence of California estuaries increases forecasts of relative sea-level rise. *Estuaries and Coasts*. SCEC Contribution 6020

Reynolds, L.C., and Simms, A.R. (2015). Late Quaternary relative sea level in Southern California and Monterey Bay. *Quaternary Science Reviews* 126: 57-66. PDF 10.1016/j.quascirev.2015.08.003

Holmquist, J., **Reynolds, L.**, Brown, L., Southon, J., Simms, A.R., and MacDonald, G. (2015). Marine radiocarbon reservoir values in southern California estuaries: interspecies, latitudinal, and interannual variability. *Radiocarbon* 57: 449-458. PDF 10.2458/azu_rc.57.18389

NONACDEMIC PUBLICATIONS

Reynolds, L.C. (2017). Ancient wildfires suggest rising atmospheric oxygen helped end past ocean anoxia (https://www.earthmagazine.org/article/ancient-wildfires-suggest-rising-

atmospheric-oxygen-helped-end-past-ocean-anoxia). *EARTH Magazine,* American Geosciences Institute.

Reynolds, L.C. (2017). Extinct lunar magnetic field lasted longer than previously thought (https://www.earthmagazine.org/article/extinct-lunar-magnetic-field-lasted-longer-previously-thought). *EARTH Magazine,* American Geosciences Institute.

Reynolds, L., Livsey, D., Simms, A. (2012) Stories in Mud: Pamphlet prepared for the Coastal Bend Bays and Estuaries Program for use in K-12 field trips along the Corpus Christi, TX bayhead delta.

TEACHING EXPERIENCE

2017
Associate Instructor (Fall Term): Sedimentology and Stratigraphy (Earth 122)
Associate Instructor (Spring Term): The Geology of California (Earth 109)
2015
Associate Instructor (Spring Term): Introduction to Oceanography (Earth 4)
2014
Teaching Assistant (Winter Term): Antarctica (Earth 10)
2013
Teaching Assistant (Summer Term): Summer Field Geology (Earth 118)
Teaching Assistant (Spring Term): Coastal Processes and Management (ENVS 134)
Teaching Assistant (Winter Term) History of Life (Earth 30)
2012
Teaching Assistant (Fall Term): Dinosaurs (Earth 7)
Environmental Educator (Spring), Seacoast Science Center, Rye, NH
2011
Environmental Educator (Fall), Casper Mountain Science School, Casper, WY
Teaching Assistant (Summer): Dynamic Earth, John Hopkins Center for Talented Youth, Palo Alto, CA
2010
Teaching Assistant (Summer): Dynamic Earth, John Hopkins Center for Talented Youth, Palo Alto, CA
Science Mentor (Winter), Montshire Museum of Science, Norwich, VT
2009
Education Intern (Spring), Montshire Museum of Science, Norwich, VT

GRANTS AND AWARDS

NSF Graduate Research Fellowship (2013-2016)
NSF GROW/JSPS Fellowship for Research at the Atmospheric and Ocean Science Research Institute, the University of Tokyo (2016)
G.K. Gilbert Award, UC Santa Barbara (2106)
Lloyd and Mary Edwards Field Studies Fellowship, UC Santa Barbara (2016)
Outstanding Student Paper Award, AGU Annual Meeting (2015)
Graduate Student Opportunity Award, UC Santa Barbara (2015)

Global Field Travel Fund, UC Santa Barbara (2015)
Association for Women Geologists Takken Student Research Presentation Travel Award (2014)
Alumni Graduate Award for Research Excellence (2014, 2017)
Mildred E. Mathias Graduate Student Research Grant (2013)
Fellowship on Hazards (California Institute for Research on Hazards) (2013)
Graduate Student Opportunity Award, UC Santa Barbara (2013)
High Honors, Earth Sciences, Dartmouth College (2011)
Upham Geology Award for thesis research, Dartmouth College (2011)
Grimes Prize for English, Dartmouth College (2011)
Dean of Faculty Research Grants (John Lindsley Fund Grant; Class of '86 Research Award Grant), Dartmouth College (2011)

INVITED TALKS

Evidence for Holocene Coseismic Subsidence Along the Rincon Creek Fault, Carpinteria, California, Coast Geological Society, Ventura, California, September, 2017.

Coastal Hazards in the Sedimentary Record: Megafloods of California's Past, Cal Poly Pamona, May, 2016.

Geology of Carpinteria Valley, Parks Department Docent Training Program, Carpinteria, California, February, 2015.

PROFESSIONAL AND OTHER SERVICE

Mentor, UCSB Earth Science Undergraduate Honors Thesis student (2017-2018)
Mentor, Santa Barbara Channel Long Term Ecological Research undergraduate REU student (2015)
Mentor, UCSB Materials Research Laboratory Research Experience for Teachers Program (2014)
Education and Outreach Co-Chair, Women in Science and Engineering (WiSE), University of California Santa Barbara (2014-2016)
Organizer, Alumni Career Panel, UC Santa Barbara Department of Earth Sciences (2014)
Graduate Student Faculty Liaison, UC Santa Barbara Department of Earth Sciences (2014)
Organizer, Earth Science Weekly Seminar, UC Santa Barbara Department of Earth Sciences (2013-4, 2015-6)
Academic Coach, Summer Enrichment At Dartmouth (SEAD) Program (2009)

PROFESSIONAL MEMBERSHIPS: AAAS, GSA, AGU, SEPM, AWG, CGS, Sigma Xi

FIELD COURSES/WORKSHOPS ATTENDED

POLENET Glacial Isostatic Adjustment Training School (2015)
SciFnd Challenge, online science outreach class (2014)
University of California Santa Barbara Field Trip to Iceland (2014)

Communicating Science to the Public Workshop, University of California Santa Barbara (2014)
Friends of the Pleistocene Field Trip to Laguna Salada, Baja Mexico (2014)
Dartmouth Earth Science Department Field Program in the Western U.S. (2009)

FIELD EXPERIENCE

Sediment core extraction, seismic data collection, ground-penetrating radar data collection, outcrop analysis, glacial surficial geological mapping. Field work performed in the Connecticut River Valley, New Hampshire; Northern and Southern coastal California; Channel Islands, California; Corpus Christi, Texas; and Anza Borrego Desert, California.

CONFERENCE ABSTRACTS

Lead author:
Reynolds, L.C., Simms, A.R., Rockwell, T.K., Yokoyama, Y., Mijairi, Y., Hangsterfer, A. (2017) Evidence for Holocene coseismic subsidence during a non- plate boundary earthquake. American Geophysical Union Annual Meeting, New Orleans, Louisiana., December, 2017.

Reynolds, L. C., Simms, A. R., Ejarque, A., King, B.L., Anderson, R.S., Carlin, J.A., Bentz, J. M., Rockwell, T. K., Peters, R. B. (2017) Variability in sedimentation rates in southern Californian estuaries from the late Holocene through the Anthropocene, Coastal and Estuarine Research Federation, Providence, Rhode Island, October, 2017.

Reynolds, L.C., Simms, A.R., Rockwell, T.K., Yokoyama, Y., Mijairi, Y., Hangsterfer, A. (2017) Holocene coseismic subsidence along a non-subducting active margin. *Southern California Earthquake Center Annual Meeting*, Palm Springs, CA, Sept. 2017.

Reynolds, L.C., Simms, A.R., Rockwell, T., Peters, R. (2016), Terrestrial Evidence for Holocene Pluvials in Coastal Southern California , American Geophysical Union Annual Meeting, San Francisco, Calif., December, 2016.

Reynolds, L.C., Simms, A.R., Carlin, J., (2016) Sedimentary Record of Recent Flood Events from Sauces Canyon, Santa Cruz Island, California, GSA Cordilleran Meeting, Ontario, CA, April, 2016.

Reynolds, L.C., Simms, A.R., Carlin, J. (2016) Sedimentary Record of Recent Flood Events From Sauces Canyon, Santa Cruz Island, California, University of California Natural Reserve System Mathias Symposium, Bodega Bay, California, March, 2016.

Reynolds, L.C., Truong, M., Ejarque, A., Simms, A.R., Anderson, S., (2015) Dating historical sediments in estuaries: A multi-proxy approach, American Geophysical Union, San Francisco, CA, December, 2015.

Reynolds, L.C., Simms, A.R., Rockwell, T.K., Peters, R. (2015) Holocene Evolution of Carpinteria Marsh, Southern California: Storms and Subsidence. Poster Presentation, Southern California Earthquake Center Annual Meeting, Palm Springs, CA, Sept. 2015.

Reynolds, L.C., Simms, A.R., (2015) Holocene Sea Level History for Southern California and Elkhorn Slough, INQUA International Congress XIX, Nagoya, Japan, July, 2015.

Reynolds, L.C., Simms, A.R., Rockwell, T.K., Peters, R., (2015) Holocene Evolution of Carpinteria Marsh, Southern California: A Story of Storms and Subsidence, INQUA International Congress XIX, Nagoya, Japan, July, 2015.

Reynolds, L.C., Simms, A.R. (2015) Holocene Relative Sea Level in Southern California: Implication for Estimations of Recent Tectonic Rates on the Coast, Oral Presentation, PSAAPG, Oxnard, CA, May 2015.

Reynolds, L.C., Simms, A.R., Rockwell, T.K., Peters, R. (2015) Holocene Evolution of Carpinteria Marsh, Southern California: Evidence for Subsidence, Oral Presentation, Seismological Society of America Annual Meeting, Pasadena, CA, April 2015.

Reynolds, L.C. Simms, A.R., (2014) Holocene Relative Sea Level History for Southern and Central California, Oral Presentation, Geological Society of America Annual Meeting, Vancouver, CA, October, 2014.

Reynolds, L.C., Simms, A.R., Peters, R., Rockwell, T.K. (2013) Evidence of Subsidence Events along the Rincon Creek Fault in Carpinteria Marsh, Poster, Southern California Earthquake Center Annual Conference, Palm Springs, September, 2013.

Reynolds, L.C., Holmquist, J.R, Brown, L.N., Southon, J.R., Simms, A.R., MacDonald, G.M., (2014) Radiocarbon Reservoir Variability in California Estuaries, Oral Presentation, Radiocarbon in the Environment, Belfast, U.K., August, 2014.

Reynolds, L.C., Simms, A.R., King, B.L., Peters, R., Rockwell, T., Ejarque, A., Anderson, S., (2013), Sedimentological Evidence of the 1812 Santa Barbara Tsunami in Carpinteria Marsh, CA, Abstract 1808899, American Geophysical Union Annual Meeting, San Francisco, Calif., December, 2013.

Reynolds, L.C., Simms, A.R., King, B.L., Peters, R., Rockwell, T.K., Ejarque, A., Anderson, S., (2013) Sedimentological Evidence of the 1812 Santa Barbara Tsunami in Carpinteria. Abstract, Southern California Earthquake Center Annual Conference, Palm Springs, September, 2013.

ABSTRACT

The Late Quaternary Evolution of the Southern California Coast: Sea-Level Change, Storms, and Subsidence

by

Laura Conners Reynolds

The highly developed and populated coast of southern California is at risk for inundation due to storms or tsunamis; coastal erosion; wildfires; earthquake-driven shaking, liquefaction, and subsidence; sea-level rise; and other hazards. Estuaries formed during periods of sea-level transgressions often record environmental changes that have affected the region over time. These records of past climate, sea level, inundation events, and other changes can provide a baseline with which to compare current changes. Past recurrence intervals of hazard events also provide an estimate for how often and at what magnitude we can expect events to recur in the future. Here we compile relative sea-level indicators from other studies on southern California estuaries to show that relative sea level in southern California has risen 0.8 ± 0.3 mm/yr over the last 4000 years, less than modern rates and predicted future rates of sea-level rise. Predicted acceleration of sea-level rise could exacerbate the effects of storm and tsunami inundation along the coast.

We use a variety of biological, sedimentological, and geochemical measurements on sediment cores from Carpinteria Marsh, Carpinteria, California, to document environmental changes that have occurred along the Santa Barbara Channel over the last 10,000 years. We

show evidence for at least 37 episodes of alluvial fan progradation due to large floods over the past 7 ka, clusters of which correspond to regional records of wet climate conditions. We also show evidence for one coseismic subsidence event at 1.0 ± 0.1 ka, which may correlate with records of other earthquakes in the region. Finally, the topmost sediments within the marsh record environmental changes within the historical period. Within these sediments, we use a multi-proxy approach to document the history of the marsh over the last 200 years including the appearance of European pollen species, makers of industrialization, and an overwash deposit related to the 1861-2 winter storm season in California.

TABLE OF CONTENTS

1. Introduction....1

2. Late Quaternary Relative Sea Level in Southern California and Monterey Bay....5

2.1 Introduction....5

2.2 Background....7

2.2.1 Overall geological setting of the California coast....7

2.2.2 Relative Sea Level....8

2.3 Methods....10

2.3.1 Compilation and indicator type....10

2.3.2 Data corrections....16

2.3.3 Error calculations....21

2.3.4 Late Holocene Rates of RSL Rise (RSLR)....22

2.4. Results....25

2.4.1 Southern California....25

2.4.2 Monterey Bay....27

2.4.3 Modern RSL Rates....29

2.5. Discussion....29

2.6. Conclusions....31

3. Coastal flooding and the 1861-2 California storm season....32

3.1 Introduction....32

3.2 Study Site....34

3.3 Methods....37

3.3.1 Core collection and physical sedimentology....37

3.3.2 Pollen Analysis 38
3.3.3 Spheroidal Carbonaceous Particle Analysis 38
3.3.4 Age-Depth Models 39
3.3.5 ^{210}Pb and ^{137}Cs Analysis 42
3.4 Results 46
3.4.1 Stratigraphy and Facies 46
3.4.2 Age-Depth Models 50
3.5 Discussion 54
3.5.1 Facies Interpretation 54
3.5.2 Timing of deposition of WSF 55
3.5.3 Implications 56
3.6 Conclusion 59
4. Holocene coseismic subsidence along a non-subducting active margin 61
4.1 Introduction 61
4.2 Study Area 63
4.3 Methods 66
4.3.1 Core collection and lithological analysis 66
4.3.2 ^{14}C Analysis 66
4.3.3 δ^{13}C Analysis 67
4.3.4 X-Ray Fluorescence (XRF) Analysis 69
4.3.5 Cerithidea Elevation Survey 69
4.4 Stratigraphic Evidence for Abrupt Environmental Change 71
4.5 Chronology of the CSS 75
4.6 Interpretation of the CSS 77

4.7 Magnitude of Subsidence....78
4.8 Hazard and Structural Implications....80
5. A Holocene hydroclimate archive from Carpinteria Marsh, California....82
5.1 Introduction....83
5.2 Study Site and Background....85
5.2.1 Seasonal and subseasonal climate....86
5.2.2 Interannual and decadal climate....87
5.2.3 Landscape response to precipitation....89
5.3 Methods....90
5.3.1 Grain size Analysis....90
5.3.3 Calculations and Data Processing....91
5.4 Results....91
5.4.1 Facies....91
5.4.2 Stratigraphy of CM46....93
5.4.3 Chronology....95
5.4.4 Stratigraphic Correlation....102
5.5 Discussion....104
5.5.1 Characteristic and occurrence of paleoflood deposits in Carpinteria Marsh....104
5.5.2 Comparisons to other records....105
5.6 Conclusions....116
6. Conclusions....118
Appendix A: List of Supplementary Files....139
Appendix B: Chapter 3 Supplementary Figures....140

Appendix C: Carpinteria Radiocarbon Dates 143

Appendix D: Carpinteria Core Info 147

Appendix E: Chapter 4 Discussion on Alternatives to subsidence.....149

LIST OF FIGURES

Figure 1. Location of estuaries, terraces, and previous studies referenced. 24

Figure 2. RSL data compilation for southern California. 26

Figure 3. RSL data compilation for Monterey Bay. 28

Figure 4. Location map 36

Figure 5. Core stratigraphy 49

Figure 6. Stratigraphy and chronology of CM20 51

Figure 7. Stratigraphy and chronology of CM15. 52

Figure 8. Stratigraphy and chronology of CM34. 53

Figure 9. Location of Carpinteria Marsh 65

Figure 10. Modern δ^{13}C measurements in Carpinteria Marsh. 68

Figure 11. Histogram of *C. californica* elevations in Carpinteria Marsh. 70

Figure 12. Transect A Core Stratigraphy 73

Figure 13. Evidence of RSL Change at the CSS 74

Figure 14. Chronology of the CSS. 76

Figure 15. Grain size, isotope, XRF data for CM46. 94

Figure 16 BChron age-depth model for the landward suite of cores. 97

Figure 17. BChron age-depth model for the seaward suite of cores. 98

Figure 18 BChron generated age models for CM16. 99

Figure 19 Stratigraphic correlation between cores 46, 49, and 51 103

Figure 20. Paleofloods of Carpinteria vs. SBB 108

Figure 21. Comparison of Carpinteria wet episodes to climate proxies 111

Figure 22. Location map for other sites referenced for pluvial proxies 112

Figure 23. Comparison of Carpinteria paleoflood events to pluvial episodes 114

CHAPTER 1

1. Introduction

The highly developed and densely populated coast of southern California is host to a wide variety of coastal hazards, including droughts, floods, earthquakes, wildfires, and tsunamis. In addition to these short-term, high-impact events, human infrastructure and coastal ecosystems are threatened by long-term sea-level rise and climate change. Many hazard events recur on longer than human timescales—therefore, historical documentation of such events is inadequate to develop reasonable risk analyses and determine recurrence intervals and magnitudes of events. In addition, understanding how coastal environments have responded to environmental changes in the past can help us prepare for and adapt to future changes. Sedimentary deposits—lakes, dunes, beaches, and estuaries—archive these past environmental changes within their geomorphology and stratigraphy.

Despite the importance of estuaries as archives of environmental history, filters of pollution, barriers to coastal inundation, and ecological and economic resources, little work has been conducted to understand the Holocene development of estuaries in southern California. In fact, it is estimated that less than 10% of the pre-colonial estuarine environments in southern California persist today (Lafferty, 2005). Many of the estuarine environments that remain are fragments of once larger systems that developed in flooded incised valleys, behind coastal barriers, or within tectonic basins (Simms et al., 2016). While estuaries developing in incised valleys and back-barrier environments have been extensively studied (Dalrymple et al., 1992), less is known about estuaries in tectonic basins.

One such tectonically active estuary in southern California is Carpinteria Salt Marsh (34°24’N, 119°31’30”W). Carpinteria Marsh is located along the Santa Barbara Channel, an

east-west trending portion of the southern California coastline. In Chapters 3 to 5, we use the sediments of this marsh to try to tease apart the history and effects of sea-level change, tectonic motion, climate change, and human influence on the Holocene marsh stratigraphy.

One of the dominant forces that has shaped the coastline of southern California over the Holocene has been post-glacial relative sea-level (RSL) change. Records of past RSL change documented from coastal sedimentary archives serve as important baselines with which we can compare future changes. On tectonically active coastlines, such as southern California, RSL histories are necessary datums used to calculate rates of vertical tectonic motion derived from paleo-shoreline indicators such as marine terraces, raised beaches, and buried marsh surfaces. Until recently, a tectonically-corrected late Quaternary RSL history for southern California had not been available. Chapter 2 (Reynolds and Simms, 2015) describes the first such RSL compilation for southern California and Monterey Bay, derived from previously published marsh and estuarine radiocarbon dates. We use this RSL history in subsequent work (i.e. Chapter 4) to quantify tectonic motion in Carpinteria Marsh.

Carpinteria Marsh exists within a Pleistocene-aged faulted syncline bounded to the south by the south-dipping Rincon Creek Fault (RCF) (Jackson and Yeats, 1982). Although movement along the RCF likely controls the geometry of the Carpinteria Basin itself, large east-west trending, north-dipping thrust faults such as the Red Mountain Fault (RMF) and Ventura-Pitas Point Fault (V-PPF) are thought to accommodate much of the shortening currently taking place in the transpressional Transverse Ranges (Jackson and Yeats, 1982). The subsurface structure in the Santa Barbara/Ventura region is much debated (Hubbard et al., 2014; Kamerling et al., 2003; Marshall et al., 2017; Rockwell et al., 2016), but recent studies have suggested that large magnitude ruptures, and potentially tsunamis (Ryan et al.,

2015), are possible. The proximity of Carpinteria Marsh to the RMF and V-PPF make it an ideal site to test for evidence of these large events.

Previous work suggests that the sedimentary evolution of Carpinteria Marsh is driven by ~1.2 m/kyr of tectonic subsidence along the Rincon Creek Fault (Simms et al., 2016). The 1.2 m/kyr subsidence does not differentiate between subsidence accommodated in discrete, large events, and that from ongoing compaction. Chapter 4 documents evidence for one discrete subsidence event at 1 ± 0.1 ka. The stratigraphy in the marsh dating to this time shows a sharp surface that superimposes subtidal sands over marsh surface deposits. The age of this subsidence event is contemporaneous with a large uplift event documented at Pitas Point (Rockwell et al., 2016), suggesting a possible relationship between movement along the RCF and the V-PPF.

However, we do not find any evidence for the older uplift events documented at Pitas Point, nor do we find any tsunami deposits which would be expected to be associated with sea floor ruptures. Instead, the deeper stratigraphy of Carpinteria Marsh is dominated by the interplay of marsh accretion and alluvial fan progradation events, with no stratigraphic evidence for subsidence events before the 1 ka event. Chapter 5 outlines the alluvial fan progradation history for Carpinteria Marsh—we interpret each progradation event as a past flood event or period of wetter than average climate, and compare the flood history from Carpinteria to that from other lake (Kirby et al., 2014; Kirby et al., 2012) and marine (Hendy et al., 2013) records.

In addition to sea-level change, climate, and tectonic effects, Carpinteria Marsh has more recently been influenced by anthropogenic effects. Since Europeans began farming in the Carpinteria Valley in the 1850s (Caldwell, 1979), the marsh has been diked, drained, infilled for development, and explored for petroleum resources (Ferren, 1985). The top two

meters of sediment within the marsh record this history of human influence with the appearance of exotic pollen markers and carbon spheroids introduced through fossil fuel combustion (Chapter 3).

Many natural hazard events were documented for the Santa Barbara Channel during the period of written records—the most prominent of which are the 1812 Santa Barbara tsunami (Toppozada et al., 2002) and the 1861-2 Great Storm of California (Engstrom, 1996). Chapter 3 documents evidence for one historical overwash event in Carpinteria Marsh which dates to the 1800s. High energy events (floods and tsunamis) can deposit sediments in the marsh that are similar in terms of grain size and sedimentary structures (Goff et al., 2012). Therefore we use a robust multi-proxy chronology to date the deposit to ~1862 AD, making this the first physical evidence for the effects of the 1861-2 storms on the coast of California, and supports the argument against any preservation of tsunami deposits in the marsh stratigraphy.

The following chapters further explore the late Quaternary development of the California coast including RSL changes and the record of climate, tectonic, and human influences that have affected the Santa Barbara region and are recorded in the sediments of Carpinteria Marsh.

CHAPTER 2

Reynolds, L.C., and Simms, A.R. (2015). Late Quaternary relative sea level in Southern California and Monterey Bay. *Quaternary Science Reviews* 126: 57-66.

2. Late Quaternary Relative Sea Level in Southern California and Monterey Bay

2.1 Introduction

Accelerated rates of sea-level rise in the 20th century have been found to be consistent with global temperature increases during the same period (Kemp et al., 2011). Recent models of future sea level predict additional acceleration over the next century due to thermal expansion, land-based ice loss, and other factors (Church et al., 2013). Records of past sea-level change from around the world provide a baseline for understanding, predicting, and preparing for these future changes.

Attempts have been made to determine a theoretical, ice-equivalent, eustatic sea-level history for the late Quaternary (Lambeck and Chappell, 2001; Lambeck et al., 2014; Peltier, 2002; Waelbroeck et al., 2002). However, modeled and observed sea-level change around the globe varies from eustatic estimates due to differences in glacial isostatic adjustment (GIA) processes, local tectonics, sediment loading, and steric factors (Clark et al., 1978; Lambeck and Chappell, 2001; Mitrovica et al., 2011; Pirazzoli, 1991). Quantifying this regional variability in relative sea-level (RSL) histories is necessary to determine how different coastlines have evolved in response to past sea-level rise, to reconstruct paleogeography during times of past human and faunal migrations, and to constrain the past distribution and melting history of ice sheets.

GIA models used to determine past ice-sheet distributions and the rheological properties of the Earth, important parameters for models that predict future sea-level change, require adequate global coverage of RSL data (Lambeck et al., 2014; Lambeck et al., 1998;

Mitrovica and Peltier, 1991; Spada et al., 2006). Existing large-scale numerical models of Holocene relative sea-level response (Clark et al., 2014; Clark et al., 1978; Mitrovica et al., 2011; Mitrovica et al., 2001; Muhs et al., 2012; Reeder-Myers et al., 2015) suggest in glacial times, southern California fell within a zone of uplift called the peripheral forebulge, which results from the migration of mantle material from beneath regions of ice load to the periphery of ice sheets. The subsequent postglacial collapse of this forebulge, along with ice sheet melting and gravitational components, would be expected to result in rising sea levels throughout the Holocene (Clark et al., 1978). However, very little RSL data for southern California are available to test these models or to determine differences in the isostatic response of the coastline with varying distances from the North American ice sheets along the northeastern Pacific Ocean.

Quaternary RSL data remain scarce for central and southern California in part due to complications that arise from the variable tectonic regimes of these regions. However, these very complications necessitate the establishment of a regional RSL curve: estimates of recent vertical tectonic rates in coastal areas based on elevations of paleo-shoreline features rely on the ability to remove the eustatic and isostatic contributions of relative sea-level change. The magnitudes of Holocene subsidence in individual sedimentary basins and uplift on recent terraces are only quantifiable when comparing site-specific RSL data to a regional curve. Rates of Holocene uplift in southern California have been calculated with the assumption that sea level has not deviated from modern levels in the late Holocene (Lajoie et al., 1982), which has not been tested for southern California. In fact, Gurrola et al., 2014 pointed out that without comparison to a regional sea level record, Holocene marine terraces exposed along the coasts of Santa Barbara and Ventura counties thought to represent recent uplift could also be, although unlikely, attributed to a sea-level high stand.

We begin to address these deficits in sea-level data by compiling existing radiocarbon ages derived from coastal, estuarine, and shelf material along central and southern California and correcting these data for long-term tectonic uplift, inconsistent sea-level datums, and variable marine radiocarbon reservoirs. This paper provides the first regional, tectonically corrected late Quaternary RSL history for southern California and a preliminary site-specific RSL history for Monterey Bay on which future GIA and tectonic studies can build.

2.2 Background

2.2.1 Overall geological setting of the California coast

The southern and central California coast is a tectonically active margin, most generally characterized by right-lateral strike-slip motion along the San Andreas Fault system, with local areas of compression and extension (Drummond, 1981; Simkin et al., 2006; Wallace). The coastline consists of crustal blocks uplifting or subsiding at different rates. Sections of the coastline undergoing uplift are often characterized by elevated marine terraces of various ages (Muhs et al., 2014). Estuaries are formed within incised valleys that cut these terraces, in tectonic synclines, or behind coastal barriers. Because the continental shelf of much of central and southern California is as narrow as 10-20 km wide, typically less than 200m deep, and characterized by high wave energy (Draut et al., 2009), most paleo-estuarine deposits formed on the shelf during times of lower sea level, but outside of incised valleys or structural basins, were likely modified or eroded away during post-glacial transgression (Le Dantec et al., 2010; Sommerfield and Lee, 2004).

Existing estuarine deposits beneath modern estuaries (e.g. San Francisco Bay, (Atwater et al., 1977) or preserved in now submerged submarine canyons along the

continental shelf (La Jolla Canyon, Sheppard and Dill, 1966) in central and southern California record a mixture of tectonic, climatic, and anthropogenic changes in the late Quaternary. The climate of much of coastal southern California is Mediterranean, with cool, wet winters and warm, dry summers (Bakker and Slack, 1985). This seasonality results in small fluvial systems exhibiting flashy, storm dominated flow (Warrick and Mertes, 2009; Warrick and Milliman, 2003). Storm supplied sediments comprise a large part of the sediment budget along the coast (Drake et al., 1972; Patsch and Griggs, 2006), and influence the geomorphology of estuarine systems. Estuaries in California have also been highly disturbed by human activity and today are only fractions of their former size (Lafferty, 2005; Lohmar et al., 1980; Nichols et al., 1986; Zedler, 1996).

2.2.2 Relative Sea Level

Global GIA models predict that the California coast falls within an intermediate-field zone of forebulge collapse—equivalent to Clark's (1978) Zone II, which predicts consistently rising sea level from ice sheet decay through the Holocene. This prediction is supported by models of deglacial RSL for the Channel Islands, California (Santa Rosa Island, Clark et al., 2014; San Nicolas Island, Muhs et al., 2012; Northern Channel Islands, Reeder-Meyers et al., 2015) that suggest sea level rose dramatically from ~100 m to ~15 m below present mean sea level (PMSL) until ~8 ka, at which point the rise decelerated to present.

While Holocene RSL data exist for the San Francisco Bay region (Atwater et al., 1977; Engelhart et al., 2015; Meyer, 2014), and farther north along the Pacific margin (Clague et al., 1982; Engelhart et al., 2015; Hamilton and Shennan, 2005; Shugar et al., 2014), only one data-based RSL curve, derived from dating submerged basal transgressive

deposits on the Santa Monica shelf (Inman, 1983; Masters, 1988; Nardin et al., 1981), exists for southern California. The Santa Monica curve established a rough baseline for the region, but is uncorrected for tectonics and is based on seismic stratigraphy and only six radiocarbon dates, five of which are from shell hash material within transgressive lag deposits on the continental shelf. While many types of coastal transgressive deposits, such as incised valley and back-barrier estuarine deposits, are useful in sea-level reconstructions (Sloss et al., 2005; Sloss et al., 2007), basal transgressive lag deposits include material reworked by wave action during the early stages of transgression along a shelf. Because the original depths of the dated shell material, as well as the degree of reworking post-deposition is unknown, reconstructions based on transgressive lag deposits contain at least 10m of uncertainty in RSL reconstructions (Nardin et al., 1981). The Nardin et al. (1981) curve also suggests the most rapid sea-level rise in the Holocene occurred between 3 and 5 ka, which would require either a GIA response uncharacteristic of an intermediate-field location (Clark et al., 2014) or a eustatic ice-volume equivalent sea-level history inconsistent with current compilations (Lambeck et al., 2014).

Compilations of RSL data from other intermediate-field locations in the United States such as the Atlantic (Engelhart et al., 2009; Engelhart et al., 2011) and Gulf coasts (Simms et al., 2007), have been used to test GIA models for these regions and have demonstrated systematic differences in RSL rates of rise related to distance from ice-loading centers. These compilations and models also show no evidence for higher-than-modern RSL during the Holocene in regions located at similar distances from the major ice sheets as southern California. A recent compilation of sea-level data from San Francisco to Vancouver, derived from dated salt marsh deposits, isolation basins, marine and terrestrial materials, and archeological sites (Engelhart et al., 2015), indicates the maximum late

Holocene rates of RSL rise occur in northern and central California and decrease to the north as forebulge collapse becomes less influential closer to the margin of the Cordilleran ice sheet. Because of the scarcity of Holocene RSL data in southern California, comparable observational tests of model-derived predictions for glacio-isostatic response and sea-level rise have not been available for the west coast of North America south of San Francisco, California.

2.3 Methods

2.3.1 Compilation and indicator type

We used two different types of sea-level indicators in this study: those with a quantitative relationship to past mean sea level, called sea-level index (SLI) points, and others with a limiting relationship to past sea levels (limiting data). SLI points must have a known location, age, and indicative meaning, i.e. an established vertical relationship to a reference water level (Shennan, 1986; van de Plassche, 1986). Examples of SLI points used in other RSL studies include microbial mats (Livsey and Simms, 2013), estuarine mollusk species (Shennan, 1986; van de Plassche, 1986), marsh foraminifera and diatoms (e.g. (Edwards and Horton, 2006; Hawkes et al., 2010; Horton et al., 1999; Kemp et al., 2011), saltwater marsh material (Tornqvist et al., 2004), corals (Bard et al., 1996; Chappell and Polach, 1991; Fairbanks, 1989), and mangroves (Bartlett and Barghoorn, 1973; Ellison, 1989; Zhen et al., 2012). Limiting data indicate that sea level must have been at or above (marine-limiting) or at or below (terrestrial-limiting) the feature dated. Examples of terrestrial-limiting data used in other RSL studies include beach ridges (Masters, 2006) and isolation basins (Bentley et al., 2005; Simms et al., 2009), while many mollusk species are marine-limiting (Petersen, 1986; Richards, 1985).

We compiled 254 radiocarbon-ages collected by previous authors from existing published and unpublished sources (Supplementary Data). These radiocarbon-ages were originally taken to aid research on the paleoecological, environmental, and geological histories of coastal environments in central and southern California (Anderson et al., 2010; Cole and Liu, 1994; Cole and Wahl, 2000; García-García et al., 2013; Hornberger, 1991; Inman, 1983; Mudie and Byrne, 1980a; Palacios-Fest et al., 2006; Scott et al., 2011; Watson et al., 2011), archeological investigations (Davis, 1996); seismic hazard and geotechnical studies (Grant et al., 1997; McNeilan et al., 1996), wetland carbon sequestration estimates (Brevik and Homburg, 2004), Holocene climate change (Davis, 1992), continental shelf sedimentation (Sommerfield and Lee, 2003, 2004; Sommerfield et al., 2009), and Quaternary sea level (Inman, 1983; McMillan et al., 2003; Nardin et al., 1981).

Of the total compiled ages, we excluded ages from samples that had no clear relationship to sea level, such as bones; specific indications of reworking, such as transgressive lag shell hash deposits, drift wood, and "burrowing clams" (McNeilan et al., 1996); were out of stratigraphic succession with other ages from the same site; or were otherwise described and erroneous or questionable by the original author. We also excluded four ages of organic material from marsh sediments in Ballona wetlands, Los Angeles County (Supplementary Data), which fall above terrestrially limiting data points of a similar age (Brevik and Homburg, 2004) Brevik and Homburg, personal communication). These outlying ages are derived from peat, wood, and organic sediments which possibly include older, reworked organic material. Our final compilations include 132 ages from southern California and 48 ages from Monterey Bay.

We determined whether each age would be used as a limiting point or as a SLI point according to the description of the sample material and sedimentary context. We relied on

the interpretation of the original authors who used evidence such as microfossils, shell content, plant macrofossils, sedimentary characteristics, and/or isotopic composition to determine the depositional environment of the sample or sedimentary unit (specific evidence used is listed in Supplementary Data). Terrestrial-limiting data include ages from freshwater peat, wood, organic material, or shells of terrestrial species found within sediments indicating freshwater deposition. Marine-limiting data include mollusk species with known large depth ranges described as within marine, bay, nearshore, or shallow shelf sediments. Terrestrial materials such as charcoal, wood, and plant material found within marine sediments were also used in a marine-limiting context as this material, if reworked, would still represent RSL somewhere above the elevation at which they were deposited.

Shell materials were characterized as terrestrial-limiting (3 ages), marine-limiting (55 ages), or marsh/estuarine (12 ages, plus 7 C. Californica ages) depending on the species (when provided) and sedimentary context. Shell types used in this compilation include: *Chione* sp., *Ostrea lurida, Laevicardium substriatum, Tagelus subteres, Mascoma nasuta, Tivela stultorum, Pecten circulare aequisulcatum, Plagioctenium circulare aequisulcatum,* and *stagnicola* sp., although many samples were undifferentiated. Many intertidal mollusk species in southern California inhabit a depth range relative to MSL and can be found both in estuarine environments as well as marine environments (Coan et al., 2000; Nardin et al., 1981). Therefore we primarily used the sedimentary context, not species type, to determine each shell-derived data point's designation.

SLI points include estuarine shells, bulk organic material, charcoal, plant parts, and peat described as representative of or occurring within salt-water marsh, lagoon, or estuarine sediments. Some samples, especially charcoal, shell fragments, and unspeciated plant material, likely experienced an unknown degree of reworking before final deposition. Unless

they were specifically described as questionable or reworked, or were out of stratigraphic succession with other ages from the same core, they were interpreted to be representative of the age of sediment deposition.

SLI points were assigned indicative ranges based on the material dated and interpreted depositional environment (Table 1.). One of the most common estuarine mollusk species in southern California, *Cerithidea californica,* was used as a sea-level index point due to its established indicative range of 1.2 to 2.1 m above Mean Low Water (MLLW) (Sousa, 1983). We followed other authors (Engelhart et al., 2015; Tornqvist et al., 2004) and assigned an indicative range of Mean Sea Level (MSL) to Highest Astronomical Tide (HAT) to ages from material within undifferentiated salt marsh deposits. Surveys of California marsh vegetation and microfossil elevations (Ferren, 1985; Scott et al., 2011) support this interpretation.

Because non-marsh estuarine sediments may be deposited below MSL, we assigned samples within sediments described as indicative of estuarine or lagoon environments to an indicative range of Lowest Astronomical Tide (LAT) to HAT for organic materials and LAT-MSL for estuarine shells other than *C. Californica*. The larger estuarine systems in southern California (e.g. Batiquitos, Buena Vista, and San Dieguito lagoons) contain areas of shallow (average <2 m water depth) subtidal environments (Beller, 2014; Elwany, 2011). Historical and pre-historical depths of these systems are uncertain. A recent examination of compiled paleoecological and historical data suggests the lagoons within San Diego County were, in prehistoric time, dominated by intertidal salt flats instead of the open water environments that exist today (Beller, 2014). This interpretation suggests estuarine sediments accumulated above LAT. However, to account for the uncertainty that remains in the depth of deposition of estuarine/lagoon sediments, we use LAT as a conservative lower

bound. The larger bays of southern California, which include Newport Bay, San Diego Bay, and Mission Bay, reach subtidal depths well below LAT (Scott et al., 2011). Therefore, we differentiate samples described as within “bay” sediments from those described as within “lagoon” or “estuarine” sediments and classify the former as marine-limiting points.

Table 1. Sample type descriptions and indicative meaning.

Designation	Description	Relationship to sea level
IC	*Cerithidea californica* shells in estuarine or marsh sediment.	1.2–2.1 m above MLLW
IM	Any sample in salt marsh, mudflat, salt pan sediments; salt water peats	MSL-HAT
IE	Samples in lagoon, estuarine sediments.	LAT-HAT (organics); LAT-MSL (shells)
ML	Shells in beach, bay, littoral inner shelf, nearshore sediments	marine-limiting: at or below MSL
TL	organics or freshwater shells in fluvial or freshwater sediments; freshwater peat	terrestrial-limiting: at or above MSL

2.3.2 Data corrections

2.3.2.1 Vertical corrections

We used the nearest open-ocean tide gauge data available from NOAA (http://tidesandcurrents.noaa.gov) to convert all sample elevations to relative to the most recent estimate of MSL for each estuary (Table 3.). For data from each estuary, we used uplift rates derived from shoreline angle elevations of the most closely related Marine Isotope Stage 5e (MIS5e) terrace to remove the effect of long-term, regional uplift on past RSL estimates (Table 2.). We used GIA-corrected uplift rates calculated Simms et al. (2015) which assumes a 119 ka age for all MIS5e terraces (modeled time of highest sea level) and a +12 m ± 3 m 5e sea level relative to PMSL, similar to other GIA model results indicating MIS5e sea levels of ~ +11 to +13 m relative to PMSL (Creveling et al., 2015). The time represented by this average uplift is much longer than that represented by the data in this compilation, therefore any deviations in Holocene uplift rates from long term trends are not reflected in this correction.

We used the San Joaquin Hills terrace correction for all Los Angeles region estuaries except data points from cores located on the up-thrown side of the Palos Verdes fault in Los Angeles Outer Harbor which are on the same tectonic block as the rapidly uplifted Palos Verdes terrace (McNeilan et al., 1996). Because of the complexity of tectonism in the Los Angeles Basin (Plesch et al., 2007), marshes within Los Angeles are more likely than those in the San Diego region to be influenced by localized tectonic movement in addition to long-term, regional tectonic uplift represented by the MIS5e terraces. Therefore the tectonic uplift rate derived from the San Joaquin Hills is unlikely representative for all of the marshes in the region. However, it is the best estimate available, and indicates less than 2.5 m of uplift has occurred in the last 14 ka, indicating small differences in uplift rate would not significantly

alter elevations. We used the Davenport MIS 5a terrace elevation (Bradley and Griggs, 1976) and an average age of 77.5 ka (Muhs et al., 2006) to correct for tectonic uplift in the Monterey region because no well dated MIS5e terraces or shorelines have been identified on the same tectonic block as Elkhorn Slough.

Table 2. MIS5e terraces used in uplift rate calculations.

Region applied	Terrace location	Average shoreline angle elevation (m)	Error (m)	Paleo sea level (m)	Error (m)	Rate of uplift (mm a^{-1})	Error (mm a^{-1})	Reference(s)
Los Angeles Region	San Joaquin Hills	28.5	3.5	12	3	0.18	0.04	Grant et al., 1999; Simms et al., 2015
San Diego Region	Oceanside, Point Loma	22.5	0.5	12	3	0.08	0.04	Ku and Kern, 1974; Kern and Rockwell, 1992; Muhs et al., 2002; Simms et al., 2015
Channel Islands Region	San Miguel Island	22.5	1.5	12	3	0.08	0.04	Muhs et al., 2014; Simms et al., 2015
Upthrown side of Palos Verdes Bay	Palos Verdes	89	7	12	3	0.65	0.06	Muhs et al., 2006; written communication, Daniel Muhs
Monterey Bay	Santa Cruz Point (Davenport 5a)[a]	13.5	1.5	−11.5	0.5	0.33	0.02	Bradley and Griggs, 1976; Muhs et al., 2006

a 5a terrace instead of 5e terrace: age 77.5 ka ± 2.5 ka (Muhs et al., 2006).

2.3.2.2. Age Corrections

For consistency, we corrected and recalibrated the original ^{14}C ages. We used previously determined ranges of $\delta^{13}C$ values to correct previously uncorrected ages (Gupta and Polach, 1985). Because coastal and estuarine ΔR values have been shown to be highly variable along the California coast (Holmquist et al., 2015; Ingram and Southon, 1996), we used a local ΔR for each estuary where available (from Queen's University Marine Reservoir Correction Database, http://radiocarbon.pa.qub.ac.uk/marine/), and average regional values when a specific value was not available (Table 3). Estuarine organic matter ages were calibrated using INTCAL13 and mollusk shells were calibrated using MARINE13 (Reimer et al., 2013). Ages are reported in calendar years BP.

One significant uncertainty in radiocarbon ages derived from marine/estuarine carbonates is the degree to which ΔR values vary over time. Here we applied modern ΔR estimates to all ages, but paired organic-carbonate material ages (Kennett et al., 1997; McNeilan et al., 1996; Sommerfield and Lee, 2003) indicate modern values may not apply to older samples because of past differences in ocean circulation and upwelling strength. This implies an additional, but so far unquantified, uncertainty to carbonate age ranges.

Table 3. Site information.

Site	NOAA station used	Recent RSLR (mm a^{-1})[a]	HAT (m PMSL)	LAT (m PPMSL)	Tidal range (m MHHW-MLLW)	1900 A.D. MSL (m PMSL)	*Cerithidea* range (m PMSL)	Delta R (^{14}C yrs)	Delta R uncertainty (^{14}C yrs)	Source Delta R
San Diego Region										
Tijuana Slough	San Diego Bay	2.08 ± 0.18 (2.16 ± 0.18)	1.46	−1.54	1.75	−0.20	–	–	–	
Mission Bay Wetlands	San Diego Bay	2.08 ± 0.18 (2.16 ± 0.18)	1.46	−1.54	1.75	−0.20	–	195	30	Ingram and Southon, 1996
La Jolla Submarine Canyon	La Jolla	2.11 ± 0.26 (2.19 ± 0.26)	1.35	−1.41	1.62	−0.21	–	236	80	Bien et al., 1960
Los Pensaquitos Lagoon	La Jolla	2.11 ± 0.26 (2.19 ± 0.26)	1.35	−1.41	1.62	−0.21	0.37–1.27	220	40	Ingram and Southon, 1996
Batiquitos Lagoon	La Jolla	2.11 ± 0.26 (2.19 ± 0.26)	1.35	−1.41	1.62	−0.21	–	220	40	Ingram and Southon, 1996
Los Angeles Region										
San Joaquin Marsh/Newport Bay Wetlands	Newport Beach	2.22 ± 1.04 (2.40 ± 1.04)	1.34	−1.43	1.65	−0.20	0.36–1.26	309	119	Ingram and Southon, 1996
Hungtinton Beach	Newport Beach	2.22 ± 1.04 (2.40 ± 1.04)	1.34	−1.43	1.65	−0.20	–	309	119	Ingram and Southon, 1996
Ballona Wetlands	Santa Monica	1.43 ± 0.34 (1.61 ± 0.34)	1.37	−1.45	1.65	−0.13	0.35–1.25	244	123	Berger, 1966; Ingram and Southon, 1996
Santa Monica Shelf	Santa Monica	1.43 ± 0.34 (1.61 ± 0.34)	1.37	−1.45	1.65	−0.13	–	220	40	Ingram and Southon, 1996
Los Angeles Outer Harbor	Cabrillo Beach	N/A	1.41	−1.84	1.67	–	–	270	55	Ingram and Southon, 1996
Santa Barbara Channel Region										
Santa Rosa Island (Abalone Rocks Estuary)	Gaviota	N/A	1.34	−1.46	1.61	−0.06	–	–		
Central California										
Monterey Bay	Monterey	1.16 ± 0.95 (1.49 ± 0.95)	1.28	−1.46	1.63	−0.12	–	416	50	Ingram and Southon, 1996

a Mean linear rates cited are taken from http://tidesandcurrents.noaa.gov/sltrends/sltrends.html, from tide gauge RSL trends over 86–100 years. RSLR rates corrected for tectonic uplift listed in Table 2 are shown in parentheses.

2.3.3 Error calculations

Age error includes errors in the $\delta^{13}C$ correction, where used; uncertainty in the local ^{14}C reservoir value; and analytical uncertainty in the radiocarbon age itself. The calibration programs used automatically combine these errors (Reimer et al., 2013). Error in elevation measurements of SLI points were calculated each vertical direction using Equation 1,

$$E_{total}=(e_{measured}+e_{indicative\ range}+e_{elevation}+e_{tectonic})^{1/2} \quad (1)$$

where E_{total}= total error in elevation measurement in one direction, $e_{measured}$= uncertainty in the measured depth of sample, $e_{indicative}$=indicative range of sample, $e_{elevation}$=1/2 tidal range for samples without core-top elevation data, and $e_{tectonic}$=error calculated from tectonic correction (following Engelhart et al., 2015; Shennan and Horton, 2002). In the case of limiting data, we calculated depth errors using Equation 1, but without indicative range error. For terrestrial-limiting data, sea level is assumed to be at or below the upper bound of each point's depth-error range. For marine-limiting data, sea level is assumed to be at or above the lower bound of each point's depth-error range.

For 60 ages, core-top elevations were not provided (see Supplementary Data). Because these cores were described as taken within a present day estuarine environment, we assumed that the top of the core, or ground surface, occurred within the tidal range of the present-day marsh and added the tidal range to the uncertainty associated with the depth of SLI points. Because tidal ranges change over time (Hill et al., 2011), we used the open ocean tidal range instead of the dampened ranges found within the marshes of southern California (Sadro et al., 2007). We did not add an error term for variation in coring methods, as details of methodologies were not always specified.

We also did not correct or include an error term for compaction of sediments, which would give lower apparent values to sea-level indicators over time. While many methods of

decompacting sediment quantitatively do exist (Brain et al., 2014; Brain et al., 2011; Brain et al., 2012; Paul and Barras, 1998), necessary properties such as void space, organic matter content, etc. were not measured in the sources used for this compilation. Compaction would likely represent less than 10% of the total Holocene sediment package thickness (Paul and Barras, 1998) in the dominantly mineral-rich sediments of southern California (Davis, 1992; Mudie and Byrne, 1980a; Scott et al., 2011). Thus, 10% of the Holocene thickness can be considered a maximum potential error due to compaction, but is likely less in many areas. Future work should focus on quantifying the effects of compaction locally using empirically derived tests of modern sediment as has been done in other regions (Brain et al., 2014; Brain et al., 2011; Brain et al., 2012; Horton et al., 2013).

2.3.4 Late Holocene Rates of RSL Rise (RSLR)

We used the mean RSL relative to PMSL for SLI points with median calibrated ages less than 4000 years BP to calculate a linear rate of late Holocene RSLR for Southern California and Monterey Bay. We removed any contribution of potentially anthropogenic-influenced RSLR since 1900 A.D. by converting all ages to years before 1900 A.D. and adjusting all RSL estimates to meters below MSL at 1900 A.D. (Engelhart et al., 2009; Shennan and Horton, 2002). 1900 A.D. MSL values relative to PMSL were sourced from mean values extrapolated from NOAA tide gauge records for California (http://tidesandcurrents.noaa.gov, see Table 3.).

We used Monte Carlo methods to simulate 1000 iterations of our Late Holocene RSL data based on uncertainty in age and depth for each SLI point (uncertainties were assumed to be Gaussian). We then used an orthogonal linear regression forced through the origin to

calculate rates of late Holocene RSL for each simulation. Rates presented represent the mean regression slope from the Monte Carlo simulations with 2 σ uncertainties.

We compared our RSL rates to average 20th century rates calculated from tide gauge data at San Diego, La Jolla, Newport, Santa Monica, and Monterey NOAA stations (http://tidesandcurrents.noaa.gov/sltrends/sltrends.html). For a consistent comparison, we corrected the tide-gauge-derived RSL rates for the same MIS5e derived uplift rates described above to estimate the average 20th century RSLR at each site (Table 3.).

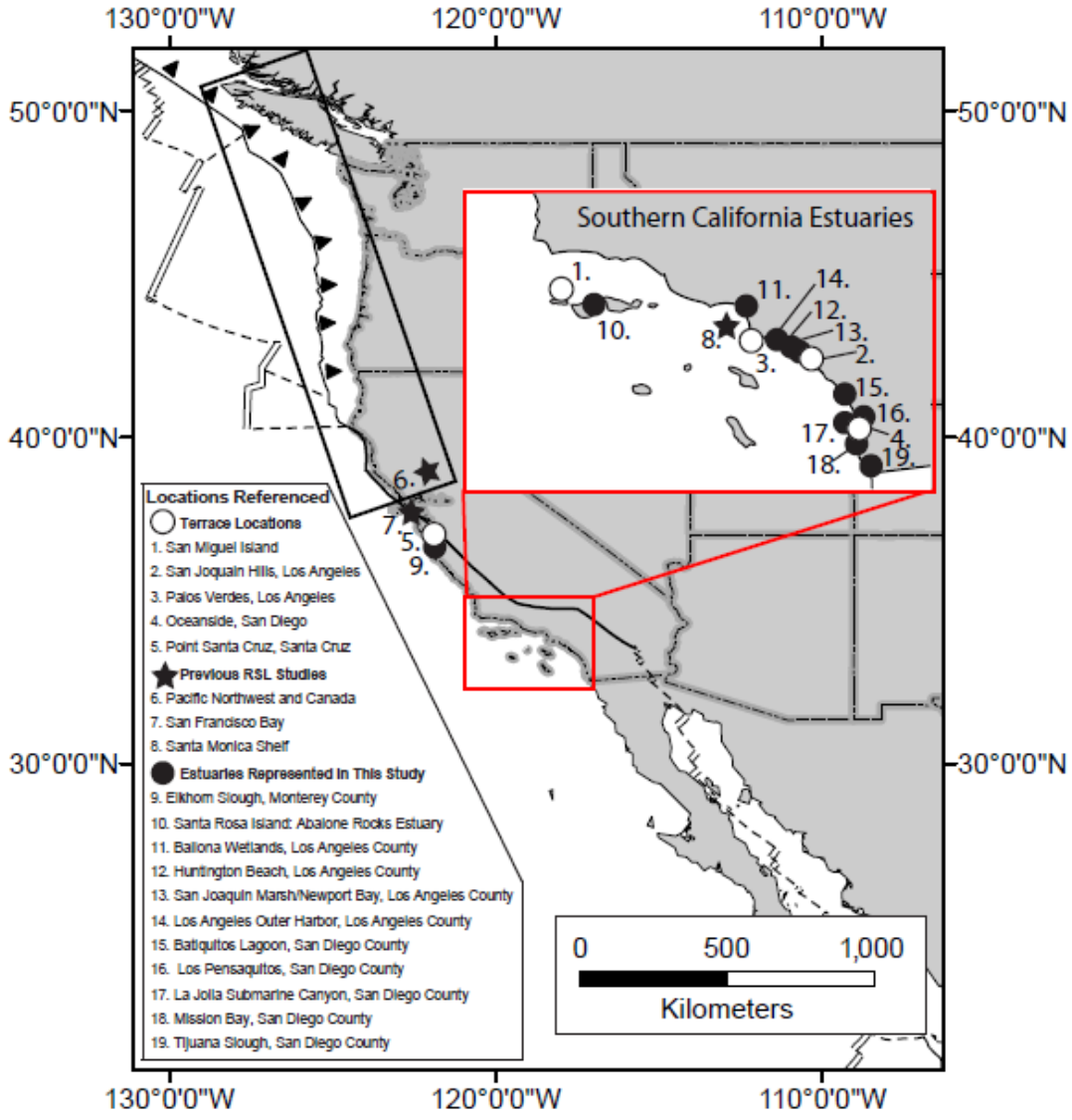


Figure 1. Location of estuaries, terraces, and previous studies referenced.

2.4. Results

2.4.1 Southern California

The RSL curve for southern California has been reconstructed from data listed in Supplementary Data, compiled from 11 estuaries and nearshore environments across three broad regions: the Santa Barbara Channel (5 points), the Los Angeles region (107 points), and the San Diego region (20 points) (see Figure 2.). No systematic differences between these three regions are observed (see Figure 2a, b, c.). The compilation shows continuously rising sea level since 12.5 ka, consistent with GIA model predictions (Clark et al., 2014; Muhs et al., 2012; Reeder-Myers et al., 2015). However, magnitudes and rates of RSL rise differ from model predictions. Model RSL values consistently fall below the range of paleo-RSL indicated by the SLI points presented in this compilation by as much as ~10m (at ~7 ka). The late Holocene rates of RSLR calculated from compilation data is 0.8± 0.3 mm a^{-1}, while the rate of RSL from Muhs et al., 2012 for this same period is ~1.3 mm a^{-1}. The upper uncertainty ranges of two points fall above MSL, therefore, no consistent and reliable indications of higher than modern sea level occur at any point during the Holocene, consistent with GIA models (Clark et al., 2014; Muhs et al., 2012; Reeder-Myers et al., 2015).

The 59 marine-limiting ages generally fall below the 41 SLI points, as expected. *C. californica* ages fall towards the middle of the data compilation, demonstrating its potential utility as a sea-level indicator in future studies in southern California. The 32 terrestrial limiting points also tend to fall towards the top of the data compilation.

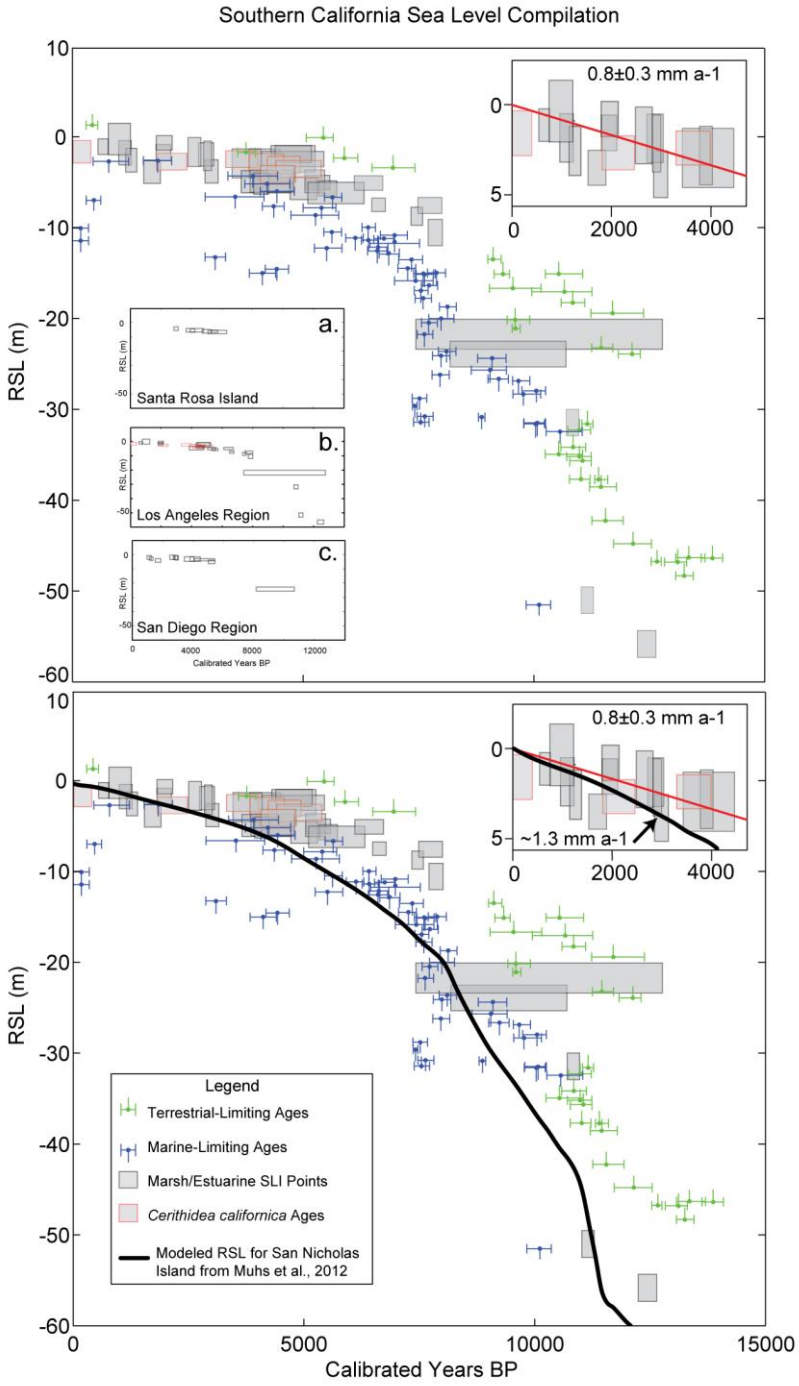


Figure 2. RSL data compilation for southern California. Inset shows Late Holocene (<4 ka) RSLR. Bottom panel shows data compilation overlain by RSL model for San Nicolas Island from Muhs et al., 2012.

2.4.2 Monterey Bay

The RSL curve for Monterey Bay is derived from 48 radiocarbon ages from Elkhorn Slough (34 points), Moro Cojo Slough (11 points), and Tembladero Slough (3 points). Thirty-eight of these points are SLI points, 7 are marine-limiting, and 3 are terrestrial-limiting. This compilation shows a similar pattern of rapid sea-level rise prior to 6 ka followed by a deceleration to present rates, although no SLI points older than 6 ka exist at present. The rate of late Holocene RSL rise over the last 4 ka is 1.3 ± 0.19 mm a^{-1}.

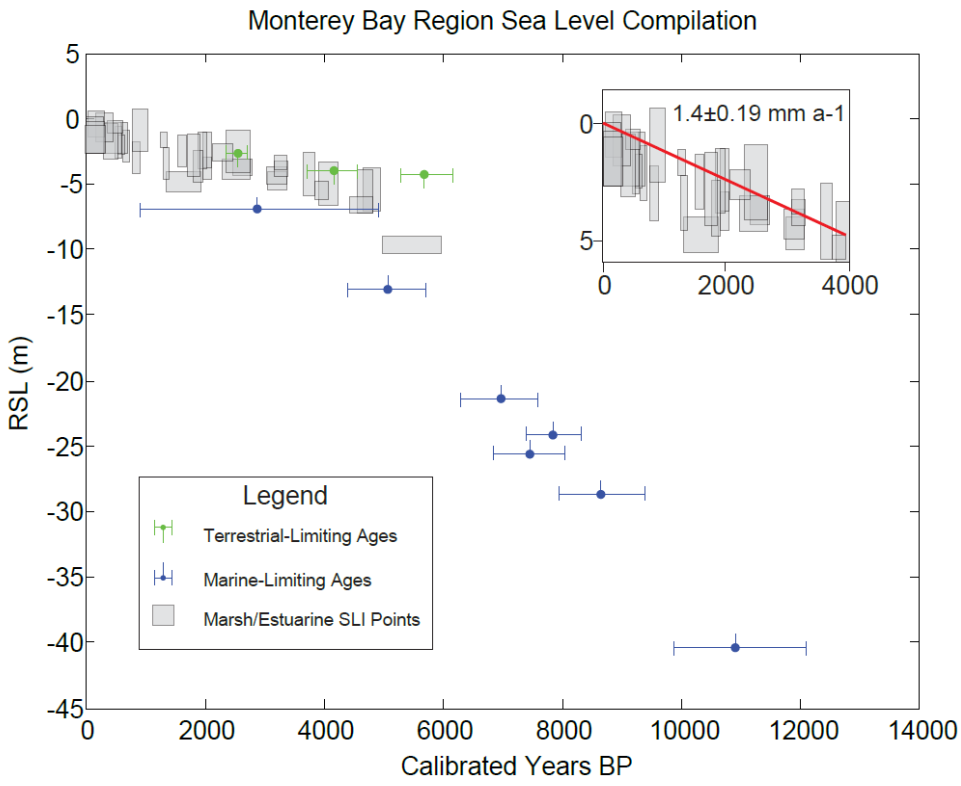


Figure 3. RSL data compilation for Monterey Bay, greater Elkhorn Slough region. Inset shows late Holocene (<4 ka) RSLR.

2.4.3 Modern RSL Rates

RSL rates from southern California and Monterey Bay corrected for uplift range from a high of 2.40 ± 1.04 mm a^{-1} at San Joaquin Marsh and Huntington Beach to a low of 1.49 ± 0.95 mm a^{-1} in Monterey Bay (Table 3). These rates are comparable to estimates of global average rates of sea level rise over the 20th century (1.7±0.3 mm a^{-1}, Church and White, 2006; 2011). However, accelerated rates of RSL since the 1990s are lower along the Pacific Coast of North American than global averages due to dynamic suppression of RSL rise caused by recent atmospheric wind pattern changes (Bromirski et al., 2011), indicating an even larger discrepancy between late Holocene RSLR calculated here and future RSLR for the Pacific coast.

2.5. Discussion

Our RSL compilation for southern California, corrected for regional, long-term tectonic uplift, dominantly reflects the glacio-isostatic and eustatic components of sea level. Site-specific effects on RSL such as differential compaction, tectonic motion along small localized faults, and anthropogenic effects have not been removed and likely contribute to the variability observed. The compilation supports models of late Quaternary RSL for southern California, which predict continuously rising sea level along the coast (Clark et al., 2014; Muhs et al., 2012; Reeder-Myers et al., 2015). Offset during the mid and late Holocene suggests models could be refined for mainland southern California with additional RSL data.

No Holocene high stand in RSL is evident for Monterey Bay and southern California, generally supporting predicted patterns of forebulge collapse. Engelhart et al. (2015) demonstrated that late Holocene RSLR rates increase north to south in the Pacific Northwest

from 0.1 and 0.15 mm a^{-1} km^{-1} in Washington, to a maximum rate of 1.5± 0.2 mm a^{-1} in Northern California and San Francisco Bay. Our results indicate late Holocene RSL rates decrease south from San Francisco Bay from 1.3 ± 0.19 mm a^{-1} in Monterey Bay to 0.8± 0.3 mm a^{-1} in southern California, reflecting a decreased signature of the collapsing forebulge farther to the south.

Localized vertical tectonic motion in southern California, similar to long-term uplift represented by MIS 5e terraces, should be evident when site-specific sea-level and geomorphic data is compared to the regional compilation. In southern California, no individual marsh used in this study shows a clear systematic difference from the other sites, which would otherwise indicate localized vertical motion from tectonic, differential compaction, or anthropogenic sources. However, the compilation indicates Holocene terraces along the coasts of Ventura, Santa Barbara, and Los Angeles counties (Grant et al., 2002; Gurrola et al., 2014; Lajoie et al., 1979; Lajoie et al., 1982) represent recent uplift, because no Holocene RSL stands higher than present are apparent, and assumptions of zero RSL rise in the late Holocene are incorrect.

Future work to quantify isostatic differences in RSL along the California coast, rates of anthropogenic subsidence from groundwater and oil extraction, and background rates of recent sea-level rise should focus on site-specific RSL studies which minimize vertical error by using material with a narrower indicative range and by constraining the effects of sediment-compaction.

2.6. Conclusions

In this paper we have presented two compilations of RSL data for regions in California: one for southern California, and another for Monterey Bay on the central California coast. Although variable tectonic regimes, compaction, and other factors may contribute to much of the scatter observed, a trend of decelerating sea-level rise over the Holocene is pronounced in both compilations, with rates of late Holocene rise in southern California and Monterey Bay of 0.8± 0.3 mm a^{-1}, and 1.3 ± 0.19 mm a^{-1}, respectively, both lower than uplift-corrected, average 20th century rates of rise (~2 mm a^{-1} for southern California and ~1.5 mm a^{-1} for Monterey Bay). The southern California compilation represents, to our knowledge, the first of its kind for this area and provides confirmation that the region is within a collapsing peripheral forebulge during the early and mid-Holocene. Holocene marine terraces exposed along the coast therefore indicate uplift, not Holocene highstands in sea level. If the age of these terraces, or the age of marsh surfaces in a subsiding basin, can be determined, the RSL data presented here will aid in determining rates of vertical motion. These compilations will also provide a basis for further sea-level studies along the Pacific coast of North, Central, and South America—regions which are in need of RSL studies to fill data gaps and better constrain ice sheet and glacio-isostatic models.

CHAPTER 3

Reynolds, L.C., Simms, A.R., Ejarque, A., King, B., Anderson, R.S., Carlin, J., Bentz, R.M., Rockwell, T.K., Peters, R (2018). Coastal Flooding and the 1861-2 California Storm Season. *Marine Geology*, in press.

3. Coastal flooding and the 1861-2 California storm season

A series of large storms attributed to Atmospheric River conditions struck the California coast in the winter of 1861-2. Although historical accounts document inland flooding, little is known about how the 1861-2 storms impacted the now heavily-developed California coast. Here we show that the 1861-2 storms emplaced a deposit of beach sand up to 50 cm thick over 450 m inland within a southern California salt marsh. This deposit is unprecedented in the post-European sediments of the marsh and more extensive than that derived from any other historical event. It is comparable in scale to hurricane and tsunami washover fans in back-barrier environments along other coastlines. The presence of overwash deposits in Carpinteria suggests that the 1861-2 storm season was erosive enough to remove coastal barriers, allowing for inundation of parts of the coastline currently developed. Efforts to prepare for a recurrence of an 1861-2 -like storm season should address potential coastal impacts; likewise, interpretations of past washover deposits should consider these unusually prolonged stormy periods in addition to hurricane and tsunami inundation.

3.1 Introduction

Storm-generated coastal erosion and inundation, river floods, and landslides have had costly consequences for the highly developed and populated world coastlines. Along the Pacific coast of North America, many of the most destructive storm seasons in the historical period have occurred during recent El Niño winters (e.g., 1982-3, 1997-8) (Barnard et al.,

2015). However, the longest-lasting and largest-magnitude (in terms of precipitation) storm season in the written record occurred during the winter of 1861-2 (Engstrom et al., 1996), when a series of mid-latitude storms resulted in two months of nearly continuous rain. Historical observations from the winter of 1861-2 describe the transformation of the Sacramento Valley into a large inland lake and flooding in many other metropolitan areas including San Francisco and Los Angeles (Engstrom, 1996; Guinn, 1890). One record from San Diego also describes a storm surge within San Diego Bay (Engstrom, 1996; Kuhn and Shepard, 1984), indicating the possibility of coastal flooding in addition to river flooding.

The storms of 1861-2 have been attributed to Atmospheric Rivers (ARs) (Dettinger and Ingram, 2013), concentrated zones of horizontal water vapor transported across mid-latitude regions (Zhu and Newell, 1998) known to produce extensive river flooding and deliver a disproportionate amount of precipitation to coastlines on which they occur (Dettinger et al., 2011; Lavers et al., 2011; Ralph et al., 2006; Viale and Nuñez, 2011). Models suggest the frequency and magnitudes of AR events may increase in the future (Dettinger, 2011). In the Santa Barbara Channel, a grey flood deposit dating to 1862 and at least five older events of similar or greater thickness were deposited during the last 2000 years (Hendy et al., 2013), suggesting a high potential for recurrence of these destructive storm seasons. According to the recent USGS ARkStorm and Cosmos models, a series of similar storms impacting the coast today would cost California over $700 billion in long-term economic losses (Barnard et al., 2014; Porter et al., 2011). This estimate includes modeled effects of the coastal impacts from erosion and inundation. However, little data is available to test model accuracy or identify areas of particular vulnerability for these coastal effects of AR storms.

Here we provide the first documentation of coastal overwash deposits from the 1861-2 storm season (Engstrom, 1996; Guinn, 1890). We mapped the deposits within Carpinteria Marsh, California, using an extensive suite of cores and a robust multi-proxy chronology derived from exotic pollen markers, spheroidal carbonaceous particles (SCPs), ^{210}Pb, ^{137}Cs, and ^{14}C data. Our objective is to use the characteristics and extent of this deposit to determine whether prolonged stormy periods, such as that of 1861-2, can create conditions necessary to erode coastal barriers and overwash low lying regions of the coast.

3.2 Study Site

Carpinteria Marsh (Figure 4) is a small, microtidal (tidal range 1.01 m) estuary located along the east-west trending coastline of the Santa Barbara Channel (Ferren, 1985). The marsh lies within the Carpinteria basin syncline and has experienced 1.2 ± 0.4 mm a^{-1} of subsidence over the last 6 ka (Simms et al., 2016). Although the marsh today is a small fragment of a once larger estuary, the 0.93 km^2 (230 acres) that remain contain a high-resolution record of Holocene environmental changes along the Santa Barbara coastline (Ferren, 1985).

The Santa Barbara Channel mainland has been occupied by humans for at least 10,000 years (Rick et al., 2013), and permanent European settlements were established by the late 1700s. European species of crops were introduced in small quantities in Santa Barbara and Ventura Counties throughout Spanish and Mexican settlement (1782-1850), but large-scale agriculture was established in Carpinteria Valley only after the initiation of the American period from 1850 to present (Caldwell, 1979; Ejarque et al., 2015).

Much of the pre-historic Carpinteria marsh was filled for agriculture and development between the late 1800s and the present day (Caldwell, 1979). Although little historical information is available on the marsh prior to the 20th century, a coastal survey map from 1869 (Grossinger et al., 2011) indicates that the marsh was once separated from the ocean by an ~150 m wide sandy dune and beach barrier that intermittently closed the estuary to tidal flow (Figure 4). The railway was built on the northern border of the marsh in 1887, which accelerated development of the town (Caldwell, 1979).

Prehistorically, at least four streams drained into Carpinteria Marsh; however, today only Santa Monica and Franklin Creeks enter the marsh (Ferren, 1985). Streams along the Santa Barbara channel are prone to flashy, storm-driven flow, most of which occurs during the winter season (Warrick and Mertes, 2009). Historical storms, including those in 1914 and 1938, resulted in large overbank floods in downtown Carpinteria, as well as coastal erosion of dunes east of the marsh (Caldwell, 1979; Ferren, 1985). In response to repeated flood damage, debris basins were installed at canyon mouths to prevent coarse sediment from being carried into town, and Santa Monica and Franklin Creeks were channelized beginning in 1966 (Ferren, 1985). Despite the impact of numerous El Niño and Atmospheric River storms in Carpinteria in the 20th and 21st centuries, a comparison of a 1929 aerial photograph of Carpinteria Marsh (Special Research Collections, 1929) to current satellite images shows no evidence of coastal overwash deposition and no large geomorphic change (channel migration, etc.), other than that related to direct anthropogenic influence, since 1929 (Figure 4).

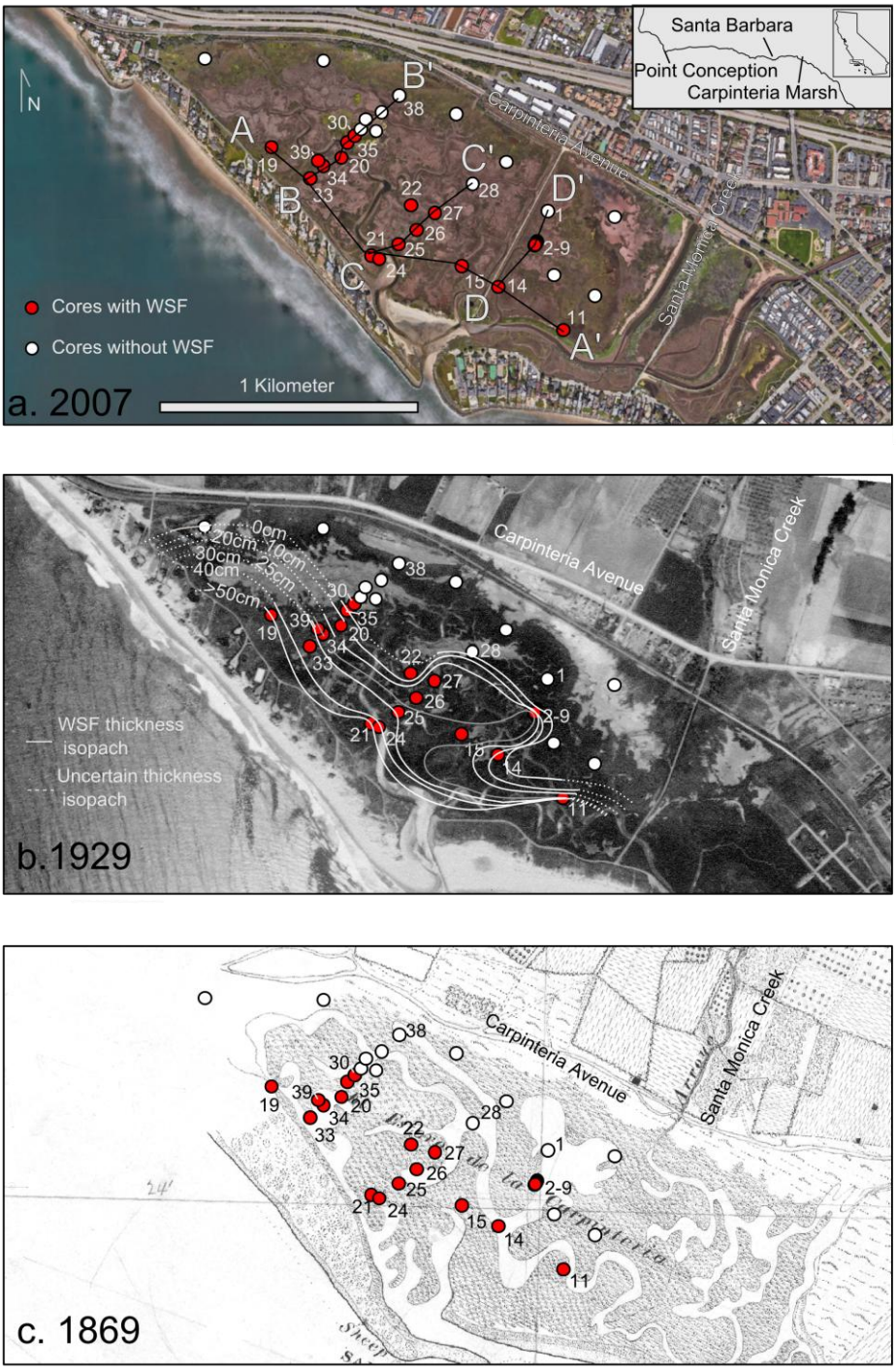


Figure 4. Location map. 1869 map (c), 1929 aerial photograph(Special Research Collections, 1929) (b), and 2012 satellite image (a) of Carpinteria marsh with core locations and transects superimposed. Cores with candidate overwash deposit White Sand Facies (WSF) are shown in red, cores without beds of WSF are colored white. Locations of transects A, B, C, and D, shown in detail in Figure 5, are noted in (a). An isopach map of WSF bed thickness is overlain on the middle (1929) panel (b). Lines of equal thickness for the candidate 1861-2 overwash deposit are shown. Isopach lines are dotted where uncertain.

3.3 Methods

3.3.1 Core collection and physical sedimentology

We collected 43 vibracores up to 4 m in length to document historical and prehistorical environmental changes in Carpinteria Marsh (Figure 4). We used a Garmin handheld GPS or Topcon differential GPS to determine core coordinates. Core top elevations were determined from either Topcon differential GPS or from vegetation-corrected LiDAR collected in 2003 (NOAA, 2009-2011; Sadro et al., 2007) for cores for which differential GPS elevations were unavailable. Cores were split; imaged; described for sedimentary structures, organic content, shell content, and color; and sampled for grain size, quartz-feldspar-lithics (QFL) ratios, and chronological markers.

We analyzed 117 core samples for grain size, targeting cores with candidate overwash deposits. For each candidate overwash deposit, we sampled from the base to the top of the deposit at 1-5 cm resolution. We also sampled modern beach and dune environments at Carpinteria State Beach and modern sediments from Carpinteria Creek for grain size. The mouth of Carpinteria Creek enters Carpinteria State Beach ~1.75 km east of the mouth of Carpinteria Marsh. Unlike Santa Monica and Franklin Creeks, Carpinteria Creek is unchannelized and free of debris basins in its watershed. The sediments of Carpinteria Creek are therefore more representative of historical and prehistorical stream sediments in Carpinteria and more comparable to any alluvial sediments found in cores.

Sediments were pretreated for grain-size analysis with a 3-hour boil in 30% hydrogen peroxide to remove organic matter, and suspended in 10% hexametaphosphate (Kirby et al., 2014). We did not remove carbonates because a test of grain size on samples with and without carbonate removal showed no significant difference in the grain-size distribution.

Grain-size distributions were analyzed using a CILAS 1190 laser diffraction system. We used GRADISTAT to calculate grain-size statistics (Blott and Pye, 2001).

3.3.2 Pollen Analysis

Samples from CM20 and CM15 were processed for pollen analysis at 5-10 cm resolution, using modified standard pollen preparation procedures (Faegri et al., 1989). CM20 and 15 were chosen because both cores include a candidate overwash deposit interbedded with laminated, fine-grained sediments, which are likely to preserve pollen. Siliceous and carbonate material were removed by digestions in HF and HCl, respectively. Further removal of siliceous material was accomplished through a density separation using lithium polytungstate (LST) at a density of 1.9 g/cm^3. Samples were acetolysized and treated with KOH to remove humic acids, suspended in glycerol, mounted on slides, and identified and counted on a light microscope at 400X and 1000X magnification. Pollen and fungal spore identification followed published illustrations and morphological keys (Punt et al., 1976-2009; Reille, 1992; van Geel and Aptroot, 2006) and the Northern Arizona University Laboratory of Paleoecology's pollen reference collection. At least 300 and 400 terrestrial pollen grains were counted per sample in CM15 and CM20, respectively. Pollen and spore values are expressed as a percentage of the total terrestrial pollen sum, excluding Cyperaceae, fern spores, aquatic plants and Chenopodiaceae (full diagrams in Appendix B). Pollen and spore diagrams were graphed using C2 software v.1.7.2 (Juggins, 2011).

3.3.3 Spheroidal Carbonaceous Particle Analysis

Spheroidal carbonaceous particles (SCPs) are porous spheroids of mostly elemental carbon produced by the incomplete combustion of hydrocarbons at high temperatures

(>1000 ^{o}C) (Rose, 2015; Ruppel et al., 2013; Swindles et al., 2015). SCPs are aerially deposited markers of regional industrial activity (Ejarque et al., 2015; Swindles et al., 2015). Samples from CM20 and CM15 were analyzed for SCPs at 2.5-10 cm resolution following Ejarque et al. (2015), which uses a modified Rose (1990, 1994) procedure. Five cc of sediment were freeze-dried and weighed. Organic, siliceous, and carbonate material were removed in a series of digestions in concentrated nitric acid, HF, and HCl. Samples were sieved through 5 μm sieves, suspended in glycerol, mounted on slides, and counted at 400X resolution. SCPs were identified using a reference collection (Ejarque et al., 2015; Rose, 2008) and standard characteristics. These characteristics include black color, close to spheroidal shape (axes between 0.7 and 1), and presence of one or more pores (Rose, 2008). *Lycopodium clavatum* spore tablets (Stockmarr, 1971) were added in order to calculate SCP concentration. One to three whole slides were counted for each sample, equating to 300-700 *Lycopodium* grains. Although small SCPs (2-20 μm) have been identified in Arctic and Antarctic regions far from their source (Rose et al., 2012), this study would likely have picked up only regional to local signals due to the lowered detection limit due to removal of <5 μm particles during processing.

3.3.4 Age-Depth Models

Because of large uncertainties in calibration of radiocarbon data for the historical period, we developed age-depth models for CM20 (Figure 6) and CM15 (Figure 7) from multi-proxy chronologies derived from radiocarbon; exotic pollen markers (including pollen evidence of agricultural activities); coprophilous fungal spores (related to domestic grazing); and spheroidal carbonaceous particle stratigraphy. We assign ages to the first appearance of

Eucalyptus (gum) pollen in the sedimentary record, as well as the first decrease in *Quercus* (oak) and concurrent increase in crop pollen (Figure 6, 7). *Eucalyptus* trees were first introduced in Santa Barbara by American settlers in 1870 (Ejarque et al., 2015; Esau, 2006), and in 1876 historical documents attest to the presence of groves of this tree in Carpinteria Valley (Caldwell, 1979). Therefore, we assign the first appearance of *Eucalyptus* pollen to the calendar year 1875 ± 5 years. In the early American period in Carpinteria Valley (1850-1860s), settlers cleared the land for ranching activities and cultivation, mainly for fruit and nut orchards (Caldwell, 1979; Campos, 2007). We therefore assign the decrease in *Quercus* and contemporaneous increase in crop pollen and coprophilous fungi to the beginning of this period, calendar year 1850 ± 5 years.

Because the concentration of SCPs in sediments has been found to correlate with regional industrial activity (Ejarque et al., 2015; Ruppel et al., 2015), SCPs can be used as chronological markers if a robust historical record of combustion sources exists. Comprehensive and direct emissions data for the historical period in California are not available, but Bond et al. (2007) used estimates of consumption and population statistics to model black carbon emissions around the world from 1850 to 2000. We summed Bond et al. (2007) output data covering the California region (30-42^{o}N, 112.5-123.5^{o}W) for decadal estimates of black carbon emissions (Figure 6, 7). Additionally, records of crude oil production for Santa Barbara and Ventura counties, which have been shown previously to correlate with SCPs (Ejarque et al., 2015), are available from 1876 onwards (Schmitt et al., 2002).

Oil production, which started in Carpinteria with the first attempts to distill oil from asphaltum in 1857 (Gilbert, 2004), occurred at temperatures of ~650 ^{o}C (Rothwell, 1904), too low to produce SCPs. However, if powered by coal, steam-powered rigs and trains

associated with oil production would produce SCPs. Historical records indicate that the first steam-powered rig was drilled in Ojai in 1866 (Schmitt et al., 2002) and the first steam-powered train passed through Carpinteria in 1887 (Caldwell, 1979). By the turn of the 20th century, steam rigs began to be powered by oil (Rintoul, 1976). Therefore, SCPs may have been produced as early as 1866, and were more certainly produced in measurable quantities by regional industry and trains in the late 1800s. To incorporate the uncertainty in initial production of SCPs in Santa Barbara and Ventura counties, we assign the first appearance of SCPs in the sediment record to calendar year1880 ± 15 years.

Although the crude oil production record (Adamson, 2002, 2008, personal communication; Nehring, 1975; Schmitt et al., 2002) and models of black carbon output (Bond et al., 2007) since the mid-late 1800s in California have different magnitudes of changes, they agree on direction of change through time: each record initiates in the mid-1800s and slowly increases until ~1900, at which point production and emissions both accelerate. Production and emissions peak in the 1950s during the post-World War II industrial boom, after which point both records show a decline to present values associated with slowed production and the introduction of aerosol filtering systems. These values generally agree with other independently dated SCP records compiled from lakes and estuaries around the world (Swindles et al., 2015) and in southern California (Ejarque et al., 2015). Therefore, we assign the peak in SCP concentrations to calendar year 1955 ± 5 years (Table 4).

We used BChron (Parnell et al., 2008), a Bayesian modeling program, to develop an age depth model for CM20 and CM15. BChron calibrates radiocarbon ages with IntCal13 (Reimer et al., 2013) and uses Monte Carlo methods to estimate errors on predicted ages. Modern radiocarbon ages were calibrated with CALIbomb (Reimer et al., 2004), with each 2

σ calibrated age range approximated in BChron as normally distributed (Table 5.). We assume a normal distribution for the uncertainty of non-radiometric ages and include an input for vertical uncertainty (sampling resolution).

3.3.5 ^{210}Pb and ^{137}Cs Analysis

We compare our pollen and SCP-based chronology in CM20 and CM15 to an age-depth model for CM34 established from ^{210}Pb and ^{137}Cs activity. CM34 was the closest and most stratigraphically comparable core to CM20 with enough sediment available for analysis (Figure 4, 6). Both ^{210}Pb and ^{137}Cs activities were determined by gamma spectroscopy using a High-Purity Broad Energy Germanium Gamma Detector. Twelve sediment samples packed in petri dishes, sealed, and aged for at least 20 days to ensure secular equilibrium between ^{226}Ra and the measured daughter isotopes (^{214}Pb and ^{214}Bi), were used to determine supported ^{210}Pb. After the 20-day incubation period, the samples were counted for at least 24 hours. Total ^{210}Pb was determined from the gamma peak at 46.5 keV, while supported ^{210}Pb was determined by measuring the peaks of ^{214}Pb (at 295 keV and 351.9 keV) and ^{214}Bi (at 609 keV), daughters of ^{226}Ra.

The ^{210}Pb activities were corrected for self-absorption, and excess ^{210}Pb ($^{210}Pb_{ex}$)was then determined for each sample by subtracting the measured supported ^{210}Pb from the total ^{210}Pb. ^{137}Cs was measured concurrently in each sample from the gamma peak at 661 keV. While ^{137}Cs can serve as an independent chronometer to ^{210}Pb, it may be displaced downward in the core due to diffusion or biological mixing in the sediment (Santschi et al., 1983). Therefore, we rely primarily on the ^{210}Pb data, and interpret the ^{137}Cs data with

caution. Both $^{210}Pb_{ex}$ and ^{137}Cs activities were decay corrected to the time of collection, and uncertainties were propagated from the counting statistics.

Table 4. Age-Depth Values

CM15	Age Years BP*	Age A.D.	Age SD	Depth BGS	Depth Error	Notes
Top of Core	-62	2012	1	0	0	
Peak SCPs	-5	1955	5	30	5	a
First Appearance of *Eucalyptus*	75	1875	5	31	10	b
First Appearance of SCPs	70	1880	15	35	5	c
CM20						
Top of Core	-62	2012	1	0	0	
Peak SCPs	-5	1955	5	22.5	2	a
First Appearance of *Eucalyptus*	75	1875	5	55.5	5	b
First Appearance of SCPs	70	1880	15	55	1	c
American Period	95	1855	5	83	5	d

a. Crude oil production peaked in southern California in the 1950s (Schmitt et al., 2002). Black carbon emissions modeled for southern California peak in the 1950s as well (Bond et al., 2007) which corresponds to SCP peaks from around the world (Swindles et al., 2015).

b. First reference to gum trees in Carpinteria 1876 (Caldwell, 1979). *Eucalyptus* was introduced to Santa Barbara County in 1870 (Ejarque et al., 2015). Because it is an insect pollinated species, only very local signal would be recorded (Mudie and Byrne, 1980a). Therefore, we assign the first appearance in the sedimentary record to between 1870 and 1880 AD.

c. Crude oil production began in Ventura County in 1865, using a steam-engine powered drill rig (Schmitt et al., 2002). An asphalt mine and refinery were active in Carpinteria on and off from 1857 to the 1920s (Caldwell, 1979; Gilbert, 2004).Although it is unclear if the early production methods would have generated SCPs, the steam engine trains through Carpinteria starting in 1887 would have likely been powered by coal and therefore would have produced SCPs. Most SCP records around the world begin in the 1850s-1900s (Swindles et al., 2015).

d. Decrease in oak pollen, increase in crop pollen and dung-related fungi. 1850-60 Carpinteria's population becomes well established and land is cleared for cropland and ranchland (Caldwell, 1979; Stockton, 1960).

* Where present is 1950 AD

Table 5. Radiocarbon Ages

Lab	Lab No.	Material Description	Core	Sample Depth BGS	14C age	14C error	lower cal range BP	upper cal range BP	median probability	Notes
UCIAMS	115623	Charcoal	15	40	180	20	1	286	183	
UCIAMS	115624	Charcoal	15	69	5170	20	5905	5986	5926	a
YAUT	26733	plant fragments	15	123	19	40	255	-6	80	b
UCIAMS	186408	plant fragments	15	224	130	20	11	270	119	
UCIAMS	186406	plant fragments	19	67	225	20	1	305	209	
UCIAMS	186405	plant fragments	19	129	830	30	688	789	737	
UCIAMS	115625	Charcoal	20	59	255	20	154	421	299	
UCIAMS	115626	Insect parts	20	86	185	20	1	287	181	
UCIAMS	186407	plant fragments	20	110	660	15	564	667	598	
UCIAMS	186401	plant fragments	20	225	1395	15	1289	1330	1303	

a Stratigraphically out of order, removed from age model

b Calibrated with CALIBOMB (Reimer et al., 2013; Hua et al., 2013) Two sigma age ranges were modeled as normally distributed ages in BChron according to their relative probability, as indicated below and shown in Figure 7.

[cal BP -6 :cal BP -5]0.030-- not included in BChron model
[cal BP 31 :cal BP 85]0.519-- used twice in BChron model
[cal BP 86 :cal BP 138]0.236-- used once in BChron model
[cal BP 223 :cal BP 256]0.216-- used once in BChron model

3.4 Results

3.4.1 Stratigraphy and Facies

The overall stratigraphy of the top 4 m of sediment in Carpinteria marsh can be summarized as 1-3 m of basal grey sand overlain by interbedded brown mud and sand. In the top meter of sediment in 20 cores, the upper brown mud and sand is interrupted by one 1-50 cm thick white-grey sand layer (Figure 5). We define four sedimentary facies based on sedimentary structures, nature of contacts, grain size, mineralogy, organic and shell content, and color.

3.4.1.1 Mud Facies (MF)

Mud Facies (MF) is characterized by organic-rich, fine-grained sediment (clay to fine sand, mean grain size <50 μm). MF is massive, mottled, or laminated, with colors ranging from blue-grey to red-brown. Whole and partial *Cerithidea californica* (California Horn Snail) shells are common, while other shell fragments are rare. MF contains sparse marsh and mud flat foraminifera, dominated by *Trochiammina inflata* and *Milliammina fusca*. Beds of MF range in thickness from a few cm to close to a meter and are found at the surface of the marsh today, and in the basal portions of the four cores that reach 4 m below the ground surface. Beds of two other facies, White Sand Facies (WSF) and Brown Sand Facies (BSF), are interbedded with beds of MF.

3.4.1.2 Grey Sand Facies (GSF)

GSF is a dark gray, poorly sorted sand (fine to medium sand, mean grain size 50-150 μm) with few muddy silt lamina and lenses. GSF tends to be more poorly sorted than modern beach or dune sediments (Appendix B). GSF is frequently mottled or faintly laminated. GSF is devoid of foraminifera, but contains abundant shells and shell fragments of estuarine and intertidal species including *Ostrea* spp., *Saxidomus nuttallii, Macoma nasuta*, and *Leukoma laciniata.* Beds of GSF are over 1.5 m thick in places and either grade into or are sharply overlain by beds of MF or BSF. The basal bed in 20 vibracores is composed of GSF. GSF is found stratigraphically below the bed of WSF wherever they occur in the same core.

3.4.1.3 Brown Sand Facies (BSF)

BSF is a lithic-rich, fine brown sand. BSF consists of 10-60 cm thick beds of poorly sorted sandy silt to medium brown sand (mean grain size ranges from 20-112 μm), with scattered granules. The dominance of lithic grains and poor sorting of BSF is similar to the characteristics of modern stream samples (Appendix B). BSF is devoid of foraminifera and shell fragments of any kind. BSF beds are thickest, coarsest, and most frequent within the inland-most cores of the marsh (CM16, 17, 18). Beds of BSF are found interbedded with beds of MF.

3.4.1.4 White Sand Facies (WSF)

WSF consists of a moderately sorted, light-gray, quartz-rich sand layer. One bed of WSF occurs in the upper meter of sediment in 20 cores. The basal contact of the WSF bed with MF (15 cores) or GSF (5 cores) is sharp or erosional. The upper contact of the WSF bed with MF is sharp or gradational. In the 5 cores in which a WSF bed directly overlies GSF, we assigned the shallowest erosional surface present as the base of the WSF bed. In these cases, measured thickness is a minimum. When the top contact is gradational, the deposit is often mottled and burrowed. The total thickness of the deposit thins with increasing distance from the beach from 58 cm to 1 cm (Figure 4).

The majority (17/20) of occurrences of WSF contain normally graded or ungraded parallel laminations of sand and silt (WSF-L); dipping laminations were only observed in CM2. Where not laminated, the grain size characteristics of WSF are most similar to modern beach and dune samples (Appendix B). The maximum mean grain size within each bed of WSF (150-250 μm) decreases with increasing distance from the beach. WSF is devoid of shell fragments and foraminifera tests.

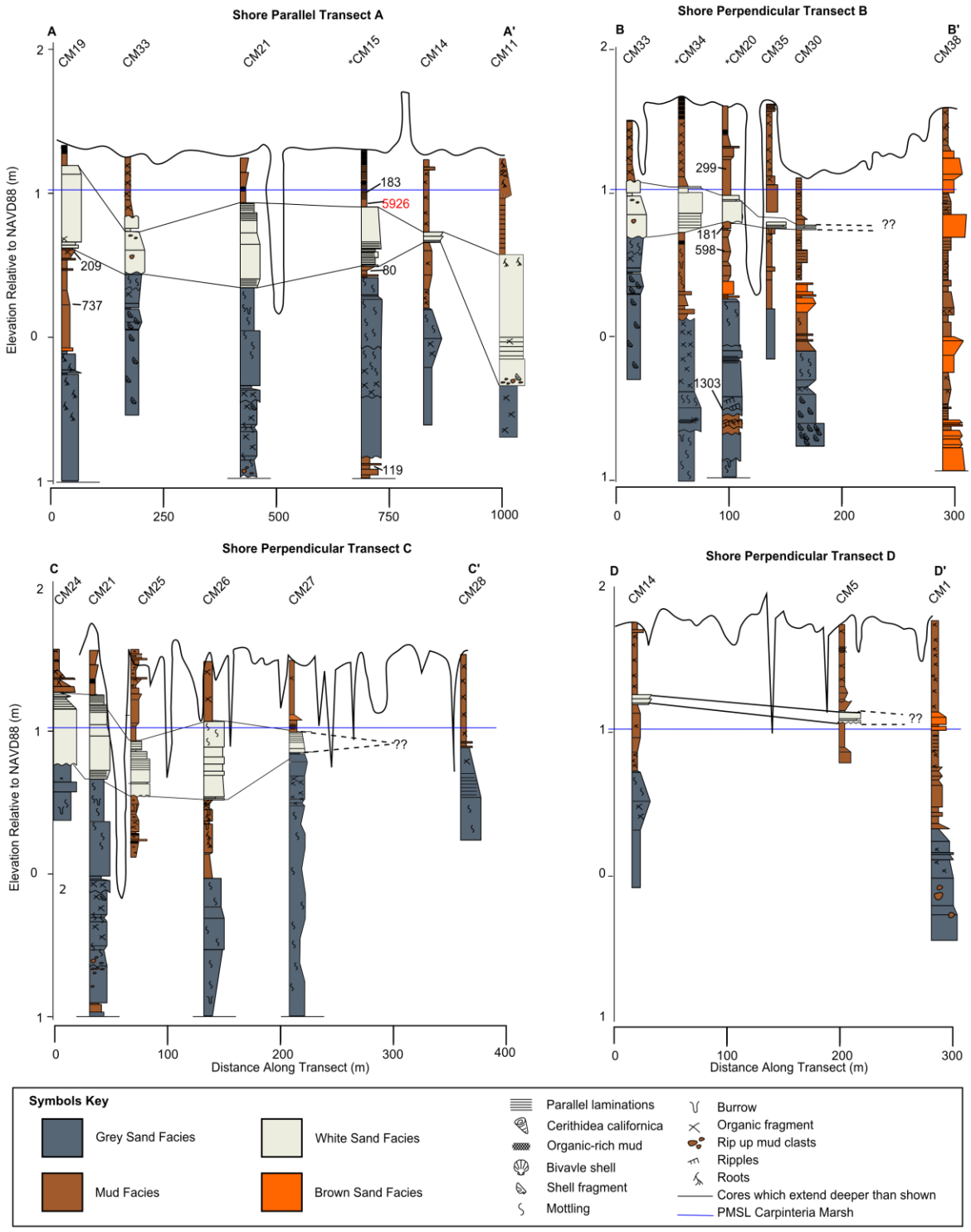


Figure 5. Core stratigraphy. Stratigraphy through shore parallel and shore perpendicular transects labeled in Figure 4. Bed width represents grain size, color corresponds with facies. Note horizontal scale under each transect is the same for transects B, C, and D. Cores CM15, 20, and 34 are shown in more detail, along with related chronological information, in Figures 4, 5, and 6, respectively

3.4.2 Age-Depth Models

Table 4 summarizes the depth of the pollen-, spores-, and SCP-based chronological markers identified in CM15 and CM20. In both CM15 and CM20, we have identified the first appearance of *Eucalyptus*, evidence for European influence, the introduction of SCPs, and the peak of SCP deposition (Figure 6, 7). The transition from the Mexican to American Periods, characterized by a depression in *Quercus* pollen and rapid increase in crop pollen, can only be distinguished in CM20.

The age model for CM34 relies entirely on ^{210}Pb and ^{137}Cs activities (Figure 8). $^{210}Pb_{ex}$ decreases exponentially in the top 30 cm of sediment, and using the Constant Flux Constant Supply model (CFCS, Appleby and Oldfield, 1983) we can calculate an average sedimentation rate of 0.37 ± 0.04 cm a^{-1} for this section of the core. The peak value of ^{137}Cs observed in CM34 occurs at 29 cm depth. If this peak is in place, it likely represents a time period of 1953-1963. However, the $^{210}Pb_{ex}$ data suggests the modern mixed layer is between 3 and 9 cm deep; therefore, Cs could be mixed downward as much as 9 cm in the core. We assume a 9 cm mixed layer, which brings sedimentation rates based on the ^{137}Cs chronology in alignment with rates calculated based on the $^{210}Pb_{ex}$ data. The absence of laminations and parallel bedding above WSF in CM34 supports the presence of bioturbation influence on the Cs stratigraphy.

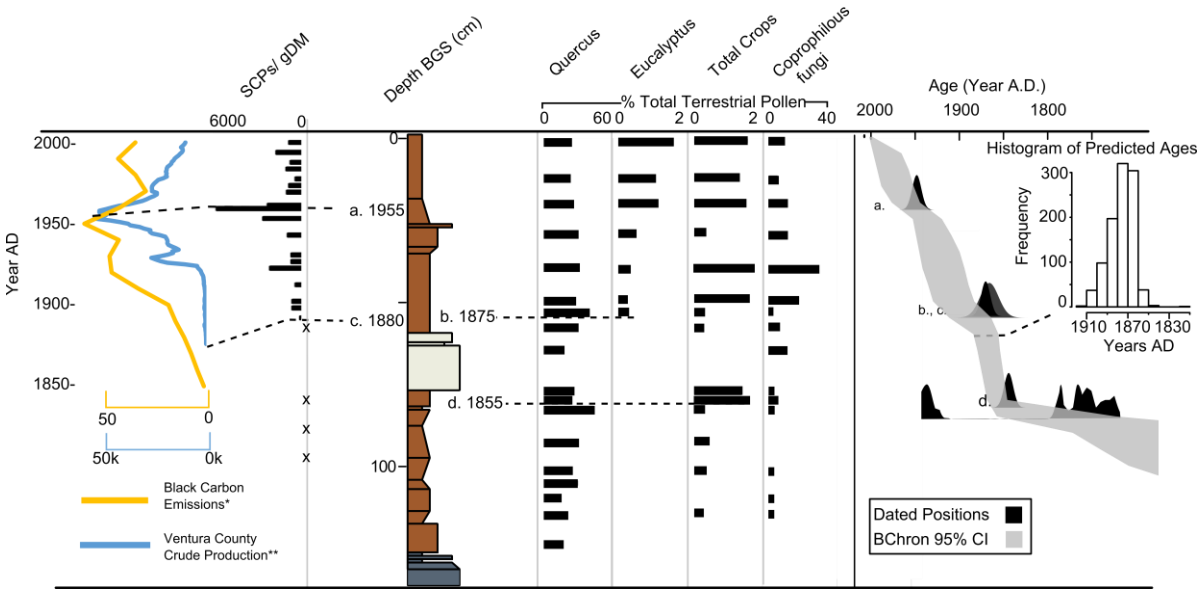


Figure 6. Stratigraphy and chronology of CM20. Pollen, SCP, and ^{14}C data used in age model. "X" symbols on SCP plot indicate samples sampled, but devoid of SCPs. The BChron generated age model for CM20 is shown on the right with a histogram of ages predicted for the top of the WSF bed. *Bond et al., 2007; ** Schmitt et al., 2002; Adamson et al., 2002; Adamson et al., 2008; Adamson, personal communication.

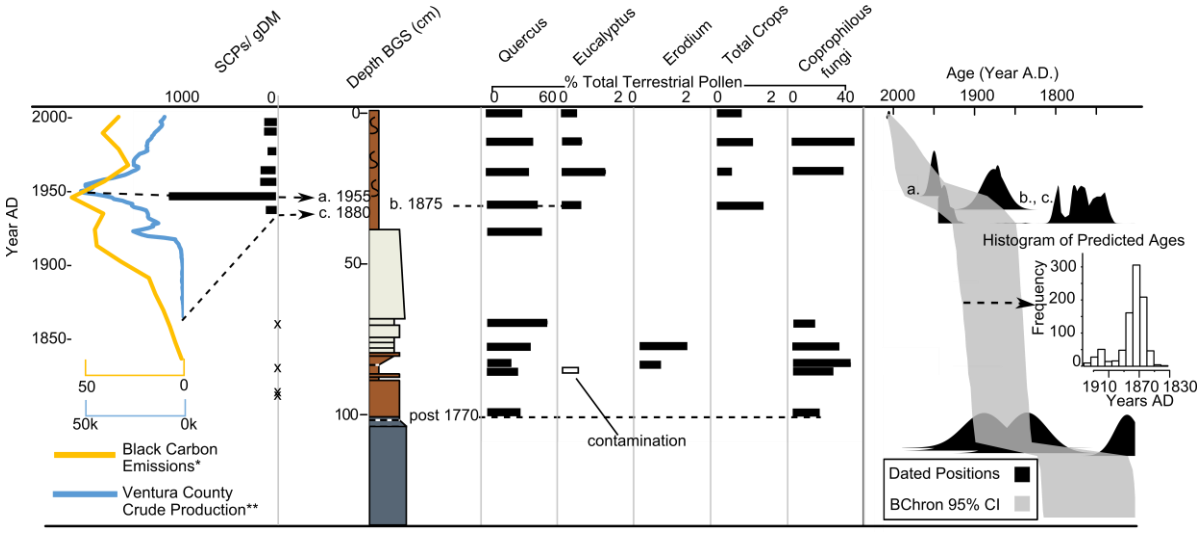


Figure 7. Stratigraphy and chronology of CM15. Pollen, SCP, and ^{14}C data used in age model. "X" symbols on SCP plot indicate samples sampled and found to be devoid of SCPs. The BChron generated age model for CM15 is shown on the right with a histogram of ages predicted for the top of the WSF bed. Two grains of *Eucalyptus* were found at 86.5 cm BGS in a mud-filled burrow. No SCPs were found in this layer, nor in samples above and below, which were devoid of *Eucalyptus*. This sample was interpreted to represent contamination by modern material. *Bond et al., 2007; ** Schmitt et al., 2002; Adamson et al., 2002; Adamson et al., 2008; Adamson, personal communication.

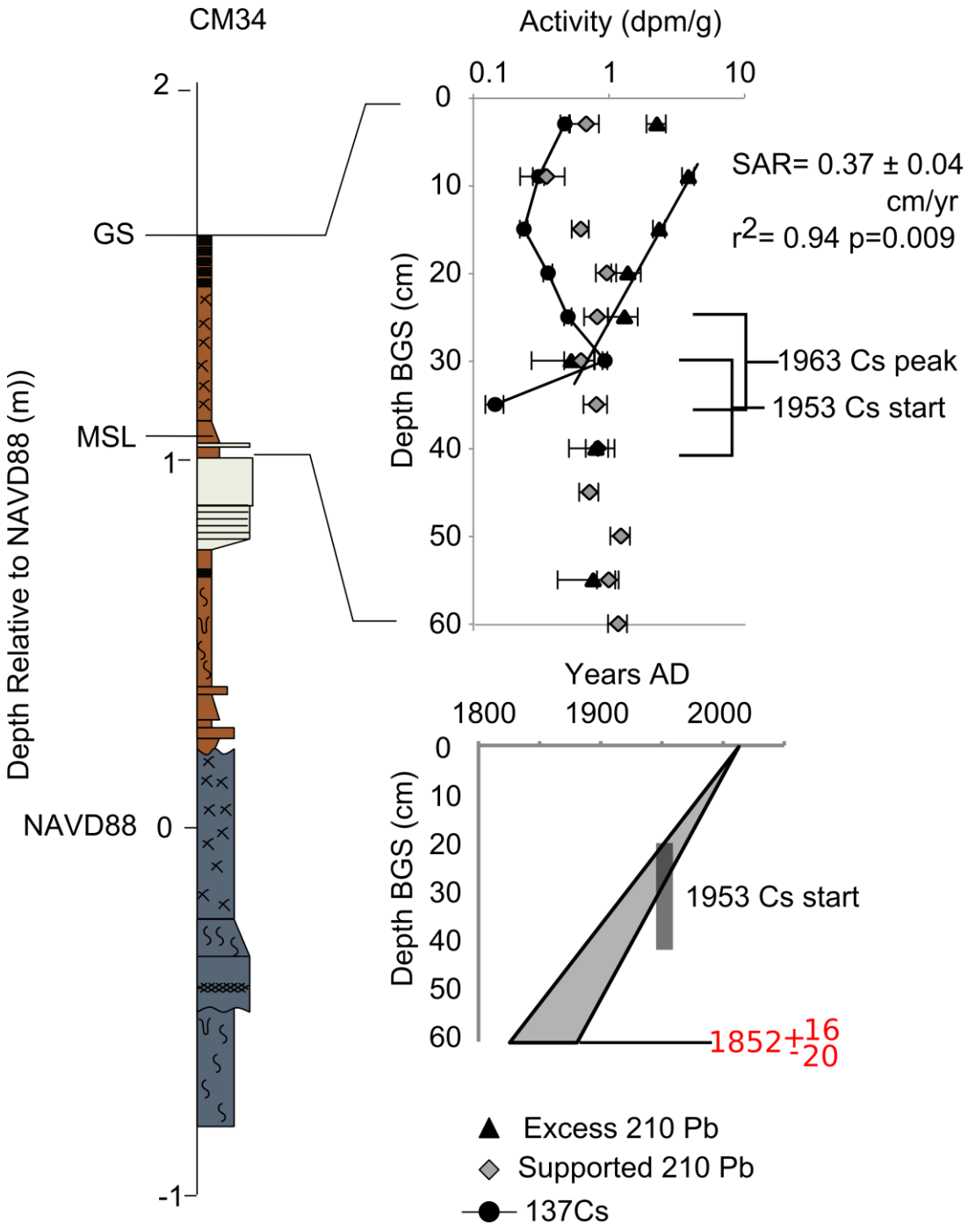


Figure 8. Stratigraphy and chronology of CM34. Uncertainty of Cs-137 start in linear age-depth graph indicates both sampling resolution and potential 9 cm mixed layer. Age in red is modeled age for the top of WSF in CM34.

3.5 Discussion

3.5.1 Facies Interpretation

Based on sedimentary characteristics and invertebrate composition, GSF is interpreted to represent deposition in an intertidal to subtidal, marine-influenced estuarine environment. MF is interpreted to represent intertidal to supratidal marsh surface and mudflat deposits, similar to what is observed throughout the marsh today. Beds of BSF, confined primarily to the most landward cores in the vicinity of paleostream mouths, are interpreted to represent alluvial fan deposition before the post-1966 flood control channelization of Carpinteria streams (Ferren, 1985).

The transition from dominantly GSF to interbedded MF and BSF beds in the upper stratigraphy of the marsh represents a shallowing of the estuarine environment through time. Pollen from exotic plants and crops –i.e. *Olea*, Cerealia-type, *Erodium*, *Plantago lanceolata*- and coprophilous fungal spores related to domestic grazing (i.e., *Sporormiella*-type, *Sordaria*) introduced during European settlement in the region (Ejarque et al., 2015)—begin to appear in the sedimentary record above the uppermost presence of GSF within CM20 and CM15 (Figure 6, 7). The pollen stratigraphy suggests that the transition from an open estuary to back-barrier marsh occurred around the beginning of Spanish settlement in the late 17th century, perhaps accelerated by increased fine-sediment load to the coast, as observed in other estuaries and coastal lakes in the region (Ejarque et al., 2015; Mudie and Byrne, 1980). Any storm overwash deposits older than European contact would be difficult to identify within the already marine-influenced GSF. Therefore, WSF is the only candidate overwash deposit identified in the Carpinteria stratigraphic record.

Because WSF is found in beds with a sharp or erosional basal contact, thins and fines landward, and is quartz-rich like beach and dune sands, we interpret it to represent deposition by a high-energy marine event that eroded and overwashed the barrier system in front of the newly established salt marsh and mudflats. The landward thinning and fining of the deposit, presence of parallel laminations, variation in grain size trends, and evidence for bioturbation of the upper part of the unit are similar to those characteristics observed in hurricane overwash deposits from the Gulf and Atlantic coasts (Donnelly et al., 2004; Hawkes and Horton, 2012; Hennessy and Zarillo, 1987). The deposit thickness is inversely correlated with base elevation, suggesting it infilled existing low marsh topography. The abrupt decrease in thickness at the landward edges of the deposit and presence of dipping lamina in CM2 may represent the avalanche face of the overwash fan as observed in modern storm deposits (Donnelly et al., 2006; Phantuwongraj et al., 2013).

3.5.2 Timing of deposition of WSF

The youngest radiocarbon dates beneath the WSF bed in CM15, CM19, and CM20 (Table 5) demonstrate that the bed was deposited more recently than 1650 A.D. Based on the pollen stratigraphy from CM20, WSF was deposited after the American period began in 1850 but before *Eucalyptus* trees were introduced to the region in the 1870s. Because WSF is interpreted to result from a potentially erosive event, we assume that the age of the top of the bed best represents the approximate age of deposition. The age model prediction of the median age for the top of WSF in CM20 is calendar year 1877 ± 24 years (2σ error) (Figure 6). The chronology of CM15 is less well resolved, but available chronological markers indicate the deposit was emplaced post-European contact (1770s), but before

industrialization (1880s), with a median predicted age from the BChron age-depth model of 1886 ± 52 years (Figure 7).

In CM34, the ^{210}Pb activity in the upper 30 cm gives an average sedimentation rate of 0.37 ± 0.04 cm a^{-1}. If we extrapolate this rate to the top of WSF at 60 cm, the WSF bed was deposited around calendar year 1852 +16/-20 (Figure 8). Therefore, all three chronologies place the deposition of WSF between 1840 and 1900, most likely between 1850 and 1880. The storms of 1861-2 resulted in the most prolonged and severe storm season recorded from the 1840s to the 1880s (Engstrom, 1996; Guinn, 1890), and therefore we interpret WSF to represent deposition related to the 1861-2 winter storms. Deposition of WSF enabled by barrier destruction may have continued for months, possibly years after the 1861-2 storms, but likely concluded before the 1870s (appearance of Eucalyptus and SCPs). This interpretation is supported by the decline of European crop pollen species directly above WSF in CM20 (Figure 6), which may correlate to the destruction of cropland by inundation related to the 1861-2 storms and the subsequent severe drought of 1862-5 (Engstrom, 1996; Guinn, 1890).

3.5.3 Implications

3.5.3.1 1861-2 winter storms' impacts on coast

While inland effects of the 1861-2 storms have been noted previously (Engstrom, 1996; Guinn, 1890; Porter et al., 2011), this deposit provides the first physical evidence that coastal erosion and inundation was produced by these storms. The coastal destruction may not have been historically documented outside of San Diego because of a general lack of observation in coastal areas—Engstrom (1996) notes that the Morro Bay spit was left off an

early (1842) map, even though radiocarbon data suggests it has been present since the mid Holocene (Orme, 1990). Estuaries forming in tectonic basins, such as Carpinteria Marsh, may also have a particularly high potential to preserve overwash deposits due to increased accommodation from subsidence (Simms et al., 2016). Additionally, tectonic estuaries often form outside of the influence of large rivers—the signal of large storm events in river mouth estuaries is likely to be dominated by fluvial discharge instead of marine inundation and wave activity.

The inland extent of WSF (over 450 m from the 1929 shoreline, Figure 4) is larger than 90% of the 717 penetration distances compiled from extreme historical hurricanes along the Atlantic and Gulf coasts (Morton and Sallenger, 2003). Long-duration or back-to-back storms are known to suppress barrier recovery, allowing for the maintenance of temporary inlets (Donnelly et al., 2006) and greater inland deposition (Morton and Sallenger, 2003), a scenario that may have occurred in Carpinteria Marsh during the 1861-2 storms. Today, the marsh rises less than 2.5 m over 500 m from the mouth to high marsh; this shallow topographic gradient may also have aided inland penetration.

The thickest deposits of WSF occur along transect C-C’ (Figure 4, 5), which intersects the shoreline at a location coincident with the zone of highest wave heights and greatest shoreline change predicted for Carpinteria Marsh by the COSMOS model in the ARkStorm scenario (Barnard et al., 2014; Porter et al., 2011). The deposit geometry suggests the storm surge breached the barrier at this location and potentially maintained a temporary inlet for the duration of the storm season, possibly longer. This location also coincides with a mapped opening in Quaternary conglomerate outcrops along the shoreline (Slade, 1975), although these outcrops are not mapped in other publications (Dibblee Jr and Ehrenspeck, 1986).

3.5.3.2 Differentiation of storm and tsunami deposits

Previous work from Carpinteria Marsh identified a number of candidate paleo-tsunami sand layers in the marsh (Wilson et al., 2014). While some of these deposits had characteristics associated with tsunami deposition, their source was ultimately determined to be inconclusive due to ambiguous microfossil and sedimentary evidence, as well as radiocarbon dating uncertainties (Wilson et al., 2014). Although it is unclear whether WSF correlates with any of these deposits, it shares sedimentary characteristics common to both tsunami and storm deposits, such as parallel laminations, normal grading, and grain size and mineralogical similarity to beach sands. While scale of inundation is often larger for tsunamis than for storms (Goff et al., 2012), recent field data and numerical simulations related to typhoon Haiyan have shown that variations in coastal topography can amplify storm wave heights and run up distances to values comparable to those from tsunamis (Shimozono et al., 2015).

Additionally, our age models suggest WSF was deposited in the 1860s, well after 1812, the year of the only near or far field tsunami thought to have impacted the coast of southern California in the 19th or 20th centuries with waves greater than 1 m amplitude (Toppozada et al., 2002; Wilson et al., 2014). Therefore, even in tectonically active regions without frequent hurricane activity, such as much of the California coast, other types of storms can produce large overwash deposits that would be challenging to differentiate from tsunami deposits outside of a historical context.

3.5.3.3 Implications for atmospheric river storms

Other work has suggested the 1861-2 storms were derived from Atmospheric Rivers (ARs) (Dettinger and Ingram, 2013). Although ARs are capable of producing extreme wind conditions (Waliser and Guan, 2017), the largest waves documented for California in recent decades were associated with El Niño storms, not recent AR storms (e.g., Allan and Komar, 2006). Reconstructing wave heights and interpreting the meteorological conditions responsible for the 1861-2 storms is beyond the scope of this study. However, emplacement of overwash deposits do not require anomalously large swell or wave heights if the duration of storm activity is long enough to continuously remove barrier deposits without allowing time for recovery. Therefore, if the 1861-2 storms were AR-derived events, the duration of storm activity may have created unique conditions not observed during other historical AR events. Consequently, mitigation efforts for these types of storms should consider the effects of coastal erosion and inundation in addition to the effects of excess precipitation.

3.6 Conclusion

Here we provide the first sedimentary evidence of coastal overwash deposition related to the 1861-2 storm season. We show that a multi-proxy chronology derived from exotic pollen markers, spheroidal carbonaceous particles (SCPs), ^{210}Pb, ^{137}Cs, and ^{14}C data allows us to robustly assign ages to estuarine sediments from the 19th century, a difficult time period from which to establish chronologies. Similar types of chronologies could be used elsewhere to differentiate between historical storm and tsunami deposits in coastal records. Although inundation from tsunamis and large storms associated with El Niño winters or smaller AR events are historically documented throughout the last 200 years in

southern California (Barnard et al., 2015; Guinn, 1890) no other event has created an overwash deposit in Carpinteria Marsh, suggesting that the 1861-2 storm season was far more destructive to coastal barrier systems in this location, and prolonged periods of AR storms may be more erosive than expected. This is particularly troubling considering coastal systems that once took the brunt of storm events—dunes, beaches, and estuaries—are today some of the most degraded and developed environments in coastal regions around the world. Preparations for future impacts of such events should take coastal erosion and overwash processes into account when predicting areas of vulnerability, and barrier systems should be prioritized for protection whenever possible.

CHAPTER 4

Reynolds, L.C., Simms, A.R., Rockwell, T.K., Yokoyama, Y., Mijairi, Y., Hangsterfer, A. Holocene coseismic subsidence along a non-subducting active margin. Submitted.

4. Holocene coseismic subsidence along a non-subducting active margin

Coseismic subsidence is a recurring hazard along coastlines associated with subduction zones. However, few studies have unequivocally demonstrated coseismic subsidence along other types of active margins. Here we show lithological, geochemical, and biological evidence for an abrupt subsidence event in an estuary along the highly-urbanized southern California coastline at 1.0 ± 0.1 ka. At an elevation of -2 to -4 m throughout the estuary, an organic-rich mud containing marsh invertebrates and geochemical signatures indicative of terrestrial influence is sharply overlain by a blue-gray sand containing intertidal and subtidal invertebrates and geochemical signatures of marine influence. Using relative sea-level indicators, we interpret this contact to represent up to 3.47 ± 0.5 m of coseismic subsidence, sediment compaction, and subsequent erosion. This event suggests that coseismic subsidence is not confined to coastlines near subduction zones but is also possible along other types of active margins including the densely-populated California coast.

4.1 Introduction

The hazardous effects of coseismic subsidence, demonstrated by historical events around the world, include immediate inundation of low-lying regions and increased susceptibility of broader coastal areas to future storm surges and sea-level rise (Hughes et al., 2015; Imakiire and Koarai, 2012; Jaramillo et al., 2017). Subsidence and subsequent marine inundation due to past coseismic events has been shown to be preserved in the sedimentary

record of estuaries (Atwater, 1987; Nelson et al., 1998; Nelson et al., 1996). However, differentiating coseismic subsidence from nonseismic processes that produce similar stratigraphic changes, such as floods, global mean sea-level (GMSL) rise, sediment flux-driven transgressions, local morphological changes (barrier breaching, mouth migration), or anthropogenic-induced subsidence, is difficult (Nelson et al., 1998), but necessary for proper hazard assessment.

Based on observations from coastlines associated with subduction zones, researchers have proposed criteria for identifying soils or marsh surface deposits submerged by coseismic subsidence. These criteria include evidence for RSL increase of more than a half-meter, rapid submergence (<1-3 mm contact), laterally extensive and synchronous contacts, and the presence of tsunami deposits (Nelson et al., 1998; Nelson et al., 1996; Shennan et al., 2016). At subducting margins, identification of subsidence due to plate flexure during great earthquakes has been aided by the ability to correlate stratigraphic changes and ages of events across a large geographic region (Leonard et al., 2004).

Subsidence may also occur along local structures, both on subducting coastlines and other types of active margins, such as that of southern California. Although long-term subsidence has been previously proposed as a main contributor to accommodation in fault-bounded estuaries in southern California (Simms et al., 2016), discrete coseismic subsidence events have not been frequently recognized in the stratigraphic record due to the difficulty in differentiating the effects of subsidence from other coastal processes. The only previous study to propose coseismic subsidence in southern California (Leeper et al., 2017) records buried marsh surfaces at elevations within error of where they would be expected to form based on paleo-RSL (Reynolds and Simms, 2015), and does not rule out alternative interpretations for the stratigraphic changes observed, such as contemporaneous storm

events recorded in the Santa Barbara Channel (Hendy et al., 2013) or the effects of anthropogenic subsidence in the Los Angeles Basin (Bawden et al., 2001; Takekawa et al., 2014).

Identifying and quantifying local subsidence remains a challenge for proper risk assessment and hazard mitigation in many populated coastal regions. Here we use an extensive suite of sediment cores and multiple relative sea-level indicators to show evidence for an abrupt environmental change in Carpinteria Marsh, southern California. The stratigraphic change observed is laterally continuous and synchronous throughout the entire estuary, dated to ~1.0 ka. It is interpreted to represent a sudden submergence of a paleo-marsh surface of more than 1 m, fitting many of the criteria previously established for identifying coseismic subsidence in the stratigraphic record.

4.2 Study Area

Carpinteria Marsh (34^{o} 24’ N 119^{o} 31’ W) is a 230 acre salt marsh along the central Santa Barbara Channel, a region characterized by mild, wet winters and warm, dry summers (Bakker and Slack, 1984) (Figure 9). The marsh is a remnant of a larger estuary that existed before infilling and development began in the 1850 s (Ferren, 1985). The marsh lies on the southern flank of the Western Transverse Ranges, a large east-west trending fold and thrust belt exhibiting rapid uplift since the Pliocene (Jackson and Yeats, 1982; Rockwell et al., 2016). The large east-west trending, north-dipping thrust faults in Ventura and Santa Barbara counties may have the potential for Mw 8 earthquakes (Rockwell et al., 2016). However, the subsurface geometry in the Ventura region and the relationship between the Red Mountain Fault (RMF), Ventura-Pitas Point Fault (V-PPF), and other thrust faults in the Santa Barbara

Channel south of Carpinteria (Figure 9) is subject to multiple interpretations (Hubbard et al., 2014; Jackson and Yeats, 1982; Johnson et al., 2017; Marshall et al., 2017; Rockwell et al., 2016).

The marsh lies within the axis of the Carpinteria basin, a small, faulted syncline separated from the Ventura Basin to the south by Plio-Quaternary movement along the RMF (Jackson and Yeats, 1982) (Figure 9c). The marsh is located on the down-thrown side of the south-dipping, out of syncline Rincon Creek Fault (RCF), a potential back-thrust from the RMF (Jackson and Yeats, 1982). The RCF displaces Quaternary sediments of the Santa Barbara Formation onshore(Fredrickson, 2016), and continues offshore, where it is likely responsible for uplift of the rocky reef off Sand Point, Carpinteria (Ferren, 1985), and may continue west into Santa Barbara as the Mesa Fault (Jackson and Yeats, 1982; Jennings and Saucedo, 1994). Previous work estimated 1.2 ± 0.4 mma^{-1} of subsidence in Carpinteria Marsh over the past 6 ka (Simms et al., 2016). However, the nature of the subsidence (slow or episodic) and the structures associated with this subsidence, remained unclear.

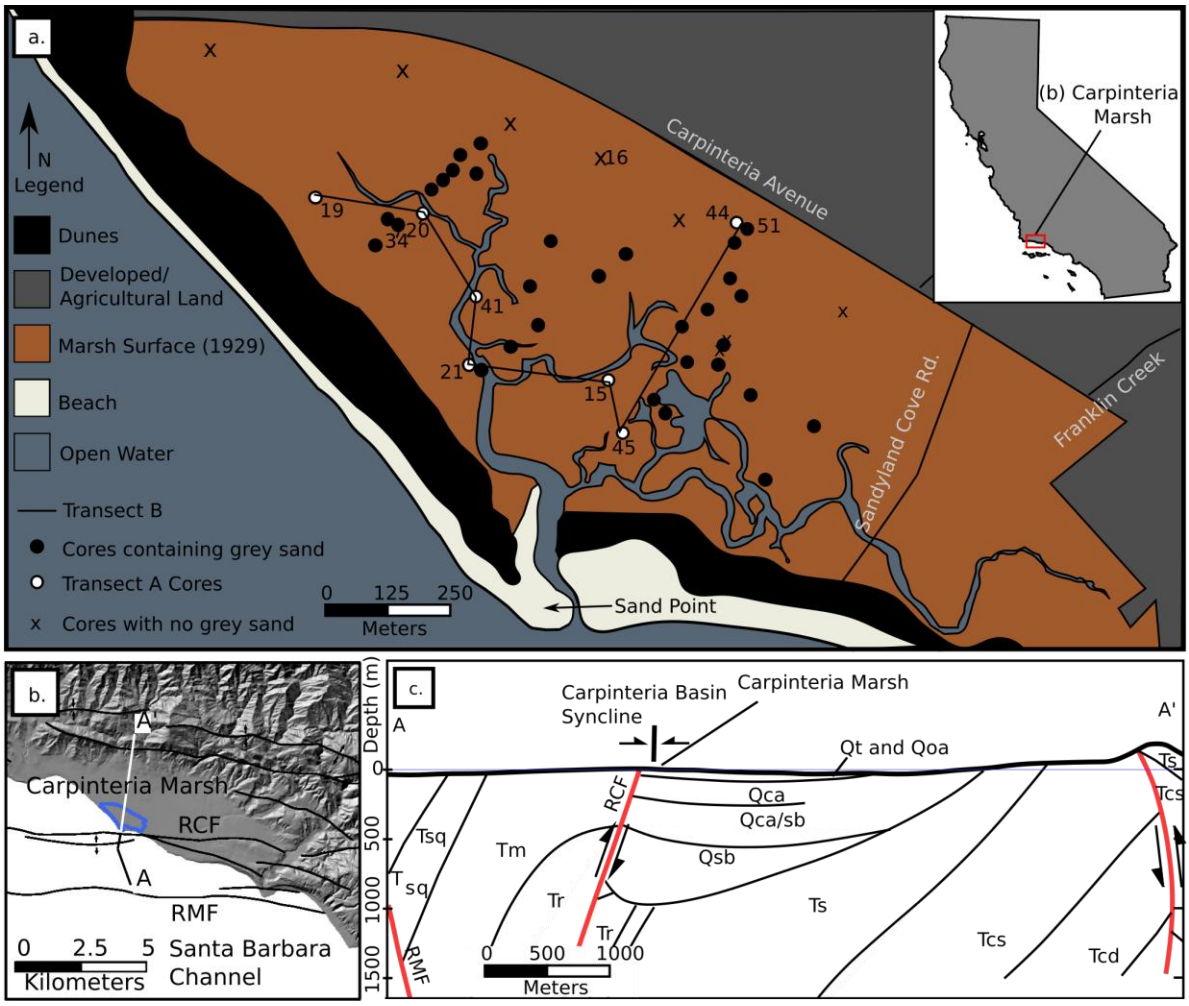


Figure 9. Location of Carpinteria Marsh—details traced from 1929 aerial photographs prior to much of the development currently affecting the marsh. Cores which sample the gray sand are shown by black circles, cores which reach the CSS are part of transect A, shown by white circles. Inset (b) shows major structures in region, adapted from Simms et al., 2016. The blue line represents the marsh boundaries shown in (a). Panel (c), adapted from Jackson and Yeats, 1982 and Simms et al., 2016, shows a cross section through A-A' (inset (b)).

4.3 Methods

4.3.1 Core collection and lithological analysis

From 2012 to 2017 we collected 44 vibracores up to 4 m below ground surface and seven Geoprobe 7822DT cores up to 14 m below ground surface. 23 of 51 core top elevations were determined using a Topcon differential GPS unit, while the remaining 28 core-top elevations were determined using high-resolution LIDAR, corrected for vegetation cover (NOAA, 2009-2011; Sadro et al., 2007). We described the cores and established sedimentary facies according to grain size, color, sedimentary structures, organic and shell content.

4.3.2 ^{14}C Analysis

75 organic, charcoal, and shell samples were sampled for radiocarbon analysis at the University of California Irvine Keck Carbon Cycle AMS Laboratory, while the remaining 26 samples were analyzed at the Atmospheric and Ocean Research Institute, The University of Tokyo (Yokoyama et al., 2010). Carbonate samples were subjected to a 30-50% leach and hydrolyzed with phosphoric acid before graphitization (Hirabayashi et al., 2017; Yokoyama et al., 2007). Humic acids were removed from organic samples by repeated treatments of HCl and NAOH before combustion and graphitization (Yamane et al., 2014). Radiocarbon ages and descriptions are listed in Appendix C and Supplementary Data.

4.3.3 $\delta^{13}C$ Analysis

Modern sediment and plant samples from Carpinteria marsh were collected, freeze dried, and shipped in the summer of 2016 to the Atmospheric and Ocean Research Institute, The University of Tokyo. 30 modern sediment samples and 175 sediment samples from CM46 were analyzed. We sampled CM46 at 5 cm resolution. All samples were freeze-dried, crushed with a mortar and pestle to a fine powder, and then treated with 3 N HCl at 100 °C for 2 hours to remove inorganic carbon. Next the samples were washed with 7 rinses of DI water and dried overnight. 5-150 mg of sediment or plant material was weighed into a tin capsule for analysis (amount dependent on estimated carbon content). A Delta V Advantage and Flash 2000 EA IRMS at AORI was used for isotopic analysis. Data was corrected for machine drift and amount-dependent deviations where necessary. Repeated analyses of internal standards indicate a 1 σ uncertainty of 0.43‰.

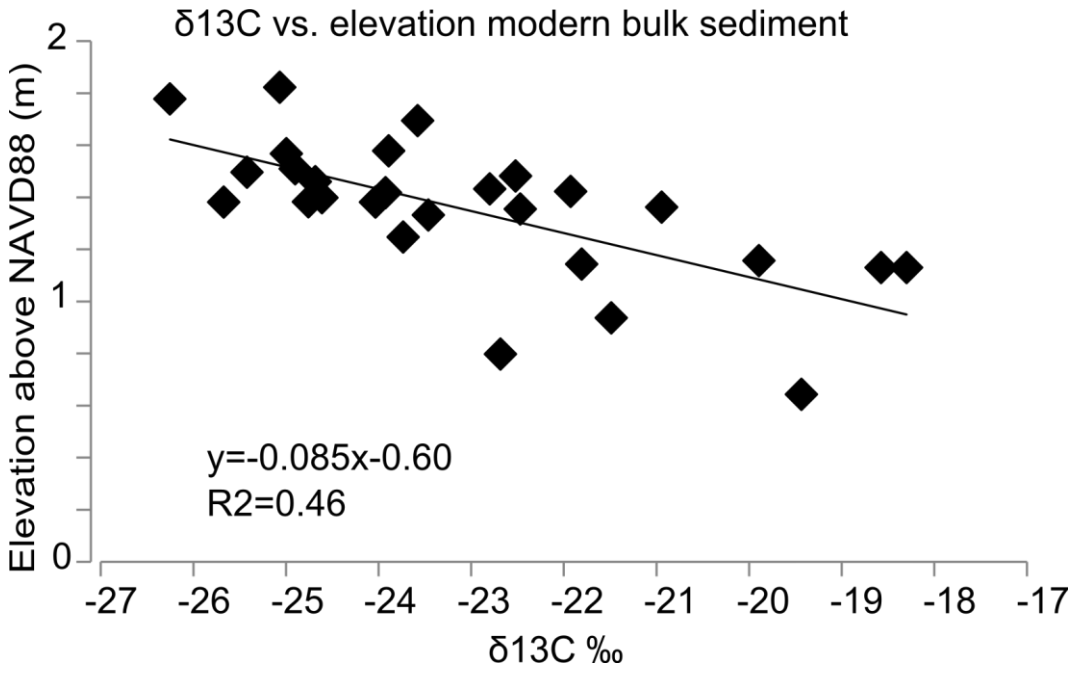


Figure 10. Modern δ^{13}C measurements in Carpinteria Marsh.

4.3.4 X-Ray Fluorescence (XRF) Analysis

CM46 was scanned at 0.2 mm resolution on an Avaatech X-Ray Fluorescence (XRF) core-scanner at Scripps Institution of Oceanography in 2013 at 10, 30, and 50 keV, measuring a suite of 29 elements. X-ray spectra were processed following Addison et al., 2013. Because water content can affect elemental counts, we followed other authors and used log ratios relative to a heavy element (Ti) to compare different elemental values between core sections (Addison et al., 2013; Hennekam and de Lange, 2012; Weltje and Tjallingii, 2008).

4.3.5 Cerithidea Elevation Survey

We surveyed *Cerithidea californica* from Carpinteria marsh in January of 2016 to determine their relationship to sea level in Carpinteria. We measured three transects, tabulating the elevation of all live *C. californica* found within 1 m of the transect line. We find the *C. californica* live at 1 ± 0.3 m above NAVD88 (see Figure 11), which equates to mean sea level ± 0.3 m (Sadro et al., 2007).

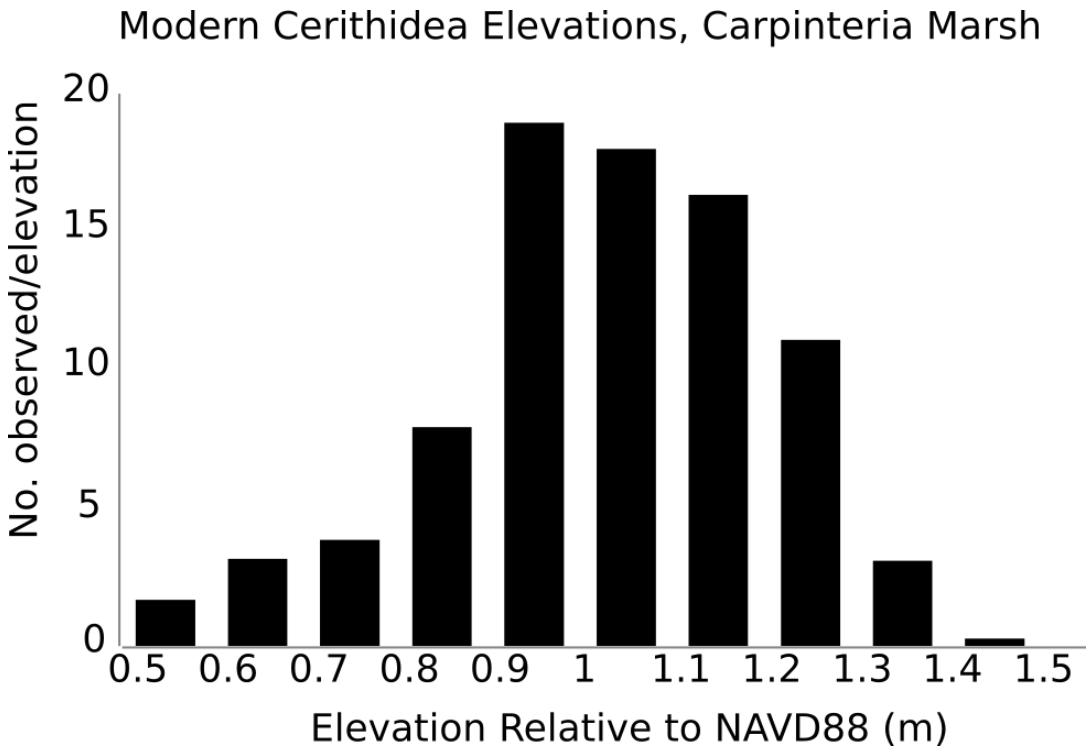


Figure 11. Histogram of C. californica elevations in Carpinteria Marsh.

4.4 Stratigraphic Evidence for Abrupt Environmental Change

At the base of all seven cores that penetrate below 10 m depth is a shell-rich gray sand, which grades upwards into 6-10 m of interbedded brown muds and sand containing intertidal gastropod shells (Figure 12). These organic-rich, fine-grained deposits are abruptly (<1 mm contact, as defined by Nelson et al., 1998) overlain by 1-4 m of medium-grained, shelly sand, similar to the basal layer. This upper gray sand grades into the top-most sediment in the marsh—organic-rich, laminated and bioturbated muds interbedded with brown sand layers. The sharp or erosional contact between the lower muds and upper sand occurs at an elevation of -1.93 to -3.28 m relative to North American Vertical Datum 1988 (NAVD88), and is the candidate subsidence surface (CSS, Figure 12).

The CSS marks a distinct lithostratigraphic, geochemical, and biological boundary (Figure 13). The silty mud below the contact is brown, organic-rich, and laminated or massive. The grain size, color, and sedimentary structures within the lower muds are similar to those observed in the upper meter of historical to modern marsh deposits, formed dominantly above Mean Sea Level (MSL) today (Sadro et al., 2007). When foraminifera are present below the CSS, assemblages are dominated by the low marsh species *Miliammina fusca* with rare *Trochammina inflata* and *Elphidium excavatum* (Avnaim-Katav et al., 2017; Bentz, 2016; Scott et al., 2011). Shells of *Cerithidea californica*, a marsh gastropod, were found embedded in the mud directly below the CSS in core CM46, and within muddy rip-up clasts just above the CSS in CM21.

Directly above the CSS, the grain size abruptly increases to fine to medium silty sand. This gray sand extends 2-3 meters up from the CSS before grading into the marsh surface deposits. The CSS contact is erosive and contains muddy rip-up clasts in four of

seven cores in which it is observed. The grey sand exhibits massive, bioturbated, and laminated sections, which are variable and difficult to correlate between cores. It contains sparse organics and shell fragments of intertidal to subtidal invertebrates including articulated *Chione undulata, Leukoma staminea, Tagelus californianus,* and *Macoma nasuta*. A fragment of *Leptopecten latiauratus*, a marine, non-estuarine kelp scallop, was also found within the sand. Similar to modern beach and dune sand in Carpinteria (Wilson et al., 2014), the gray sand is devoid of foraminifera and ostracods.

XRF and $\delta^{13}C$ data from CM46 also show an abrupt shift at the CSS (Figure 13). Although qualitative, relative changes in XRF values of various elements have been related to changes in the proportion of sedimentary material derived from marine versus terrestrial sources. Increases in Ca and Sr values have been associated with increased marine influence, while increases in Fe have been associated with increased terrestrial influence (Dupont and Kuhlmann, 2017; Kuwatani et al., 2014). The mud below CSS has low Sr and Ca, and high Fe values, but this pattern abruptly reverses in the grey sand above the CSS contact, suggesting the CSS marks a shift from more terrestrially influenced sediment to more marine influenced sediment. In addition, the bulk sediment $\delta^{13}C$ values of the 1 m of mud below the CSS in CM46 averages 25.3 ± 2.0‰, while $\delta^{13}C$ values of the 1 m of the gray sand above the CSS average 22.2 ± 3.4‰. Modern sediments in the marsh demonstrate a linear increase in $\delta^{13}C$ values with decreasing elevation. This trend has also been observed in other estuaries, and interpreted to represent increased marine carbon input at lower elevations (Milker et al., 2015).

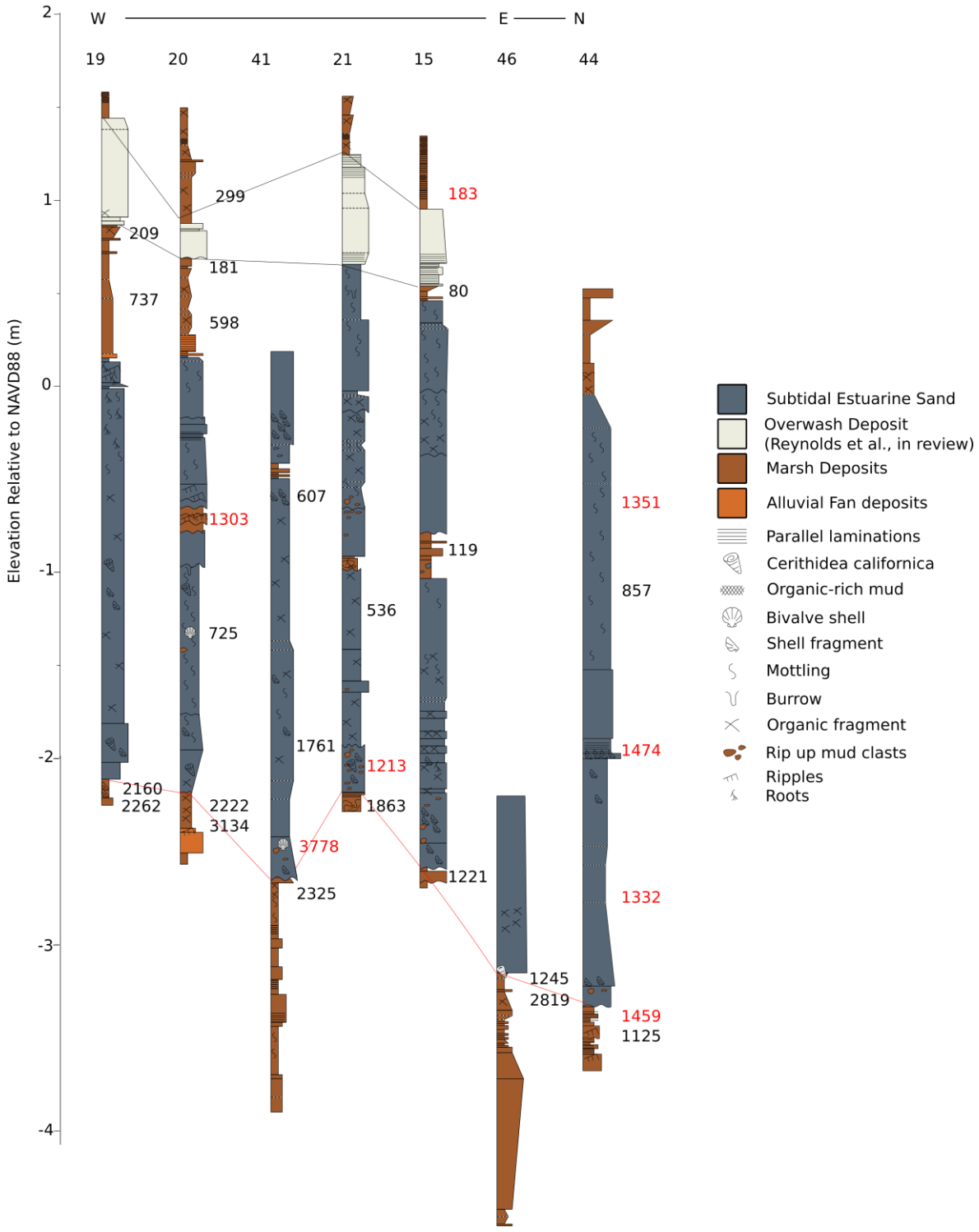


Figure 12. Transect A Core Stratigraphy. Transect through all cores that include the CSS (shown in red). Median calibrated ages are shown (see Appendix C and Figure 14 for 2 σ ages). Red ages are interpreted as reworked and are removed from the chronological model.

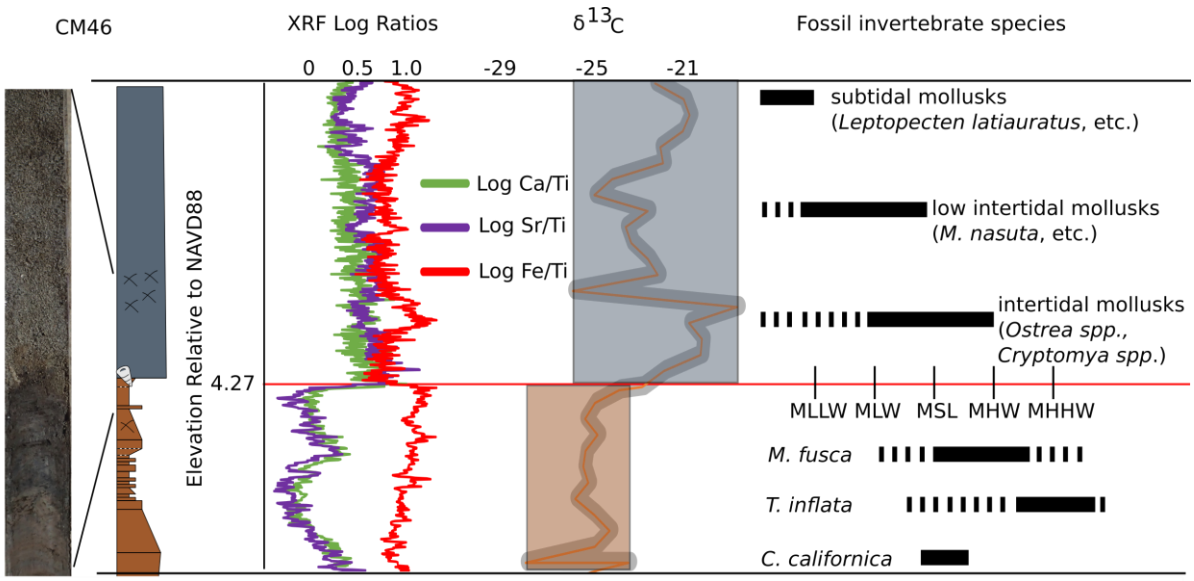


Figure 13. Evidence of RSL Change at the CSS. Core photo, stratigraphy, XRF, $\delta^{13}C$ data (with 2 sigma uncertainty envelope), and invertebrates found above and below the CSS (red line) with their approximate elevation ranges relative to tidal datums.

4.5 Chronology of the CSS

Radiocarbon ages show that sedimentation in Carpinteria Marsh from ~7 to 3 ka was ~2.2 mm a^{-1} (Figure 14). Sedimentation initially kept pace with RSL rise, but began to outpace RSL around 5 ka, at which point the marsh became overfilled. This lack of accommodation caused a ~2 kyr hiatus in sedimentation due to erosion and/or non-deposition between 2.8 ka and 1.0 ka. Dry climate conditions are documented from 2.8-1.85 ka in the southwest Great Basin Region (the Late Holocene Dry Period (Mensing et al., 2013)), from 2.1-0.7 ka at Dune Pond in Santa Barbara (Ejarque et al., 2015); and from 2.57 to 2.0 ka in Zaca Lake, Santa Maria (Kirby et al., 2014), indicating regionally dry climatic conditions may have exacerbated this period of erosion/non-deposition in Carpinteria Marsh.

The CSS must have formed after deposition of the mud beneath it, but before deposition of the sand above it. Using only the cores dated both above and below the CSS (Figure 14), and using only dates in stratigraphic order within each core (Appendix C, Supplementary Data), the 50 cm of mud beneath the CSS was deposited between 1 and 3 ka, while the sand above the CSS was deposited after 1 ka. Therefore, the CSS formed at ~1 ka. An age uncertainty of 0.1 ka was assigned to the CSS because the age range 0.9-1.1 ka overlaps the three youngest age ranges above and below the CSS.

After 1.0 ka the sedimentary history between cores becomes more variable. Many of the ages in the sand above the CSS are out of stratigraphic order within their core, indicating reworking. Sedimentation above the CSS was rapid—with as much as 2 m of sediment accumulating within 500 years after the event (Figure 14b).

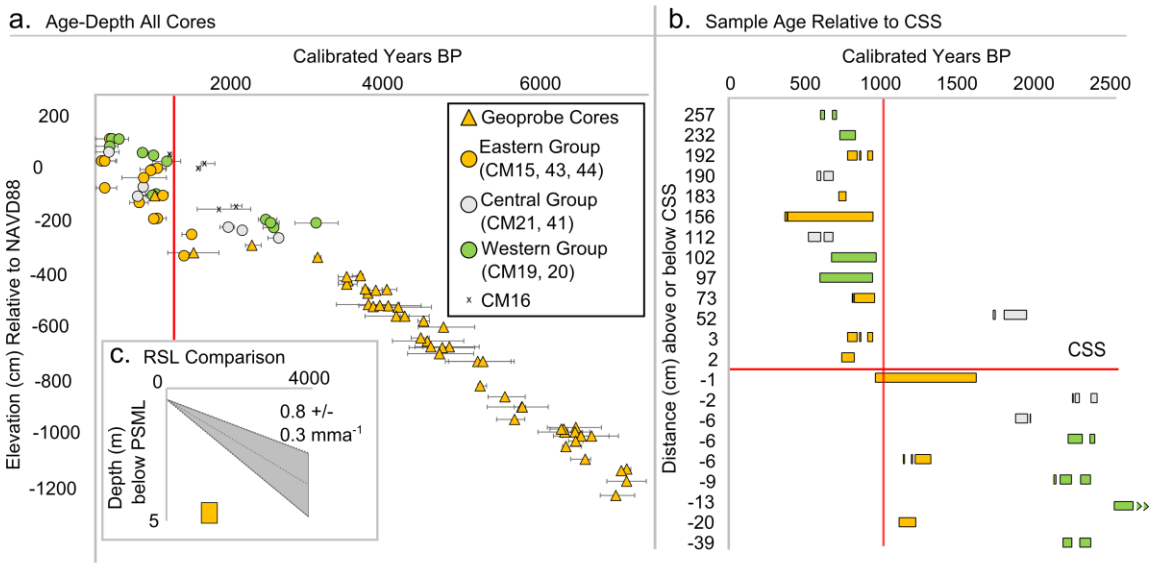


Figure 14. Chronology of the CSS. (a) shows 2 σ calibrated radiocarbon ages vs. elevation in all cores. Ages out of stratigraphic order within their core have been removed. (b) shows 2 σ calibrated ages of radiocarbon samples from cores in which the CSS contact is directly sampled. The depths above and below are in order, but not to scale. The vertical red line in both (a) and (b) represents the inferred timing of the CSS event. (c) Inset shows relative sea level of southern California (Reynolds and Simms, 2015) compared to the C. californica-derived RSL estimation for Carpinteria at the CSS. Cores are grouped according to location in the marsh: Eastern Group includes cores 19 and 20, Central Group includes cores 41 and 21, and Western Group includes cores 15, 44, 45, and 51.

4.6 Interpretation of the CSS

The lithology, fossil content, and geochemistry across the CSS indicate an abrupt increase in RSL in Carpinteria Marsh at 1.0 ± 0.1 ka. The mud below the contact contains marsh species, geochemical indications of terrestrial influence, a high-organic content, and grain size similar to that observed on the surface of the marsh today. The overlying gray sand contains subtidal shell species, geochemical indications of marine influence, and grain size and low-organic content typical of the mouth and subtidal channels within the marsh today.

The presence of rip-up clasts, erosional contacts, and rapid deposition above the candidate subsidence surface implies infilling of suddenly expanded accommodation. The CSS varies in elevation from -1.9 to -3.28 m, but is laterally continuous between cores as much as 700 meters apart from one another (Figure 9, 2). The chronology indicates this environmental change was abrupt and synchronous throughout the marsh, resulting in the formation of marine-influenced, subtidal estuary that lasted for at least 500 years.

Nonseismic alternatives to subsidence include storm or tsunami deposition, channel or estuarine mouth migration, climatic influence on sedimentation rates, or barrier breaching. The stratigraphy and chronology within the sand above the CSS suggests this sand was not emplaced during a single event, as would be expected for storm or tsunami deposition. No indicators of similar changes are found in other estuaries in the area (Cole and Wahl, 2000; Ejarque et al., 2015; Lohmar et al., 1980), as would be expected from a climatic event. The emplacement of the upper gray sand over mud appears to be synchronous throughout the marsh, which would argue against channel or mouth migration. Finally, barrier breaching would require that the mud below the CSS was deposited ~1-3 m below MSL to allow for infilling of accommodation, which is not likely given the geochemical data and presence of

the intertidal *C. californica*. Therefore, we argue that abrupt, tectonic subsidence at 1.0 ka is the most likely cause of the stratigraphic boundary marked by the CSS.

4.7 Magnitude of Subsidence

We followed the methodology of Simms et al. (2016) to calculate the magnitude of RSL increase at 1.0 ka based on the *C. californica* shell found just below the CSS in CM46. *C. californica* has been found to live 1.2-2.1 m above MLLW in other marshes in Southern California (Sousa, 1983), and -0.2 ± 0.3 m relative to present mean sea level (PMSL) in Carpinteria Marsh (Methods). Therefore the *C. californica* found in CM46 at -4.29 m represents a paleo-RSL of 4.27 ± 0.3 m below PMSL. In contrast, at 1.0 ka, average RSL in southern California was 0.8 ± 0.3 m below PMSL (Reynolds and Simms, 2015). Therefore, RSL in Carpinteria Marsh increased by 3.47 ± 0.5 m at 1 ka. Because no abrupt increases in RSL are expected for California in the late Holocene (Reeder-Myers et al., 2015; Reynolds and Simms, 2015), we interpret this RSL increase to represent subsidence of the marsh surface, and hereafter use the terms "RSL increase" and "subsidence" interchangeably.

A similar calculation can be made from the $\delta^{13}C$ data by comparing modern values and corresponding elevations to core data. The 1 m of mud below the candidate subsidence surface in CM46 has an average $\delta^{13}C$ value of -25‰. Modern bulk sediments with this value are found at elevations of 1.5 ± 0.3 m (0.48 ± 0.3 m above PMSL) today. Assuming this elevation range for the mud beneath the CSS in CM46, we calculate 3.97 ± 0.5 m of subsidence, agreeing, within error, to the subsidence estimated from *C. californica*-derived RSL estimates.

In regions underlain by deep deposits of unconsolidated sediment, such as Carpinteria basin, shaking-induced compaction is known to contribute to overestimates of

coseismic subsidence (Leonard et al., 2004). Additionally, the presence of rip-up clasts in four cores indicates some erosion of the marsh surface occurred post-subsidence. Therefore, we interpret the observed subsidence in CM46 to represent a maximum estimate of vertical motion, with probable contributions of liquefaction-induced compaction and erosion. The shallowest occurrence of the CSS is at -1.93 m elevation in CM19. The mud below the contact in this core is devoid of foraminifera or shells, so we cannot estimate the elevation at which it was deposited. Assuming it was deposited at the same elevation as CM46, however, leads to a minimum amount of subsidence in Carpinteria Marsh of 1.35 ± 0.5 m.

Variability in the elevation of the CSS between cores (Figure 12) may reflect uneven coseismic subsidence and/or differences in compaction, erosion, or original marsh topography. CM16 extends to 4 m below ground surface, but does not contain the gray sand present in other cores, likely demonstrating the landward limit of sand deposition. This core contains beds of laminated muds and brown sand—the latter of which is interpreted to represent alluvial fan deposits from paleo streams entering the fringes of the marsh. One sand bed, which dates to ~1 ka, has convolute bedding. We interpret this to have been caused by liquefaction due to the subsidence event at 1 ka. The lack of marine-influenced sand above this layer suggests either CM16 subsided less than other cores in the marsh, or was at a higher pre-subsidence elevation and remained above MSL after subsidence.

In other areas of southern California, groundwater withdrawal and oil extraction is thought to contribute to ongoing subsidence (Marshall et al., 2013). A maximum of 2 mm a^{-1} of anthropogenic subsidence since 1850 (Marshall et al., 2013) would account for less than 0.3 m of the subsidence observed in Carpinteria. Therefore, anthropogenic factors cannot explain the observed subsidence.

4.8 Hazard and Structural Implications

Previously calculated comparisons of deeper *C. californica*-derived paleo-RSL to the southern California RSL compilation(Reynolds and Simms, 2015) show calculated subsidence rates decrease with depth in Carpinteria, as the total magnitude of subsidence is averaged over a longer and longer period of time. This suggests that most, if not all, of the long-term subsidence calculated previously (Simms et al., 2016) may have been accomplished in the single 1.0 ka event.

The most likely source of subsidence within Carpinteria Slough is movement along the RCF, which would imply a hazard to the greater Carpinteria community, and possibly neighboring Santa Barbara, if the RCF and Mesa Fault are linked(Jackson and Yeats, 1982; Jennings and Saucedo, 1994). The potential effects of such a subsidence event, as documented from historical events, include coastal flooding, ecological community shifts, damage to infrastructure due to liquefaction, and increased susceptibility of low-lying coastal areas to storms and sea-level rise (Hughes et al., 2015; Imakiire and Koarai, 2012; Jaramillo et al., 2017). However, the linear sedimentation rate from 3-7 ka and absence of stratigraphic evidence for older subsidence events suggests that the recurrence interval for cosiesmic subsidence in Carpinteria is greater than 6 kyrs.

The Carpinteria 1.0 ± 0.1 ka subsidence event is contemporaneous with the most recent large earthquake at Pitas Point near Ventura, dated to 0.95 ka (Rockwell et al., 2016). Correlation between the two events would support the potential for large-scale ruptures within the Ventura/Santa Barbara regions. However, three older Holocene uplift events observed at Pitas Point have no correlative stratigraphic changes in Carpinteria, perhaps suggesting movement along the PPF only occasionally activates the RCF. Future research

should explore whether Quaternary motion inferred along the Rincon-Mesa faults (Fredrickson, 2016) is coincident with subsidence in Carpinteria.

This research clearly demonstrates that fault-bound estuaries in southern California are capable of experiencing coseismic subsidence. Therefore, subsidence in fault-bounded estuaries in southern California, and elsewhere along the Californian, Mediterranean, and other active coastlines should be considered a potential hazard and investigated to determine the existence and recurrence intervals of such events. This research also demonstrates that abrupt, coseismic subsidence on non-subducting active margins can be identified and quantified in the stratigraphic record with the same criteria used for subduction margins. However, an extensive suite of cores and multiple proxies are required to differentiate subsidence from other estuarine processes.

CHAPTER 5

5. A Holocene hydroclimate archive from Carpinteria Marsh, California

Winter storm activity and resulting precipitation patterns in coastal southern California are spatially and temporally variable. Periods of below average precipitation, such as the 2012-2016 California drought, have costly effects for agriculture and exacerbate wildfire risk. On the other extreme, coastal and inland flooding from winter storms (e.g., 1997-8, 2004-5) and debris flows triggered by intense spells of precipitation (e.g., La Conchita, 2005; Montecito, 2018) have been deadly. In coastal southern California, decadal to centennial scale hydroclimate variability is not well understood, and past hydroclimate reconstructions are sparse. Here we show a new record of paleoflood deposition from Carpinteria Marsh, California.

Streams in the Santa Barbara region only transport sediment during storm events; therefore, paleoflood deposits are a good proxy for storm activity throughout the Holocene. The timing of paleoflood events in Carpinteria is comparable to regional records of hydroclimate trends in the Holocene, demonstrating more frequent and thicker paleoflood deposition from 0.3-1 ka, 2.8-3.6 ka, 4-4.5 ka, and 5-5.3 ka. Paleoflood deposits are thinnest and the least frequent 1-2.8 ka, 4.5-5 ka, and 5.3-7 ka, perhaps indicating extended drought conditions during these times. Alluvial sediment in estuaries provides an additional hydroclimate record in Mediterranean climate regions where lake and tree ring records may be hard to come by.

5.1 Introduction

Most of the coastal zone in the western United States is classified as having a Mediterranean climate, characterized by warm, dry summers and cool, wet winters (Aschmann, 1973). In California, most of the annual precipitation occurs during the winter season (November-May) (Ryan et al.,1994) and most of the winter season precipitation occurs during a few individual precipitation events (storms) (Dettinger et al., 2011). Therefore, higher than average frequency or intensity of winter storms is associated with excess seasonal and annual precipitation totals, but also with increased occurrence of storm-induced natural hazards such as flooding, coastal erosion, landslides, and debris flows. Persistent winter seasons with fewer and/or weaker storms can lead to drought conditions, resulting in increased risk for wildfires (Westerling et al. 2006).

Understanding winter storm variability (location, intensity, duration, and frequency) is important for predicting water resource availability and the likelihood of natural hazard events. However, it has proved challenging to predict future storm activity and resulting precipitation patterns. Models of future precipitation yield inconsistent predictions for the Pacific coast (Dettinger et al., 2011) (Bell et al., 2004; Cai et al., 2014). Even short-term predictions can fail from one year to the next. For example, the 2015-2016 strong El Niño winter was predicted to result in increased precipitation in southern California, but instead this region was drier than average over the winter season (Jong et al., 2017).

Part of the challenge in pr**e**dicting precipitation patterns along the west coast arises from the complicated and interrelated intraseasonal (Madden-Julian Oscillation (MJO), Atmospheric Rivers (ARs)), interannual (El Niño Southern Oscillation (ENSO), North American Monsoon (NAM)), and decadal (Pacific Decadal Oscillation) ocean-atmospheric phenomena in this region. A great deal of uncertainty remains in how these different

processes affect precipitation frequency and magnitude and in how they may modulate or intensify one another. The temporal limitations of the instrumental record further hamper our understanding of storm variability. While instrumental records have been crucial for documenting recent climate change, especially anthropogenic influences on the climate system, they often miss environmental variation or catastrophic events that recur over decadal, millennial, or longer timescales.

The geological record of environmental change preserved in marine and terrestrial sediments (Ely, 1997; Enzel et al., 1993; Hendy et al., 2013; Hendy et al., 2015; Kirby et al., 2010; Kirby et al., 2014; Kirby et al., 2012; Schimmelmann et al., 2013; Schimmelmann et al., 2006), and speleothems (Wagner, 2006) extends our record of past climate conditions beyond the few hundred years of instrumental and historical climate data. Decadal to centennial patterns of precipitation are particularly poorly understood (Kirby et al., 2012), so pre-instrumental records of hydroclimate are crucial for understanding spatial and temporal variability, connections between different climate processes, and landscape responses at these timescales.

Existing Holocene hydroclimate records from southwestern North America are dominantly from lakes (Kirby et al., 2010; Kirby et al., 2014; Kirby et al., 2012), deserts (Ely, 1997; Enzel et al., 1993; Miller et al., 2010) and marine basins (Barron et al., 2015; Du et al., 2018; Hendy et al., 2013; Schimmelmann et al., 2013). Paleoclimate records from coastal southern California, a region lacking in lacustrine and tree ring records, are sparsely distributed. Estuarine paleoclimate records have helped fill in some of these geographical gaps. Extant estuarine records (Anderson et al., 2010; Beller, 2014; Cole and Liu, 1994; Cole and Wahl, 2000; Davis, 1992; Davis, 1996; Mudie and Byrne, 1980b; Scott et al., 2011) focus almost exclusively on paleoecological and anthropogenic changes through the

Holocene, enabling important reconstructions of centennial to millennial scale temperature and moisture trends in the region. However, additional insights about storm activity may be able to be gleaned from more detailed studies of estuarine stratigraphy and physical sedimentology.

In Mediterranean climates, ephemeral streams transport sediments to the coastal region only during or immediately following large precipitation events (storms) (Warrick and Mertes, 2009). Therefore, we hypothesize that fluvial-sourced paleoflood deposits in the estuarine record can serve as proxies for storm activity in the Holocene. We use diagnostic geochemical and grain size characteristics to differentiate marine derived sand beds from fluvially derived sand beds in Carpinteria Marsh, California. These fluvially-derived beds are interpreted to represent alluvial fans prograding into the marsh fringes during storm-induced flooding of the coastal plain of Carpinteria.

Our objectives are: (1) to identify evidence for storm-induced paleoflood deposition in the Holocene estuarine sedimentary record of Carpinteria Marsh, California; (2) to compare the timing of paleofloods in this estuary to the records of floods and pluvial periods from the Santa Barbara Channel and nearby lakes; and (3) to compare the timing of paleofloods in Carpinteria to other proxies for the climate patterns (ENSO, PDO, ARs) thought to drive precipitation variability in coastal southern California.

5.2 Study Site and Background

Carpinteria Marsh (34^{o} 24’ N 119^{o} 31’ 30” W) is a ~0.9 km^{2} salt marsh along the central Santa Barbara Channel. Carpinteria Marsh contains a ~7000 year, high resolution sedimentary record of environmental change (Simms et al., 2016; Chapter 3). The east-west trending Santa Barbara coastline is home to the Santa Ynez Mountains, one of the fastest

uplifting mountain ranges in the world (Rockwell et al., 2016; Gurrola et al., 2014). These mountains exert a significant orographic effect on moisture sources moving over the region. The Channel Islands border the Santa Barbara Channel to the south, providing a barrier between mainland Santa Barbara and the open Pacific Ocean. Deep water off the Santa Barbara Chanel are sourced from the North Pacific, and the coastal region is subject to seasonally variable upwelling of cold, deep, nutrient-rich water (Harms and Winant, 1998).

5.2.1 Seasonal and subseasonal climate

Most of the annual precipitation along the Santa Barbara coastline occurs from November to May (Ryan et al., 1994). Much of the seasonal variation in weather along the southern California is controlled by the position and strength of the North Pacific High (NPH), a region of high atmospheric pressure marking the boundary between the Ferrel and Hadley atmospheric cells (Cayan and Peterson, 1989). The NPH is strong and centered over southern California during Northern Hemisphere (NH) summer, creating an atmospheric ridge that blocks storms from passing through to the southern coast. In the winter, the NPH migrates south and is generally weaker, allowing storms to reach the coastline. The subtropical jet stream, a river of wind in the troposphere above the NPH, is more active in the NH winter, and aids in bringing moist air masses and storm systems toward the southern Californian coast (e.g. Schroeder et al., 2013).

Atmospheric Rivers (ARs) are common features of such mid latitude winter storms, increasingly recognized as the main source of extreme precipitation and flooding along the west coast of North America (Dettinger et al., 2011; Ralph and Dettinger, 2011; Ralph et al., 2006). ARs are narrow (<1000 km wide), long (>2000 km), zones of concentrated water vapor in the lower troposphere, similar to low, short-lived jets, that transport moisture from

the tropics to the mid latitudes around the world (Zhu and Newell, 1998; Dettinger et al., 2011; Ralph et al., 2006). In the Northern Hemisphere, cyclones are characterized by low pressure cores surrounded by a counter-clockwise flow of winds. ARs are generated off the southeast quadrant of these cyclones, traveling in front of the cold front, transporting warm, moist air north and east from the tropics to the California coast (Ralph et al., 2006; Dettinger et al., 2011). When an AR reaches the topography of the California coast, the tropical moisture is orographically released in intense precipitation events lasting hours to days. The amount and intensity of precipitation varies by latitude and weakens inland (Harris, 2013).

In southern California, ARs are responsible for up to 20-40% of annual rainfall (Dettinger et al., 2011; Rutz et al., 2014), 20-30% total precipitation in Santa Barbara county, and 10-26% of rainfall days (Harris, 2013). ARs, especially the subset of AR events called Pineapple Express, which transports moisture from Hawaii to the west coast, have been responsible for many of the highest intensity precipitation and flooding events in recent decades (Dettinger et al., 2011). Both frequency and strength of ARs vary interannually, but because they are defined and identified using satellite imaging, their long-term variability is not well understood, nor is their relationship to other climatic patterns (Harris, 2013; Harris and Carvalho, 2017).

5.2.2 Interannual and decadal climate

Seasonal (winter) precipitation totals, frequency of storm events, duration of storms, and precipitation intensity of storms all vary on interannual and decadal time scales due to changes in ocean-atmosphere circulation and convection patterns. The El Niño Southern Oscillation (ENSO) is one such ocean-atmosphere climate phenomena. ENSO has three main phases which vary every ~3-7 years: its warm phase, El Niño, is characterized by warm

Sea Surface Temperatures (SSTs) in the eastern tropical Pacific which causes the thermocline to flatten and shallow; its normal phase is characterized by a steeper thermocline and cooler SSTs; and its cold phase, La Niña, is characterized by strengthened normal conditions where the pacific warm pool increases in area and the thermocline steepens. Each phase can also vary by strength (weak, moderate, strong), as defined by magnitude of SST anomalies.

ENSO has global effects, but in California, El Niño conditions are associated with increased water vapor along the coast, especially in the southern part of the state due to a southward shift of the jet stream, which directs cyclones over this region. Although the warm phase of ENSO is more likely than neutral or cold phases to be associated with increased precipitation in California, less than 50% of El Niño winters resulted in greater than average precipitation in Santa Barbara over the last century (Naftlay, 1998). Warm phase ENSO conditions are also associated with higher than average SST within the Santa Barbara Channel (Friddell et al., 2003).

The Pacific Decadal Oscillation (PDO) is a climate pattern with SST and precipitation patterns similar to that of ENSO, but varying over decades instead of years. Similar to ENSO, a positive (warm) PDO is associated with higher than average SST within the SBC (Friddel et al., 2003), and a southern displacement of the jet stream resulting in increased precipitation frequency and magnitude in southwestern North America (Mantua and Hare, 2002).

In summary, winter storms in southern California occur more frequently during times of higher than average SST in the SBC, which occur during years experiencing the warm phase of ENSO and the positive (warm) phase of the PDO. Likewise, cooler than average SST are associated with La Niña conditions and an increased risk for drought (Barron et al.,

2015). From analysis of the last 40 years of precipitation data from Santa Barbara county, warm ENSO years are associated with wetter than average winters 73% of the time, and precipitation extremes occur more frequently during strongly cold and warm phases of ENSO than during moderate and weak conditions of any phase (Harris, 2013). Atmospheric River events in southern California may be more frequent and more intense during warm ENSOs and positive phases of the PDO (Harris, 2013), although the relationship between AR activity and other climate patterns is not well understood.

5.2.3 Landscape response to precipitation

Winter storms in southern California often result in river flooding, debris flows, and landslides. Few streams in southern California flow perennially—most are dominated by flashy, storm-driven flow (Warrick and Mertes, 2009). These streams transport sediment in short-lived braided rivers, sheet flow, and debris flows (Fenzel and Price, 1971). Some streams empty directly into the ocean—in these streams most of the transported sediment is deposited close to shore (Warrick et al., 2004), but some is transported far offshore by hyperpycnal and homopycnal plumes (Steel et al., 2016) and makes up ~85% of the SBB sediment budget (Schwalbach and Gorsline, 1985). Other streams terminate on the coastal plain as alluvial fans or fan deltas building into estuaries and coastal lagoons, which act as sediment traps.

The amount of sediment transported by a stream depends primarily on the flow conditions (discharge rate), sediment characteristics (grain size), substrate (lithology), and any preconditioning of the landscape (Reid and Laronne, 1995; Warrick and Mertes, 2009). Certain environmental preconditions can drastically influence sediment availability and sediment load during storm flow. Suspended sediment loads of coastal streams in southern

California were observed to increase by a factor of 35 in years following wildfires in the watershed (Warrick et al., 2012). Likewise, a storm during an otherwise dry period may be more likely to trigger debris flows and landslides due to increased sediment availability in the watershed. Earthquakes (e.g., Keefer et al., 1994), vegetation type and percent cover (e.g., Florhseim et al., 1991), and land-use change (Warrick and Mertes, 2009) can also play significant roles in sediment availability and erodibility within a watershed. Therefore, terrigenous sediment accumulation offshore and alluvial sedimentation in estuaries are both a result of storm-induced sediment transport, and so may record similar history of storm activity with local variability due to watershed characteristics.

5.3 Methods

Methods for core collection, stable isotope analysis, XRF analysis, and radiocarbon age constraints are described in full in Chapter 4. Additional methods are described below.

5.3.1 Grain size Analysis

CM46, CM51, and CM20 were sampled at 1 to 10 cm resolution (same sample depths as stable isotope samples) for grain size analysis. Sediments were pretreated for grain-size analysis with a 3-hour boil in 30% hydrogen peroxide to remove organic matter, and suspended in 10% hexametaphosphate (Kirby et al., 2014) before being analyzed on a CILAS 1190 laser diffraction grain size analyzer following the methods of Sperazza et al. (2004).

5.3.3 Calculations and Data Processing

For comparison with other proxy records, XRF data was averaged 2 cm above and below each grain size/stable isotope measurement. For calculations of Total Organic Carbon (TOC) and Total Nitrogen (TN) we used internal standards from the Atmospheric and Oceans Research Institute at the University of Tokyo, Japan to determine the relationship between injected C or N and machine measured value (equations 1 and 2 below). We calculated C and N amounts (μmol) in all the working standard samples analyzed by multiplying the sample weight (mg) by C and N contents of working standards (mmol C or N g–1). Regression lines through the measured peak area ("Area All") for C and N against the injected amount of C and N, gives the following equation:

[Area All]C = aC•[Injected C] + bC; [Area All]N = aN•[Injected N] + bN (Eq.1)

C and N amounts of the sample analyzed are calculated via the following equation:

[C (μmol)] = ([Area All]C – bC) / aC; [N (μmol)] = ([Area All]N – bN) / aN (Eq.2)

C and N contents (weight percent) of the sample is obtained by dividing these values by the weight of sample analyzed.

5.4 Results

5.4.1 Facies

The four facies and facies interpretations are described in detail in Chapter 3 (section 3.4.1) and Chapter 4 (section 4.4), and summarized in Table 6 below.

Table 6. Facies summary

Facies	Description	Interpretation	Occurrence
White Sand Facies	Fine to medium light grey sand. Fining upward silty laminations common. WSF beds have sharp or erosional bases and gradational upper contacts. No shell fragments. Rare organic fragments. Less negative δ13C values.	Beach sand overwashed into back-barrier marsh.	Only occurs once in upper meter of sediment; seaward cores only.
Grey Sand Facies	Fine to medium blue-gray sand. Beds of GSF have sharp or erosional bases and sharp or gradational upper contacts. Mottling, burrows, and discontinuous laminations common. Articulated bivalves, shell fragments common. Organic fragments small, but common. Less negative δ13C values and low C: N ratios. Larger values of Ca, Sr, Br.	Marine-influenced subtidal estuarine sand or estuarine mouth.	Occurs from ~0 to -3 m relative to NAVD88 throughout marsh.
Brown Sand Facies	Silt to coarse brown sand. Parallel laminations, climbing ripples, fining upward grain size common. Beds of BSF have sharp or erosional bases and sharp or gradational upper contacts. No shell fragments. Rare organic fragments. More negative δ13C values and high C:N ratios. Smaller values of Ca, Sr, and Br.	Fluvial flood deposit.	Occurs interbedded with MF throughout marsh. Thickest and more frequent beds of BSF are found in landward parts of marsh.
Mud Facies	Clay to silt. Parallel laminations and mottling common. Beds of MF have sharp or gradational bases and upper contacts. *Cerithidea californica* shells common, other shell fragments rare. Intermediate and variable δ13C, C:N, and XRF values.	Upper marsh deposits: vegetated marsh surface, mudflats, pans, upper channel banks.	Occurs in the upper 1-3 m of sediment in the marsh, as well as 2.5-10.5 m below NAVD88 throughout the marsh.

5.4.2 Stratigraphy of CM46

As previously shown in Figure 14 of Chapter 4, the overall pattern of sedimentation in Carpinteria Marsh can be summarized as (1) a basal bed of GSF below -10.5m NAVD88, (2) 5-8 m of interbedded BSF and MF beds, (3) another 1-3 m section of GSF, and finally, (4) the upper 1-3 meters of interbedded BSF, MF, and one bed of WSF. Here we present select data for CM46 . CM51 has similar grain size trends and is stratigraphically correlative (Figure 19).

Beds of BSF exhibiting the following properties were identified as candidate paleoflood deposits: (1) a sharp or erosional base, (2) an abrupt increase in grain size to at least fine sand from the layer below (3) a low $\delta^{13}C$ value relative to the layer below; 4) a high C:N ratio relative to the layer below; and (5) a high lithic content and absence of shell material. In some cases where isotopic data was not available, we used only criteria #1, 2, and 5 to identify paleoflood deposits.

Paleoflood deposits are interbedded with relatively more marine-influenced sediments of GSF or MF. These sediments, relative to paleoflood deposits, have higher $\delta^{13}C$ values, lower C:N ratios, and vary in grain size from clay to fine sand. The deposits of MF are often rich in *Cerithidea californica* shells and exhibit dense mottling. In GSF, *C. californica* shells are rare or absent, but other subtidal bivalves including *Chione undulata, Leukoma staminea, Tagelus californianus*, and *Macoma nasuta*, support the interpretation of a more marine-influenced, high energy environment present during deposition of this facies.

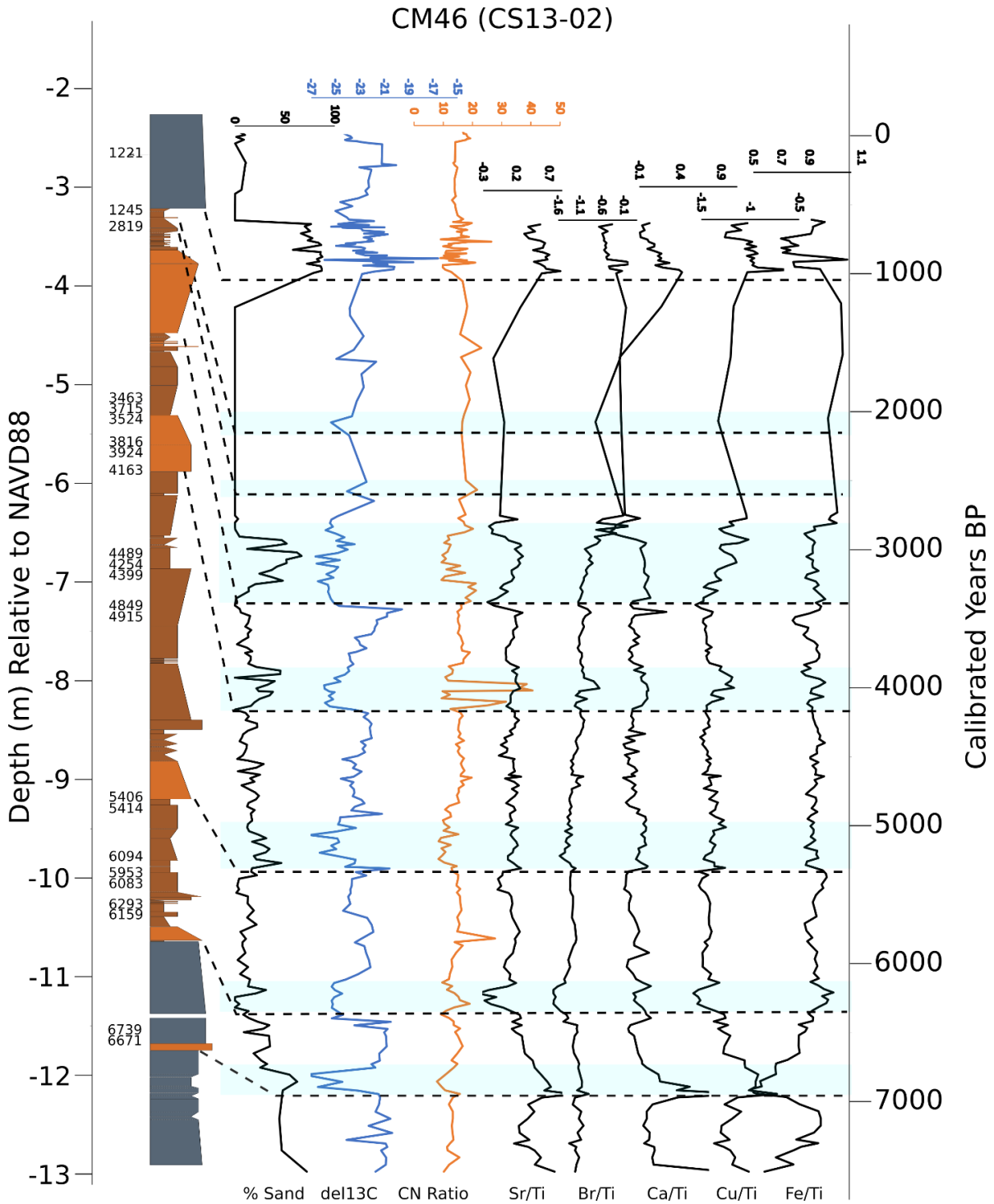


Figure 15. Compilation of grain size, stable isotope data for CM46 and CM20 and XRF data for CM46. Green bars highlight data associated with beds of BSF interpreted to represent paleofloods, aka alluvial fan deposits prograding into the marsh during storm flow of ephemeral streams.

5.4.3 Chronology

We combined radiocarbon data from each Geoprobe core and its nearest vibracores to get a full (ground surface to ~14m depth) sedimentary record at two locations in the marsh—one close to the shoreline, and close to the marsh's current most landward extent. Cores CM15 and 46 were combined for one age model, and CM43, 44, and 51 were combined for the second age model. An independent age model for CM16, which supplements the upper two meters of sediment not sampled in CM51, 43, or 44. We used BChron (Parnell et al., 2008), a Bayesian modeling program, to develop the age models and to predict the 2-sigma age for the base of each candidate paleoflood (BSF) deposit. BChron calibrates radiocarbon ages with IntCal13 (Reimer et al., 2013) and uses Monte Carlo methods to estimate errors on predicted ages. We calculated ages for the base of the deposit because the top of the deposits is sometimes gradational (deposit thicknesses are minimum). Because of the possibility of erosion, the ages given are maximum ages. Modeled age, 2-sigma uncertainties, and thickness of paleoflood deposits are given in Table 7.

Each group of cores (the landward group of CM51, 43, 44, and 16 and the seaward group CM15, 46) samples the full stratigraphy at that particular location. In order to prevent sampling bias, we only used vibracore data in sampling gaps of the Geoprobe cores, i.e. from 2 to 4 m below NAVD88 where we are missing a section of CM51 (Figure 19). We identified 41 total paleoflood deposits in the two combination records, 4 (8 total) of which are found in both records (~3.2 ka, 4 ka, 5.2 ka, and 6.3 ka). Other paleoflood beds may also be correlative, but because of the age uncertainties it is often difficult to confidently correlate individual beds. Because we only identified beds with average grain size coarser than fine

sand as paleoflood deposits, this number is likely a minimum. Smaller floods that transported finer grained material or muddy debris flows would be difficult to differentiate from other fine-grained deposits in the marsh. Additionally, erosion and resuspension of material may have destroyed some of the thinner paleoflood deposits, especially in the seaward portion of the marsh where tidal energy is the highest.

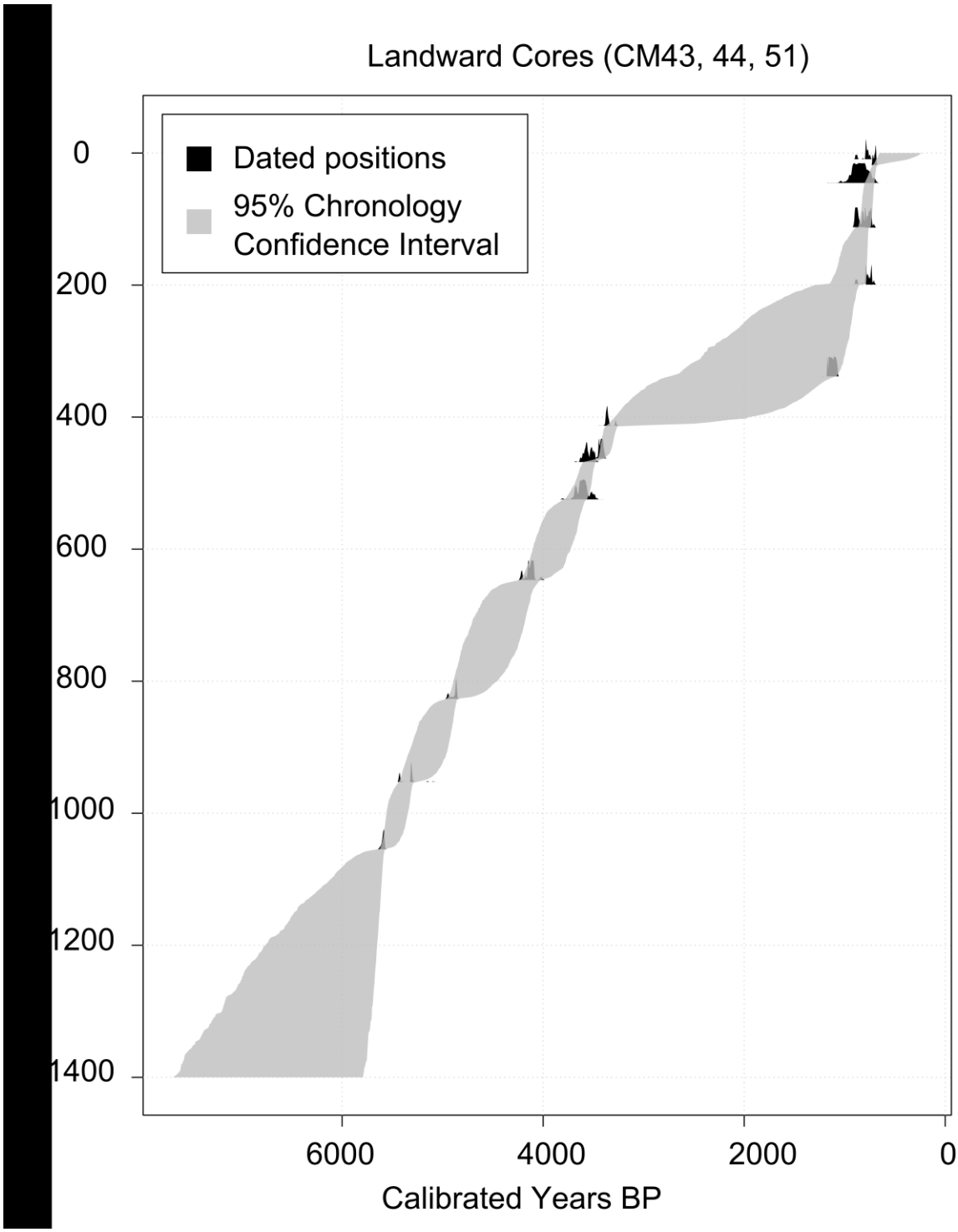


Figure 16 BChron age-depth model for the landward suite of cores.

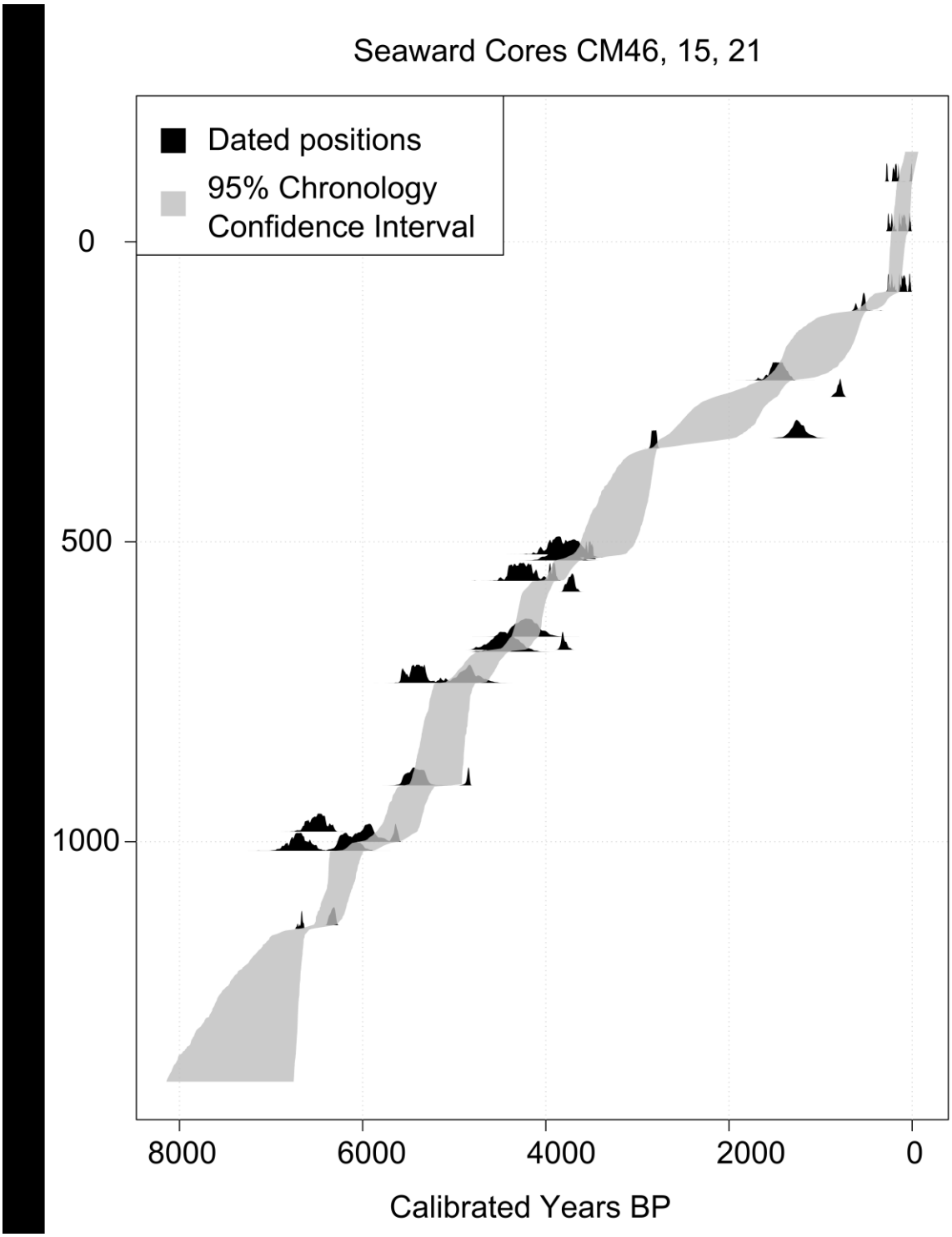


Figure 17. BChron age-depth model for the seaward suite of cores.

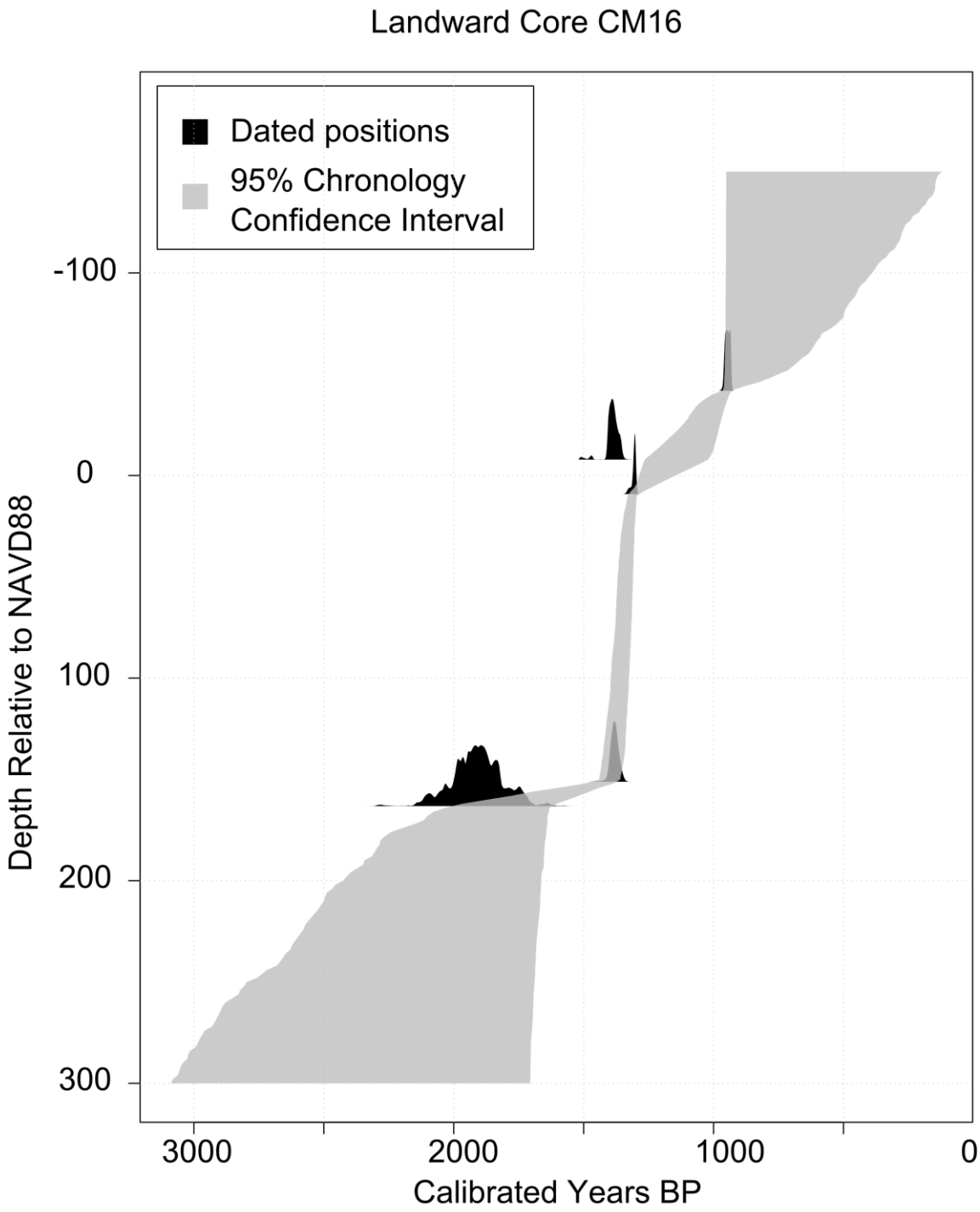


Figure 18. BChron generated age models for CM16.

Table 7. Table of paleoflood depths, thickness, and ages.

Core	Top Depth BGS	Base Depth BGS	Top Depth Below NAVD	Base Depth Below NAVD	Deposit Thickness	Median Calibrated Age BP	2-Sigma Uncertainty
CM15	85	86	-56	-55	1	62	84
CM15	216	217	75	76	1	228	76
CM43 16-02	12	30	-64	-46	18	392	306
CM43 16-02	65	80	-11	4	15	550	194
GP7	274	300	24	50	26	745	53
GP7	300	303	50	53	3	748	53
GP7	303	309	53	59	6	750	54
CM43 16-02	146	150	70	74	4	758	56
GP7	339	348	89	98	9	768	63
GP7	371	376	121	126	5	828	105
GP7	610	617	360	367	7	2000	953
GP2	562	563	338	339	1	2714	169
GP2	567	572	343	348	5	2837	113
GP2	602	660	378	436	58	3127	290
GP7	675	681	425	431	6	3372	107
GP7	681	686	431	436	5	3379	87
GP7	696	707	446	457	11	3411	48
GP7	707	711	457	461	4	3421	42
GP7	727	734	477	484	7	3569	79
GP7	843	873	593	623	30	4030	175
GP2	792	807	568	583	15	4094	148
GP7	935	943	685	693	8	4333	259
GP7	944	954	694	704	10	4398	290
GP7	954	961	704	711	7	4413	276
GP7	961	967	711	717	6	4432	284
GP7	1116	1122	866	872	6	5052	175
GP7	1122	1125	872	875	3	5058	182
GP7	1128	1170	878	920	42	5206	173
GP2	1064	1077	840	853	13	5222	257
GP7	1170	1200	920	950	30	5303	128
GP2	1239	1244	1015	1020	5	6134	214
GP2	1274	1298	1050	1074	24	6235	168
GP7	1525	1530	1275	1280	5	6356	800
GP2	1399	1404	1175	1180	5	6764	255

Table 7 (cont.). Table of paleoflood depths, thickness, and ages.

Core	Top Depth BGS	Base Depth BGS	Top Depth Below NAVD	Base Depth Below NAVD	Deposit Thickness	Median Calibrated Age BP	2-Sigma Uncertainty
CM16	15	17	-144	-142	2	836	440
CM16	58	84	-101	-75	26	905	271
CM16	85	94	-74	-65	9	916	249
CM16	94	101	-65	-58	7	925	222
CM16	216	220	57	61	4	1335	33
CM16	220	228	61	69	8	1340	32
CM16	229	255	70	96	26	1357	34

5.4.4 Stratigraphic Correlation

Using lithological and chronological constraints, we use three cores to build a north-south (shore perpendicular) cross section through the center of the marsh (Figure 19). Geoprobe cores did not sample the top ~3 meters of sediment, so we supplement the upper part of the record with vibracores CM20, CM3, and CM44, respectively. Cores exhibit similar vertical grain size trends and chronology. BSF beds tend to be thicker and more frequent in the landward part of the marsh, thinning and fining seaward.

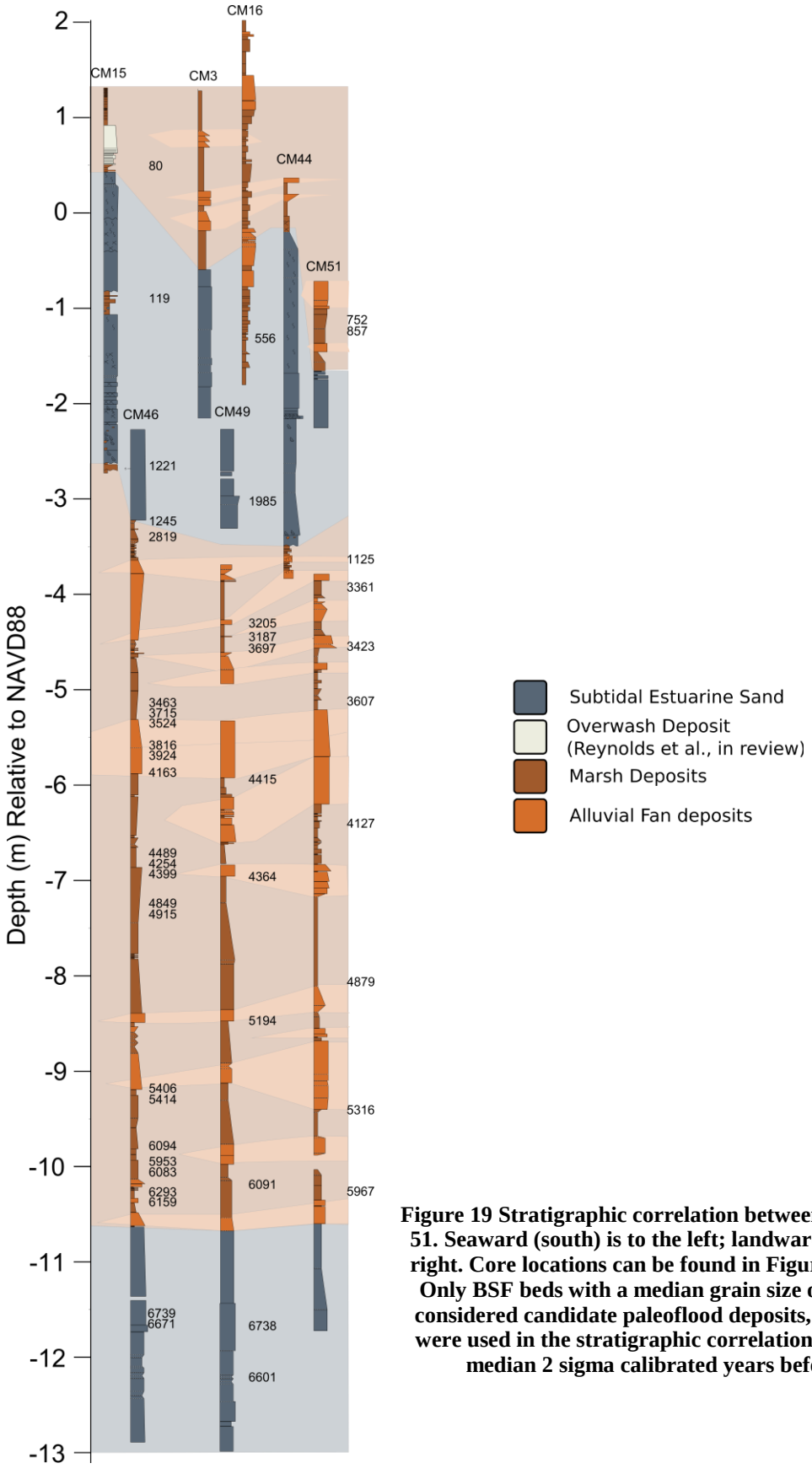


Figure 19 Stratigraphic correlation between cores 46, 49, and 51. Seaward (south) is to the left; landward (north) is to the right. Core locations can be found in Figure 9 of Chapter 4. Only BSF beds with a median grain size of fine sand were considered candidate paleoflood deposits, but all BSF beds were used in the stratigraphic correlation. Ages shown are median 2 sigma calibrated years before present.

5.5 Discussion

5.5.1 Characteristic and occurrence of paleoflood deposits in Carpinteria Marsh

These physical and geochemical characteristics of the paleoflood deposits indicate rapid deposition and transport of terrestrial (fluvial) organic and inorganic matter into the marsh via one of the ~4 streams that prehistorically entered the marsh (Ferren, 1985). Each paleoflood deposit may represent single events, or amalgamation of flooding from multiple storms during a period of months to tens of years.

Identified paleoflood deposits make up 12-25 % of the vertical accumulation of sediment in the three cores presented here. Salt marsh accretion tends to accelerate in parallel with sea level rise, allowing the marshes to effectively keep pace with moderate rates of sea level rise (Kirwan et al., 2016, 2017). However, these observations only hold true for estuarine systems with uninterrupted sediment supply. For most of its history, Carpinteria Marsh seems to have been able to keep pace with Holocene sea level rise via episodic input of alluvial sediments. However, modern and historical development, channelization, and debris basins installation within the watersheds of the streams which drain into Carpinteria Marsh now interrupt the flow of fluvial sediment into the marsh. Without this supply of sediment, accretion may no longer be able to keep pace with accelerating sea level rise.

Anthropogenic infrastructure not only decreases the total amount of alluvial sediment entering the marsh, but it also changes the grain size distribution within the marsh, selectively removing coarser grained material. Sandy substrates support rare species (Ferren 1985)—the lack of sand transport into the marsh, due to coastal armoring and the limits on terrestrial sediment transport may negatively affect these sensitive species in the future.

5.5.2 Comparisons to other records

5.5.2.1 Paleoflood chronology: comparison to the Santa Barbara Channel record

The Santa Barbara Basin (SBB) sedimentary record contains an approximately annual record of Holocene climate including flood deposition (Du et al., 2018; Schimmelman et al., 2006; Hendy et al., 2013; Hendy et al., 2015) and SST variations (Kennett and Kennett, 2007) in the Santa Barbara Channel. Sediment cores from ODP core site 893 in the Santa Barbara Channel contain grey terrigenous layers interpreted as sediment deposited via hyperpycnal flows during river floods from the coast (Du et al., 2018; Warrick et al., 2007; Schimmelman et al., 2006). 75 flood layers were deposited over the course of the 9000-year record (Du et al., 2018). The most recent of these flood layers dates to the 1861-2 AD winter storm season (Hendy et al., 2013).

These deposits are interpreted to represent large discharge events from streams along the Santa Barbara Channel. It is likely that other streams along the Santa Barbara Channel, such as those in the Carpinteria watershed, would initiate sediment transport during the same events. However, individual flood events are difficult to correlate between the SBB record and the Carpinteria Marsh record due to chronological uncertainties in the latter. Instead, following Du et al., 2018, we used a 100-year sliding window average of the paleoflood data to compare to the SBB record to the Carpinteria record (Figure 20). We use the paleoflood data from all non-overlapping cores in each of the two (seaward and landward) locations to calculate both flood frequency and magnitude of paleoflood sediment accumulation every 50 years, for each 100-year interval (i.e. frequency at 100 cal BP represents the number of

paleoflood deposits from 100-200 cal BP; and frequency at 150 cal BP represents the number of paleoflood deposits from 150-250 cal BP).

SBB floods are more frequent than those in Carpinteria—over the last 7 ka, the SBB has 55 flood deposits, while Carpinteria has 37 (41 minus the 4 which appear to be correlative). This discrepancy is likely due to the high potential for erosion and resuspension in a tidal environment, the amalgamation of flood beds deposited close in time, and variable spatial deposition in an estuary. Some combination of amalgamation and age uncertainty is the most likely culprit, since most of the "missing" SBB floods occur within error of a Carpinteria flood.

The timing and patterns of accumulation of flood deposits in Carpinteria is broadly consistent with the SBB record (Figure 20), with similar peaks and troughs of flood sediment accumulation. The similarities of the flood sediment accumulation histories also would suggest that some of the paleoflood deposits in Carpinteria are, in fact, representative of multiple episodes of flooding. However, the lack of floods during 1-2.8 ka in the Carpinteria record does not appear to be the result of amalgamation. Radiocarbon ages show a distinct plateau from during this time. This represents an abrupt decrease in sedimentation rate, hiatus, or period of erosion throughout much of the marsh. The condensed section represented by this time has higher than average $\delta^{13}C$ and C:N ratios, suggesting increased terrestrial relative to marine influence, perhaps due to marsh overfilling of available accommodation. CM44 sediments that date to this period are very dense, and contain evidence for desiccation and erosion. Sediments dated to this time in CM46 contain marsh foraminifera and a *C. californica* shell. The first half of this interval is contemporaneous with the Late Holocene Dry Period (LHDP) of Mensing et al., 2013, which was a time of aridity throughout the Great Basin and American southwest.

Only the Carpinteria floods from 0.8-0.9 ka do not have equivalents in the SBB record. These sediments were deposited following the ~1 ka subsidence event (Chapter 3). This may indicate that the magnitude of these paleoflood deposits is not related to an especially large storm, but instead to increased accommodation space following the subsidence event and increased sediment supply generated by the seismic disruption of the landscape. Precipitation events too small to leave a record in the SBB may have been able to transport sediment into Carpinteria Marsh because of these local factors.

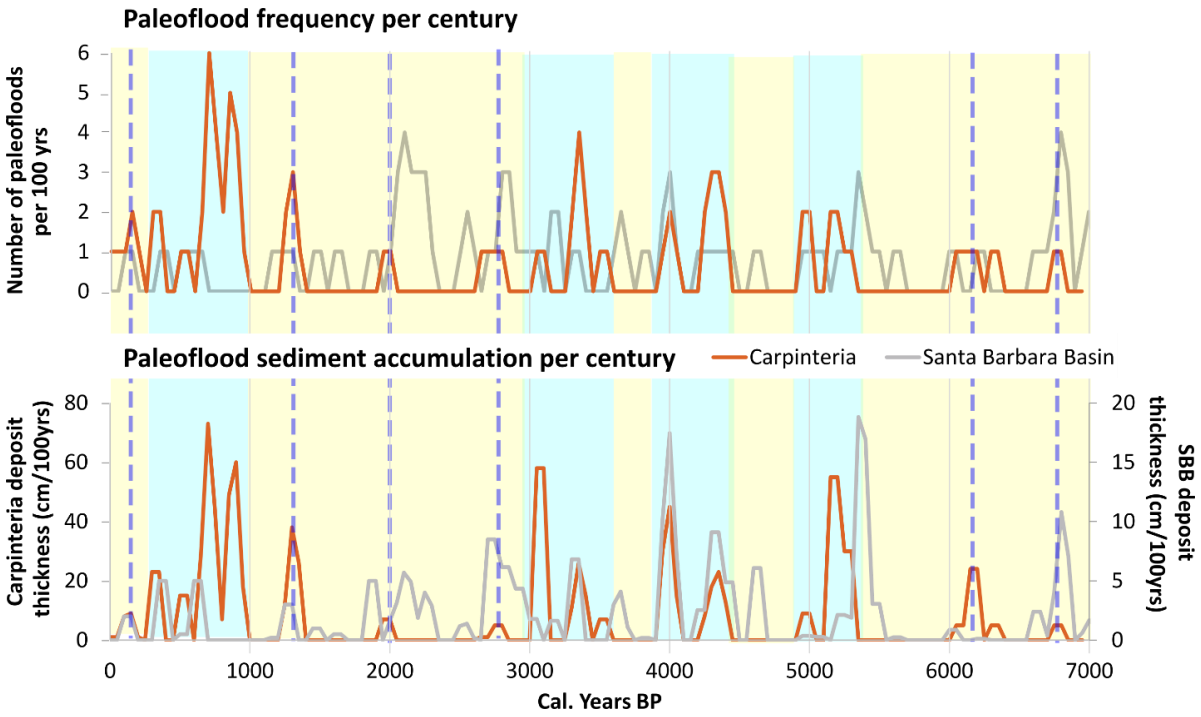


Figure 20. Carpinteria and Santa Barbara Basin (Du et al., 2018) paleoflood frequency and magnitude (bed thickness) per 100 year sliding window over the last 7000 years.

5.5.2.2 Pluvial periods

Other records of past hydroclimate from southwest North America show spatial and temporal variations comparable to what has been observed with modern climate in the region. However, some broadly consistent patterns environmental change have been inferred throughout the Holocene. Proxies for runoff and water levels from lacustrine records in southern California (Hiner et al., 2016; Kirby et al., 2010; Kirby et al., 2014; Kirby et al., 2012) and lake level records from the Mojave Desert (Enzel et al, 1992; Ely, 1997; Miller et al., 2010) indicate multiple decadal to centennial pluvial periods of wetter than average climate in southwestern North America at ~0.4-0.8, 3-5.5, and 6.6-7.3 ka. These pluvial periods have been ascribed to more frequent and higher magnitude winter storms (Kirby et al., 2012).

We identify four wet climate episodes (WE) in the Carpinteria record, corresponding to times of the greatest flood sediment accumulation and most frequent floods (light blue bars in Figure 20): 0.3-1 ka (WE1), 2.8-3.6 ka (WE2), 4-4.5 ka (WE3), and 4.9-5.3 ka (WE4). We also identify six additional smaller, possible wet episodes at ~0.2, 1.3, 2, 2.7, 6.3, and 6.7 ka. Carpinteria WE1 and WE2 are contemporaneous with pluvial periods identified in other sedimentological hydroclimate studies at Lower Bear Lake and Lake Elsinore (Kirby et al., 2010, Kirby et al., 2012), as well as high lake stands at Tulare Lake in the Sierra Nevada (Negrini et al., 2006). Both WE1 and WE2 are also contemporaneous with the Mojave desert's Silver Lake Playa highstands, dated to ~3.6 and 0.4 ka (Enzel, 1992). These two pluvials have been interpreted to represent increased frequency of winter storms in southwest North America (Ely et al., 1997; Enzel, 1992; Kirby et al., 2010). During the first half of WE1 (0.5-1 ka) and during all of WE2, SST in the Santa Barbara Channel were

cooler than average (Kennett and Kennett, 2007), which suggests a negative PDO or La Niña like conditions not normally associated in an increased frequency of winter storms. It is possible that non-El Niño AR storm activity increased instead (Kirby et al., 2010), although what would drive this is unclear. During the latter half of WE1 (0.3-0.5 ka), during the Little Ice Age, SBB pollen records documenting an increase in mesic species, interpreted to be related to more frequent El Niño like conditions (Heusser et al., 2015).



Figure 21. Location map for other sites referenced for pluvial proxies.

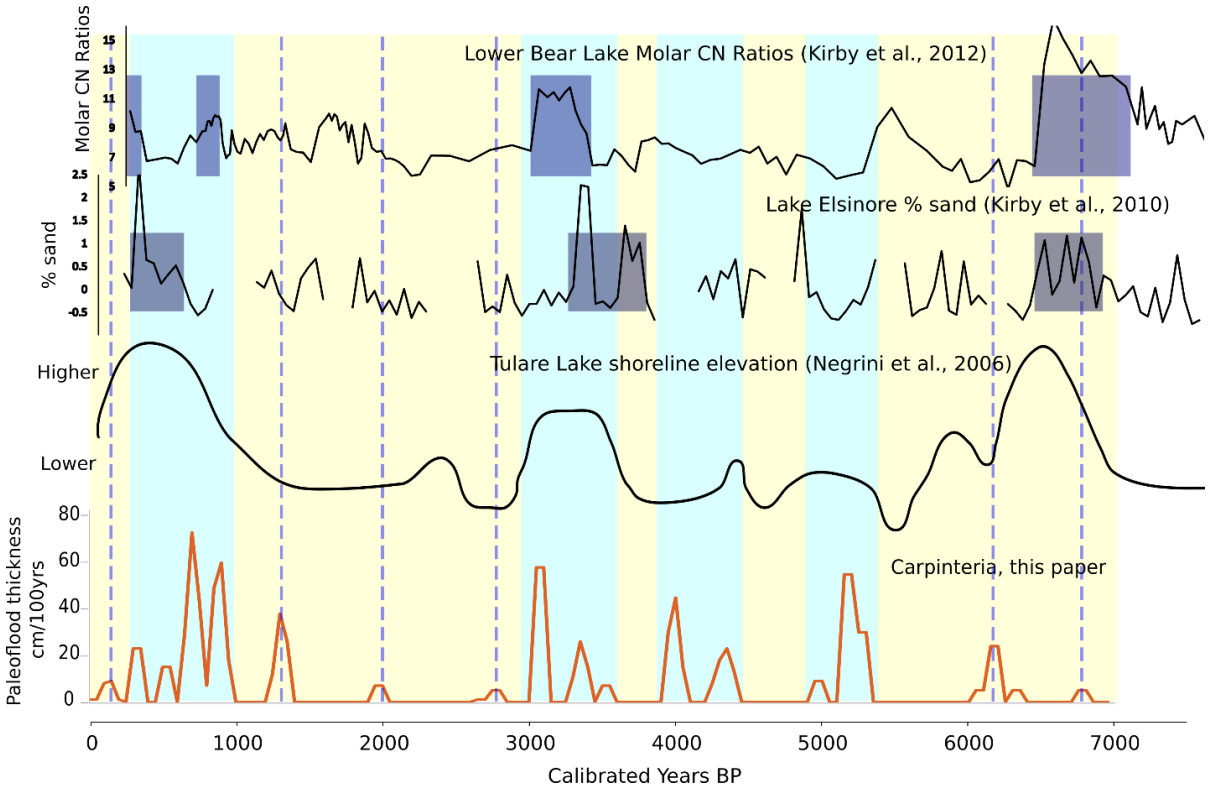


Figure 22. Comparison of Carpinteria paleoflood sediment accumulation and associated pluvial periods to other sedimentological based records of pluvials and high lake stands from California. Dark blue boxes indicate pluvial events defined by authors in referenced studies.

5.5.2.3 Comparisons to climate proxies

A comparison between the timing of increased flood sediment accumulation in the Carpinteria record with proxies for the main climate patterns thought to drive precipitation in southern California, PDO and ENSO, appears to show little clear correlation (Fig. 21). The late Holocene paleofloods in Carpinteria seem to correspond to increased episodes of El-Niño like conditions, but with the age uncertainties in the flood record, it is difficult to be confident about any relationship. It is possible that the flood events recorded in Carpinteria are not related to any one particular climate state (i.e. positive PDO, warm ENSO), but instead represent large AR storms which can occur in any phase.

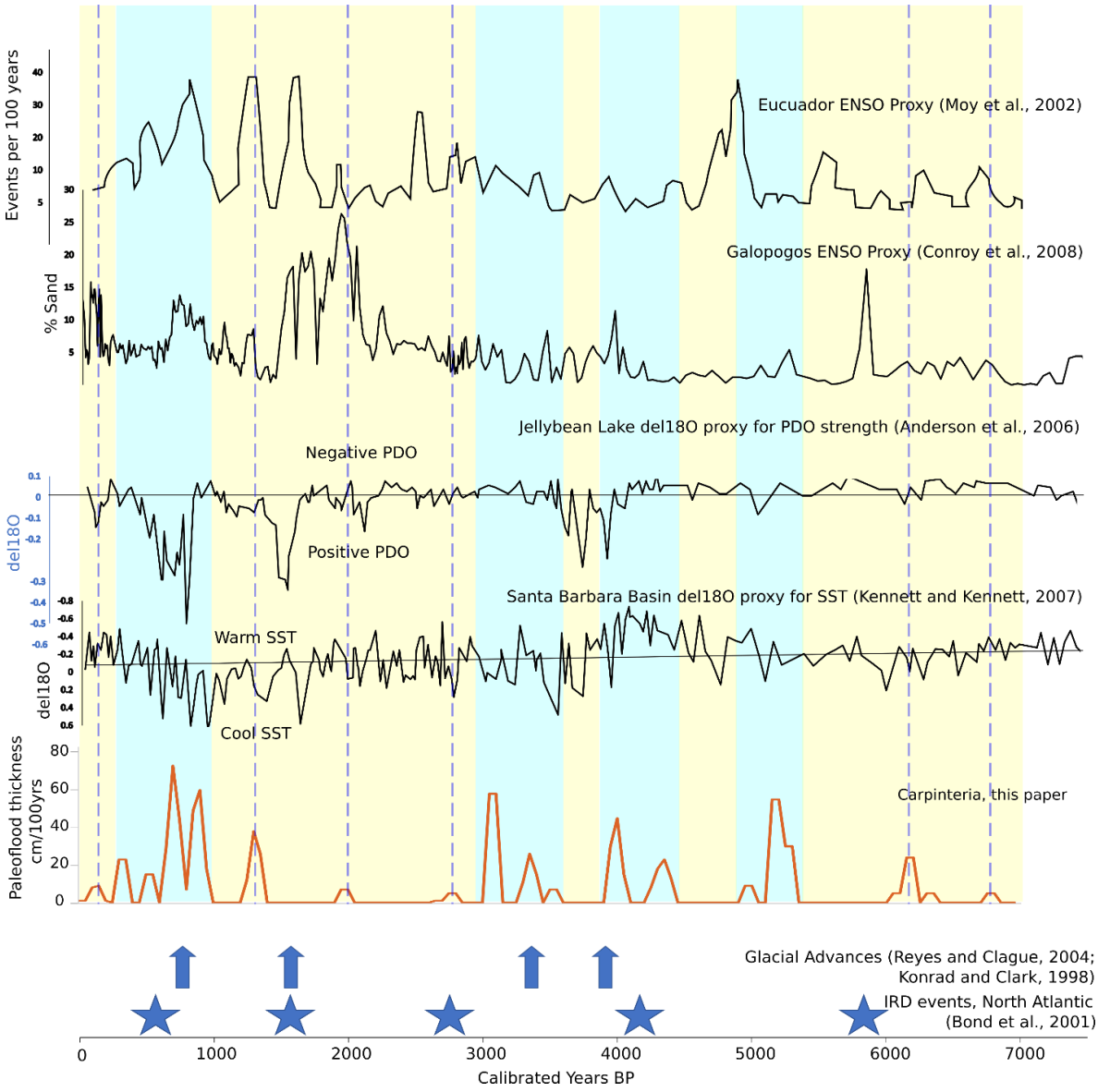


Figure 23. Comparison of Carpinteria pluvial (blue) and dry (yellow) periods to climate patterns thought to affect precipitation patterns and flooding in southern California. There appears to be little clear correspondence between flood frequency and magnitude (as represented by sediment accumulation) and proxies for ENSO (Moy et al., 2002, Conroy et al., 2008) , PDO (Anderson et al., 2005) , other climate proxies (Reyes and Clague, 2004; Konrad and Clark, 1998; Bond et al., 2001) or SBB SST (Kennett et al., 2007).

5.5.2.4 Long-lasting droughts

Tree ring (Cook et al., 2004), lacustrine (e.g., Benson et al 2002, Stine, 1994), and pollen (Mensing et al., 2013) records from the southwestern United States and Great Basin region indicate centennial to millennial scale droughts occurred during the Middle Holocene Dry Period (MHDP) from 7.5-5 ka (Lindstrom, 1990; Grayson, 2000; Benson et al., 2002); the Late Holocene Dry Period (LHDP), from ~2.8-1.8 ka (Mensing et al., 2013); and the Medieval Climate Anomaly (MCA) (Stine, 1994; Kleppe et al., 2011), from ~1.2-.75 ka. Floods in Carpinteria were small and infrequent from 1-2.8 ka, corresponds to the MHDP and the MCA, and from 5.3-7 ka, corresponding to the MHDP, indicating coastal southern California may also have been affected by these regional dry conditions.

The cause for drought conditions during these times is not well understood, although it has been proposed that they resulted from a long-lasting high-pressure ridge over the western United States (Stine, 1994) and a northward shift of the NPH, resulting in decreased SST off the west coast of North America. SST records from the Santa Barbara Channel indicate cool or neutral temperatures from ~0.5-3.8 ka and 5.9-6.2 ka, possibly representing persistent La Niña like conditions which would be expected to correspond with a drier climate in coastal southern California (Kennett and Kennett, 2007). Pollen, microfossil, and archeological evidence also supports less precipitation in coastal southern California during the MCA (Barron et al., 2015; Boxt et al., 1999; Heusser et al., 2015).

5.6 Conclusions

The stratigraphic record from Carpinteria Marsh provides a new Holocene hydroclimate record for the coastal southwest, a region lacking in such records. Estuarine sediments started to accumulate in Carpinteria at ~6-6.5 ka, a common transition period in climate records throughout the southwest United States and in coastal locations around the world (Chapter 2). From ~6.5 to 2.5 ka sedimentation in Carpinteria Marsh kept pace with sea-level rise and subsidence. The presence of *C. californica* throughout this time period suggest the marsh maintained a roughly constant elevation and tidal influence. Immediately after the 1 ka subsidence and inundation event (see Chapter 3), sedimentation increased until the marsh reestablished a high marsh environment between 500 and 100 years ago depending on the location within the marsh. Up to 25 % of the sediments within the marsh are of fluvial origin, indicating the interruption of sediments by the various flood management infrastructure in Carpinteria may inhibit the ability of the marsh to keep pace with future sea-level rise.

In Mediterranean climate estuaries, past flood deposits can be recognized by the abrupt increase in grain size and concurrent increase in geochemical markers of terrestrial organic input, indicative of sediment transport from steep mountain streams to alluvial fans on the coastal plain. Unlike in lake sediments, grain size alone cannot be used as a proxy for floods as increased marine influence can also drive increases in the sand fraction. Therefore, multiple lines of evidence are needed to ascribe a terrestrial flood origin to a sand bed in an estuary. Sediments from Carpinteria Marsh record four wet climate episodes in coastal southern California over the last 7000 years, and six more possible wet episodes of shorter duration.

Flood deposition is especially frequent and associated with the greatest deposition of coarse sediment at 0.3-1 ka, ~2.8-3.6 ka, 3.8-4.2 ka, and 4.9-5.3 ka. The Carpinteria record of floods does not consistently correlate with proxies for ENSO, PDO, or SST, indicating increased winter precipitation associated with flooding in Carpinteria has multiple, complex origins. However, WE1, WE2, and an event at ~6.3 ka are contemporaneous with other records of pluvials throughout the southwest North America, possibly indicating a regional increase in AR frequency during these time periods. The Carpinteria sedimentary record also records periods of decreased flood-derived sedimentation, interpreted here as times of drier climate. The two major dry periods in Carpinteria correspond to regional records of persistent droughts throughout southwest North America. Estuarine sediments in coastal southern California provide an additional archive of paleoclimate information that demonstrate millennial scale storm frequency and magnitude may be similar across a wide geographic span of southwestern North America.

CHAPTER 6

6. Conclusions

The relative sea-level history of southern California is similar to that from other intermediate field locations, showing rapid sea level rise until 5-7 ka at which point sea level rise decelerates to present, averaging 0.8 ± 0.3 mma-1 for the last 4 ka. This sea-level history has been one of the dominant forces shaping the coast of California over the Holocene—it has been proposed that most estuaries in southern California (Ferren, 1985), and deltas throughout the world (Stanley and Warne, 1994), initiated in their present locations when sea level rise began to slow 5-8 ka.

Carpinteria Marsh was a high energy, marine-influenced estuary during this rapid period of sea level rise, indicated by the geochemical indicators, biological content, and grain size of the grey sand at the base of all cores which sample depths of over 10 m. A marsh, characterized by organic rich muds and the presence of *C. californica* shells, was established around 6 ka. Following this transition, the marsh records a 4 kyr period where sedimentation in the marsh kept pace with sea level rise through accretion of fines and input of terrestrial sediments dominantly during flood events. We see evidence for at least 37 episodes of alluvial fan progradation in the last 6 ka, with clusters of events during the Little Ice Age, and in the mid-Holocene, similar to other records (Kirby et al., 2014).

From 3-1 ka the central part of the marsh appears to lack a sedimentary record due to either erosion or non-deposition, perhaps correlative with regional aridity. At 1 ka, the stratigraphy shows an abrupt transition from marsh sediments to subtidal marine-influenced gray sand. We interpret this to indicate an abrupt RSL rise from coseismic subsidence (and associated compaction and erosion) of 1-3.5 m. This subsidence was likely accommodated

along the Rincon Creek Fault, and may be contemporaries with a large uplift event along the Ventura-Pitas Point fault documented at Pitas Point (Rockwell et al., 2016). A relationship between movement along the Rincon Creek Fault and movement along the Ventura-Pitas Point Fault may support the recently proposed potential for long-ruptures and large earthquakes within the Santa Barbara Channel (Hubbard et al., 2014; Marshall et al., 2017; Rockwell et al., 2016).

The estuary maintained this high-energy, marine-influenced state, initiated by subsidence, for about 500 years, although the upper, gradational transition into the low-energy marsh deposits occurred at variable times throughout the marsh. By the historical period, pollen and foraminifera data indicates much of the marsh was characterized by low marsh mudflats and vegetated high marsh regions dominated by pickleweed. In the 1800s, agriculture and development started encroaching on the boundaries of the marsh, and humans began to alter the hydrology of the marsh itself through diking and farming. In 1861-2 a series of large storms eroded the barrier in front of the marsh and deposited a large overwash fan across the marsh surface. This is recorded today as a thick bed of quartz-rich sand interbedded with marsh muds which thins and fines landward within the top meter of sediment in the marsh. Although the 1861-2 storm is historically recorded to have caused a significant amount of inland flooding, the overwash deposit in Carpinteria is the first physical record of the coastal effects of this unique storm season on California.

The 1861-2 overwash deposit, along with increased sediment load (Ejarque et al., 2015; Mudie and Byrne, 1980b) from land use change, enabled the marsh to accrete to its present elevation around MHW. Today the streams entering the marsh are channelized and have debris basins which collect coarse sediments before they reach the coastal plain, therefore the alluvial fans fringing the marsh are currently eroding due to a lack of sediment

supply. Accretion within the marsh has in the past been able to keep up sea level rise—what transitions will occur in the future remains to be seen.

References

Adamson, M., personal communication.

Adamson, M.R., 2002. Oil development and the accomplishment of place. *American sociological review*, *67*(6), pp.911-917.

Adamson, M.R., 2008. Oil booms and boosterism: Local elites, outside companies, and the growth of Ventura, California. *Journal of Urban History*, *35*(1), pp.150-177.

Addison, J. A., Finney, B. P., Jaeger, J. M., Stoner, J. S., Norris, R. D., and Hangsterfer, A., 2013, Integrating satellite observations and modern climate measurements with the recent sedimentary record: An example from Southeast Alaska: Journal of Geophysical Research-Oceans, v. 118, no. 7, p. 3444-3461.

Allan, J. C., and Komar, P. D., 2006, Climate controls on US West Coast erosion processes: Journal of Coastal Research, v. 22, no. 3, p. 511-529.

Anderson, L., Abbott, M.B., Finney, B.P. and Burns, S.J., 2005. Regional atmospheric circulation change in the North Pacific during the Holocene inferred from lacustrine carbonate oxygen isotopes, Yukon Territory, Canada. *Quaternary Research*, *64*(1), pp.21-35.

Anderson, R. S., Starratt, S., Jass, R. M. B., and Pinter, N., 2010, Fire and vegetation history on Santa Rosa Island, Channel Islands, and long-term environmental change in southern California: Journal of Quaternary Science, v. 25, no. 5, p. 782-797.

Appleby P. G. and Oldfield F. (1983) The assessment of 210Pb data from sites with varying sediment accumulation rates. Hydrobiologia 103, 29–35.

Aschmann, H., 1973, Distribution and peculiarity of Mediterranean ecosystems, Mediterranean type ecosystems, Springer, p. 11-19.

Atwater, B. F., 1987, Evidence for great Holocene earthquakes along the outer coast of Washington State: Science, v. 236, no. 4804, p. 942-944.

Atwater, B. F., Hedel, C. W., and Helley, E. J., 1977, Late Quaternary depositional history, Holocene sea-level changes, and vertical crust movement, southern San Francisco Bay, California, US Govt. Print. Off.

Avnaim-Katav, S., Gehrels, W. R., Brown, L. N., Fard, E., and MacDonald, G. M., 2017, Distributions of salt-marsh foraminifera along the coast of SW California, USA: Implications for sea-level reconstructions: Marine Micropaleontology, v. 131, p. 25-43.

Bakker, E., and Slack, G., 1984, An island called California: an ecological introduction to its natural communities, Univ of California Press.

Bard, E., Hamelin, B., Arnold, M., and Montaggioni, L., 1996, Deglacial sea-level record from Tahiti corals and the timing of global meltwater discharge: Nature, v. 382, no. 6588, p. 241.

Barnard, P. L., Short, A. D., Harley, M. D., Splinter, K. D., Vitousek, S., Turner, I. L., Allan, J., Banno, M., Bryan, K. R., Doria, A., Hansen, J. E., Kato, S., Kuriyama, Y., Randall-Goodwin, E., Ruggiero, P., Walker, I. J., and Heathfield, D. K., 2015, Coastal vulnerability across the Pacific dominated by El Niño/Southern Oscillation: Nature Geoscience, v. 8, no. 10, p. 801-+.

Barnard, P. L., van Ormondt, M., Erikson, L. H., Eshleman, J., Hapke, C., Ruggiero, P., Adams, P. N., and Foxgrover, A. C., 2014, Development of the Coastal Storm Modeling System (CoSMoS) for predicting the impact of storms on high-energy, active-margin coasts: Natural Hazards, v. 74, no. 2, p. 1095-1125.

Barron, J. A., Bukry, D., and Hendy, I. L., 2015, High-resolution paleoclimatology of the Santa Barbara Basin during the Medieval Climate Anomaly and early Little Ice Age based on diatom and silicoflagellate assemblages in Kasten core SPR0901-02KC: Quaternary International, v. 387, p. 13-22.

Bartlett, A. S., and Barghoorn, E. S., 1973, Phytogeographic history of the Isthmus of Panama during the past 12,000 years (a history of vegetation, climate, and sea-level change): Vegetation and vegetational history of northern Latin America.

Bawden, G. W., Thatcher, W., Stein, R. S., Hudnut, K. W., and Peltzer, G., 2001, Tectonic contraction across Los Angeles after removal of groundwater pumping effects: Nature, v. 412, no. 6849, p. 812-815.

Bell, J.L., Sloan, L.C. and Snyder, M.A., 2004. Regional changes in extreme climatic events: a future climate scenario. *Journal of Climate*, *17*(1), pp.81-87.

Beller, E. B., S; Grossinger, RM; Longcore, T; Stein, ED; Dark, S; Dusterhoff, SD, 2014, Northern San Diego County Lagoons Historical Ecology Investigation: San Francisco Estuary Institute, v. 7222, p. 215.

Benson, L., Kashgarian, M., Rye, R., Lund, S., Paillet, F., Smoot, J., Kester, C., Mensing, S., Meko, D. and Lindström, S., 2002. Holocene multidecadal and multicentennial droughts affecting Northern California and Nevada. *Quaternary Science Reviews*, *21*(4-6), pp.659-682.

Bentley, M. J., Hodgson, D. A., Smith, J. A., and Cox, N. J., 2005, Relative sea level curves for the South Shetland Islands and Marguerite Bay, Antarctic Peninsula: Quaternary Science Reviews, v. 24, no. 10-11, p. 1203-1216.

Bentz, M., 2016, Establishing Foraminifera Based Biofacies within Shallow Marine Deposits, Carpinteria Slough, CA. Implications for southern California Sea-Level Studies [M.S. Unpublished Master's Thesis]: University of California Santa Barbara.

Blott, S. J., and Pye, K., 2001, GRADISTAT: A grain size distribution and statistics package for the analysis of unconsolidated sediments: Earth Surface Processes and Landforms, v. 26, no. 11, p. 1237-1248.

Bond, G., Kromer, B., Beer, J., Muscheler, R., Evans, M.N., Showers, W., Hoffmann, S., Lotti-Bond, R., Hajdas, I. and Bonani, G., 2001. Persistent solar influence on North Atlantic climate during the Holocene. *Science*, *294*(5549), pp.2130-2136.

Bond, T. C., Bhardwaj, E., Dong, R., Jogani, R., Jung, S. K., Roden, C., Streets, D. G., and Trautmann, N. M., 2007, Historical emissions of black and organic carbon aerosol from energy-related combustion, 1850-2000: Global Biogeochemical Cycles, v. 21, no. 2, p. 16.

Boxt, M. A., Raab, L. M., Davis, O. K., and Pope, K. O., 1999, Extreme Late Holocene climate change in coastal southern California: Pacific Coast Archaeological Society Quarterly, v. 35, no. 2/3, p. 25-37.

Bradley, W. C., and Griggs, G. B., 1976, Form, genesis, and deformation of central California wave-cut platforms: Geological Society of America Bulletin, v. 87, no. 3, p. 433-449.

Brain, M. J., Kemp, A. C., Horton, B. P., Culver, S. J., Parnell, A. C., and Cahill, N., 2014, Quantifying the contribution of sediment compaction to late Holocene salt-marsh sea-level reconstructions, North Carolina, USA: Quaternary Research.

Brain, M. J., Long, A. J., Petley, D. N., Horton, B. P., and Allison, R. J., 2011, Compression behaviour of minerogenic low energy intertidal sediments: Sedimentary Geology, v. 233, no. 1-4, p. 28-41.

Brain, M. J., Long, A. J., Woodroffe, S. A., Petley, D. N., Milledge, D. G., and Parnell, A. C., 2012, Modelling the effects of sediment compaction on salt marsh reconstructions of recent sea-level rise: Earth and Planetary Science Letters, v. 345, p. 180-193.

Brevik, E. C., and Homburg, J. A., 2004, A 5000 year record of carbon sequestration from a coastal lagoon and wetland complex, Southern California, USA: Catena, v. 57, no. 3, p. 221-232.

Bromirski, P. D., Miller, A. J., Flick, R. E., and Auad, G., 2011, Dynamical suppression of sea level rise along the Pacific coast of North America: Indications for imminent acceleration: Journal of Geophysical Research: Oceans, v. 116, no. C7.

Cai, W., Borlace, S., Lengaigne, M., Van Rensch, P., Collins, M., Vecchi, G., Timmermann, A., Santoso, A., McPhaden, M.J., Wu, L. and England, M.H., 2014. Increasing frequency of extreme El Niño events due to greenhouse warming. *Nature climate change*, *4*(2), p.111.

Caldwell, J. C., 1979, Carpinteria as it was, Papillon Press.

Campos, J., 2007, Carpinteria, Charleston, SC, Arcadia Pub., Images of America, 127 pages p.:

Cayan, D. R., and Peterson, D. H., 1989, The influence of North Pacific atmospheric circulation on streamflow in the west: Aspects of climate variability in the Pacific and the western Americas, p. 375-397.

Chappell, J., and Polach, H., 1991, Post-glacial sea-level rise from a coral record at Huon Peninsula, Papua New Guinea: Nature, v. 349, no. 6305, p. 147-149.

Church, J. A., Clark, P. U., Cazenave, A., Gregory, J. M., Jevrejeva, S., Levermann, A., Merrifield, M. A., Milne, G. A., Nerem, R. S., and Nunn, P. D., 2013, Climate change 2013: the physical science basis. Contribution of Working Group I to the Fifth Assessment Report of the Intergovernmental Panel on Climate Change: Sea level change, p. 1137-1216.

Clague, J., Harper, J. R., Hebda, R. J., and Howes, D. E., 1982, Late Quaternary sea levels and crustal movements, coastal British Columbia: Canadian Journal of Earth Sciences, v. 19, no. 3, p. 597-618.

Clark, J., Mitrovica, J. X., and Alder, J., 2014, Coastal paleogeography of the California-Oregon-Washington and Bering Sea continental shelves during the latest Pleistocene and Holocene: implications for the archaeological record: Journal of Archaeological Science, v. 52, p. 12-23.

Clark, J. A., Farrell, W. E., and Peltier, W. R., 1978, Global changes in post-glacial sea-level numerical calculation: Quaternary Research, v. 9, no. 3, p. 265-287.

Coan, E. V., Scott, P. V., and Bernard, F. R., 2000, Bivalve seashells of western North America: marine bivalve mollusks from Arctic Alaska to Baja California, Santa Barbara Museum of Natural History, v. 2.

Cole, K. L., and Liu, G. W., 1994, Holocene paleoecology of an estuary on Santa Rosa Island, California Quaternary Research, v. 41, no. 3, p. 326-335.

Cole, K. L., and Wahl, E., 2000, A Late Holocene Paleoecological Record from Torrey Pines State Reserve, California: Quaternary Research, v. 53, no. 3, p. 341-351.
Conroy, J.L., Overpeck, J.T. and Cole, J.E., 2010. El Niño/Southern Oscillation and changes in the zonal gradient of tropical Pacific sea surface temperature over the last 1.2 ka. *PAGES news*, *18*(1), pp.32-34.
Cook, E.R. and Krusic, P.J., 2004. The North American Drought Atlas. Lamont-Doherty Earth Observatory and the National Science Foundation.
Creveling, J. R., Mitrovica, J. X., Hay, C. C., Austermann, J., and Kopp, R. E., 2015, Revisiting tectonic corrections applied to Pleistocene sea-level highstands: Quaternary Science Reviews, v. 111, p. 72-80.
Dalrymple, R. W., Zaitlin, B. A., and Boyd, R., 1992, Estuarine facies models: conceptual basis and stratigraphic implications: perspective: Journal of Sedimentary Research, v. 62, no. 6.
Davis, O. K., 1992, Rapid climatic change in coastal southern California inferred from pollen analysis of San Joaquin Marsh Quaternary Research, v. 37, no. 1, p. 89-100.
Davis, O. K., 1996, Pollen analysis of Newport Bay, Orange County, California in association with excavation of CA-ORA-64., Report submitted to Michael Macko, Macko Inc.: Santa Ana Heights, CA.
Dettinger, M., 2011, Climate Change, Atmospheric Rivers, and Floods in California - A Multimodel Analysis of Storm Frequency and Magnitude Changes: Journal of the American Water Resources Association, v. 47, no. 3, p. 514-523.
Dettinger, M. D., and Ingram, B. L., 2013, The coming megafloods: Scientific American, v. 308, no. 1, p. 64-71.
Dettinger, M. D., Ralph, F. M., Das, T., Neiman, P. J., and Cayan, D. R., 2011, Atmospheric Rivers, Floods and the Water Resources of California: Water, v. 3, no. 2, p. 445-478.
Dibblee Jr, T. W., and Ehrenspeck, H., 1986, Geologic map of the Carpinteria quadrangle: Thomas Dibblee, J. Geological Foundation.
Donnelly, C., Kraus, N., and Larson, M., 2006, State of knowledge on measurement and modeling of coastal overwash: Journal of Coastal Research, v. 22, no. 4, p. 965-991.
Donnelly, J. P., Butler, J., Roll, S., Wengren, M., and Webb, T., 2004, A backbarrier overwash record of intense storms from Brigantine, New Jersey: Marine Geology, v. 210, no. 1-4, p. 107-121.
Drake, D., Kolpack, R., and Fischer, P., 1972, Sediment transport on the Santa Barbara-Oxnard shelf, Santa Barbara Channel, California: IN: SHELF SEDIMENT TRANSPORT: PROCESS AND PATTERN.
Draut, A. E., Hart, P. E., Lorenson, T. D., Ryan, H. F., Wong, F. L., Sliter, R. W., and Conrad, J. E., 2009, Late Pleistocene to Holocene sedimentation and hydrocarbon seeps on the continental shelf of a steep, tectonically active margin, southern California, USA: Marine Geophysical Researches, v. 30, no. 3, p. 193-206.
Drummond, K., 1981, Plate tectonic map of the Circum-Pacific region, northeast quadrant: Am. Assoc. of Pet. Geol., Tulsa, Okla.
Du, X., Hendy, I., and Schimmelmann, A., 2018, A 9000-year flood history for Southern California: A revised stratigraphy of varved sediments in Santa Barbara Basin: Marine Geology, v. 397, p. 29-42.
Dupont, L., and Kuhlmann, H., 2017, Glacial-interglacial vegetation change in the Zambezi catchment: Quaternary Science Reviews, v. 155, p. 127-135.

Edwards, R. J., and Horton, B. P., 2006, Developing detailed records of relative sea-level change using a foraminiferal transfer function: an example from North Norfolk, UK: Philosophical Transactions of the Royal Society a-Mathematical Physical and Engineering Sciences, v. 364, no. 1841, p. 973-991.

Ejarque, A., Anderson, R. S., Simms, A. R., and Gentry, B. J., 2015, Prehistoric fires and the shaping of colonial transported landscapes in southern California: A paleoenvironmental study at Dune Pond, Santa Barbara County: Quaternary Science Reviews, v. 112, p. 181-196.

Ellison, J. C., 1989, Polle analysis of mangrove sediments as a sea-level indicator-assessment from Tongatapu, Tonga Palaeogeography Palaeoclimatology Palaeoecology, v. 74, no. 3-4, p. 327-341.

Elwany, M. H. S., 2011, Characteristics, restoration, and enhancement of Southern California lagoons: Journal of Coastal Research, p. 246-255.

Ely, L. L., 1997, Response of extreme floods in the southwestern United States to climatic variations in the late Holocene: Geomorphology, v. 19, no. 3-4, p. 175-201.

Engelhart, S. E., Horton, B. P., Douglas, B. C., Peltier, W. R., and Tornqvist, T. E., 2009, Spatial variability of late Holocene and 20(th) century sea-level rise along the Atlantic coast of the United States: Geology, v. 37, no. 12, p. 1115-1118.

Engelhart, S. E., Horton, B. P., and Kemp, A. C., 2011, Holocene Sea Level Changes Along the United States' Atlantic Coast: Oceanography, v. 24, no. 2, p. 70-79.

Engelhart, S. E., Vacchi, M., Horton, B. P., Nelson, A. R., and Kopp, R. E., 2015, A sea-level database for the Pacific coast of central North America: Quaternary Science Reviews, v. 113, no. 0, p. 78-92.

Engstrom, W. N., 1996, The California storm of January 1862: Quaternary Research, v. 46, no. 2, p. 141-148.

Enzel, Y., Ely, L. L., House, P. K., Baker, V. R., and Webb, R. H., 1993, Paleoflood evidence for a natural upper bound to flood magnitudes in the Colorado River Basin: Water Resources Research, v. 29, no. 7, p. 2287-2297.

Esau, E., 2006, Images of the Pacific Rim: Australia and California, 1850-1935, Power Publications.

Faegri, K., Kaland, P. E., and Krzywinski, K., 1989, Textbook of pollen analysis, John Wiley & Sons Ltd., v. Ed. 4.

Fairbanks, R. G., 1989, A 17,000-year glacio-eustatic sea level record: influence of glacial melting rates on the Younger Dryas event and deep-ocean circulation: Nature, v. 342, no. 6250, p. 637-642.

Fenzel, F.W. and Price, M., 1971. *Flood of January 1969 Near Carpinteria, California* (No. 422).

Ferren, W. R., 1985, Carpinteria Salt Marsh: environment, history, and botanical resources of a southern California estuary, Herbarium, Dept. of Biological Sciences, University of California, Santa Barbara, v. 4.

Florsheim, J., Fishbain, L. and Williams, P., 1991. Geomorphic analysis for enhancement and restoration of the Tijuana Estuary, California. In *Coastal Zone'91* (pp. 2108-2121). ASCE.

Fredrickson, S. M., 2016, The Geomorphic Transition between the Santa Barbara and Ventura Fold Belts near Rincon Point, California: University of California, Santa Barbara.

Friddell, J. E., Thunell, R. C., Guilderson, T. P., and Kashgarian, M., 2003, Increased northeast Pacific climatic variability during the warm middle Holocene: Geophysical Research Letters, v. 30, no. 11.

García-García, A., Levey, M. D., and Watson, E. B., 2013, High resolution seismic study of the Holocene infill of the Elkhorn Slough, central California: Continental Shelf Research, v. 55, p. 108-118.

Gilbert, S., 2004, A Cultural Resource Study of Historical Features at Carpinteria State Beach, Santa Barbara County, California. : Brian F. Smith and Associates.

Goff, J., Chagué-Goff, C., Nichol, S., Jaffe, B., and Dominey-Howes, D., 2012, Progress in palaeotsunami research: Sedimentary Geology, v. 243, p. 70-88.

Grant, L. B., Ballenger, L. J., and Runnerstrom, E. E., 2002, Coastal uplift of the San Joaquin Hills, southern Los Angeles Basin, California, by a large earthquake since AD 1635: Bulletin of the Seismological Society of America, v. 92, no. 2, p. 590-599.

Grant, L. B., Waggoner, J. T., Rockwell, T. K., and vonStein, C., 1997, Paleoseismicity of the north branch of the Newport-Inglewood fault zone in Huntington Beach, California, from cone penetrometer test data: Bulletin of the Seismological Society of America, v. 87, no. 2, p. 277-293.

Grayson, D.K., 2000. Mammalian responses to Middle Holocene climatic change in the Great Basin of the western United States. *Journal of Biogeography*, *27*(1), pp.181-192.

Grossinger, R., Stein, E. D., Cayce, K., Askevold, R., Dark, S., and Whipple, A., 2011, Historical Wetlands of the Southern California Coast: An Atlas of US Coast Survey T-sheets, 1851-1889, San Francisco Estuary Institute Oakland.

Guinn, J. M., 1890, Exceptional years: a history of California floods and drought: Historical Society of Southern California, Los Angeles (1890), v. 1, no. 5, p. 33-39.

Gupta, S. K., and Polach, H. A., 1985, Radiocarbon dating practices at ANU.

Gurrola, L. D., Keller, E. A., Chen, J. H., Owen, L. A., and Spencer, J. Q., 2014, Tectonic geomorphology of marine terraces: Santa Barbara fold belt, California: Geological Society of America Bulletin, v. 126, no. 1-2, p. 219-233.

Hamilton, S., and Shennan, I., 2005, Late Holocene relative sea-level changes and the earthquake deformation cycle around upper Cook Inlet, Alaska: Quaternary Science Reviews, v. 24, no. 12-13, p. 1479-1498.

Harms, S. and Winant, C.D., 1998. Characteristic patterns of the circulation in the Santa Barbara Channel. *Journal of Geophysical Research: Oceans*, *103*(C2), pp.3041-3065.

Harris, S. M., 2013, A Comprehensive Analysis of Precipitation in Santa Barbara, California, on Hourly to Interannual Timescales, University of California, Santa Barbara.

Harris, S. M., and Carvalho, L. M. V., 2017, Characteristics of southern California atmospheric rivers: Theoretical and Applied Climatology.

Hawkes, A. D., and Horton, B. P., 2012, Sedimentary record of storm deposits from Hurricane Ike, Galveston and San Luis Islands, Texas: Geomorphology, v. 171, p. 180-189.

Hawkes, A. D., Horton, B. P., Nelson, A. R., and Hill, D. F., 2010, The application of intertidal foraminifera to reconstruct coastal subsidence during the giant Cascadia earthquake of AD 1700 in Oregon, USA: Quaternary International, v. 221, no. 1-2, p. 116-140.

Hendy, I. L., Dunn, L., Schimmelmann, A., and Pak, D. K., 2013, Resolving varve and radiocarbon chronology differences during the last 2000 years in the Santa Barbara Basin sedimentary record, California: Quaternary International, v. 310, p. 155-168.
Hendy, I. L., Napier, T. J., and Schimmelmann, A., 2015, From extreme rainfall to drought: 250 years of annually resolved sediment deposition in Santa Barbara Basin, California: Quaternary International, v. 387, p. 3-12.
Hennekam, R., and de Lange, G., 2012, X-ray fluorescence core scanning of wet marine sediments: methods to improve quality and reproducibility of high-resolution paleoenvironmental records: Limnology and Oceanography: Methods, v. 10, no. 12, p. 991-1003.
Hennessy, J. T., and Zarillo, G. A., 1987, The interrelation and distinction between flood-tidal delta and washover deposits in a transgressive barrier-island: Marine Geology, v. 78, no. 1-2, p. 35-56.
Heusser, L. E., Hendy, I. L., and Barron, J. A., 2015, Vegetation response to southern California drought during the Medieval Climate Anomaly and early Little Ice Age (AD 800–1600): Quaternary International, v. 387, p. 23-35.
Hill, D. F., Griffiths, S. D., Peltier, W. R., Horton, B. P., and Tornqvist, T. E., 2011, High-resolution numerical modeling of tides in the western Atlantic, Gulf of Mexico, and Caribbean Sea during the Holocene: Journal of Geophysical Research-Oceans, v. 116, p. 16.
Hiner, C. A., Kirby, M. E., Bonuso, N., Patterson, W. P., Palermo, J., and Silveira, E., 2016, Late Holocene hydroclimatic variability linked to Pacific forcing: evidence from Abbott Lake, coastal central California: Journal of Paleolimnology, v. 56, no. 4, p. 299-313.
Hirabayashi, S., Yokoyama, Y., Suzuki, A., Miyairi, Y., and Aze, T., 2017, Multidecadal oceanographic changes in the western Pacific detected through high-resolution bomb-derived radiocarbon measurements on corals: Geochemistry Geophysics Geosystems, v. 18, no. 4, p. 1608-1617.
Holmquist, J. R., Reynolds, L., Brown, L. N., Southon, J. R., Simms, A. R., and MacDonald, G. M., 2015, Marine radiocarbon reservoir values in southern California estuaries: interspecies, latitudinal, and interannual variability: Radiocarbon, v. 57, no. 3, p. 449-458.
Hornberger, M. I., 1991, Paleoenvironment of Elkhorn Slough and surrounding wetland habitats: a geological study using an ecological approach.
Horton, B. P., Edwards, R. J., and Lloyd, J. M., 1999, A foraminiferal-based transfer function: Implications for sea-level studies: Journal of Foraminiferal Research, v. 29, no. 2, p. 117-129.
Horton, B. P., Engelhart, S. E., Hill, D. F., Kemp, A. C., Nikitina, D., Miller, K. G., and Peltier, W. R., 2013, Influence of tidal-range change and sediment compaction on Holocene relative sea-level change in New Jersey, USA: Journal of Quaternary Science, v. 28, no. 4, p. 403-411.
Hubbard, J., Shaw, J. H., Dolan, J., Pratt, T. L., McAuliffe, L., and Rockwell, T. K., 2014, Structure and seismic hazard of the Ventura Avenue anticline and Ventura fault, California: Prospect for large, multisegment ruptures in the western Transverse Ranges: Bulletin of the Seismological Society of America.

Hughes, M. W., Quigley, M. C., van Ballegooy, S., Deam, B. L., Bradley, B. A., and Hart, D. E., 2015, The sinking city: Earthquakes increase flood hazard in Christchurch, New Zealand: GSA Today, v. 25, no. 3.

Imakiire, T., and Koarai, M., 2012, Wide-area land subsidence caused by "the 2011 Off the Pacific Coast of Tohoku Earthquake": Soils and Foundations, v. 52, no. 5, p. 842-855.

Ingram, B. L., and Southon, J. R., 1996, Reservoir ages in eastern Pacific coastal and estuarine waters: Radiocarbon, v. 38, no. 3, p. 573-582.

Inman, D. L., 1983, Application of coastal dynamics to the reconstruction of paleocoastlines in the vicinity of La Jolla, California: Quaternary coastlines and marine archaeology, p. 1-49.

Jackson, P. A., and Yeats, R. S., 1982, Structural evolution of Carpinteria basin, western Transverse Ranges, California Aapg Bulletin-American Association of Petroleum Geologists, v. 66, no. 7, p. 805-829.

Jaramillo, E., Melnick, D., Baez, J. C., Montecino, H., Lagos, N. A., Acuña, E., Manzano, M., and Camus, P. A., 2017, Calibrating coseismic coastal land-level changes during the 2014 Iquique (Mw= 8.2) earthquake (northern Chile) with leveling, GPS and intertidal biota: PloS one, v. 12, no. 3, p. e0174348.

Jennings, C. W., and Saucedo, G. J., 1994, Fault activity map of California and adjacent areas, with locations and ages of recent volcanic eruptions, California Department of Conservation, Division of Mines and Geology.

Johnson, S. Y., Hartwell, S. R., Sorlien, C. C., Dartnell, P., and Ritchie, A. C., 2017, Shelf evolution along a transpressive transform margin, Santa Barbara Channel, California: Geosphere.

Jong, B.-T., Ting, M., Seager, R., Henderson, N., and Lee, D. E., 2017, Role of Equatorial Pacific SST forecast error in the late winter California precipitation forecast for the 2015/16 El Niño: Journal of Climate, no. 2017.

Juggins, S., 2011, C2 Data Analysis Version 1.7. 2: Newcastle upon Tyne: University of Newcastle.

Kamerling, M., Sorlien, C., and Nicholson, C., 2003, 3D development of an active oblique fault system, northern Santa Barbara Channel, California: Seismol. Res. Lett, v. 74, no. 2, p. 248.

Keefer, D.K., 1994. The importance of earthquake-induced landslides to long-term slope erosion and slope-failure hazards in seismically active regions. In *Geomorphology and Natural Hazards* (pp. 265-284).

Kemp, A. C., Horton, B. P., Donnelly, J. P., Mann, M. E., Vermeer, M., and Rahmstorf, S., 2011, Climate related sea-level variations over the past two millennia: Proceedings of the National Academy of Sciences of the United States of America, v. 108, no. 27, p. 11017-11022.

Kennett, D. J., Ingram, B. L., Erlandson, J. M., and Walker, P., 1997, Evidence for temporal fluctuations in marine radiocarbon reservoir ages in the Santa Barbara Channel, southern California: Journal of Archaeological Science, v. 24, no. 11, p. 1051-1059.

Kennett, D. J., Kennett, J. P., Erlandson, J. M., and Cannariato, K. G., 2007, Human responses to Middle Holocene climate change on California's Channel Islands: Quaternary Science Reviews, v. 26, no. 3-4, p. 351-367.

Kirby, M., Lund, S., Patterson, W., Anderson, M., Bird, B., Ivanovici, L., Monarrez, P., and Nielsen, S., 2010, A Holocene record of Pacific decadal oscillation (PDO)-related

hydrologic variability in southern California (Lake Elsinore, CA): Journal of Paleolimnology, v. 44, no. 3, p. 819-839.
Kirby, M. E., Feakins, S. J., Hiner, C. A., Fantozzi, J., Zimmerman, S. R. H., Dingemans, T., and Mensing, S. A., 2014, Tropical Pacific forcing of Late-Holocene hydrologic variability in the coastal southwest United States: Quaternary Science Reviews, v. 102, p. 27-38.
Kirby, M. E., Zimmerman, S. R., Patterson, W. P., and Rivera, J. J., 2012, A 9170-year record of decadal-to-multi-centennial scale pluvial episodes from the coastal Southwest United States: a role for atmospheric rivers?: Quaternary Science Reviews, v. 46, p. 57-65.
Kirwan, M.L., Temmerman, S., Skeehan, E.E., Guntenspergen, G.R. and Fagherazzi, S., 2016. Overestimation of marsh vulnerability to sea level rise. *Nature Climate Change*, *6*(3), p.253.
Kirwan, M.L., Temmerman, S., Guntenspergen, G.R. and Fagherazzi, S., 2017. Reply to'Marsh vulnerability to sea-level rise'. *Nature Climate Change*, *7*(11), p.756.
Kleppe, J.A., Brothers, D.S., Kent, G.M., Biondi, F., Jensen, S. and Driscoll, N.W., 2011. Duration and severity of Medieval drought in the Lake Tahoe Basin. *Quaternary Science Reviews*, *30*(23-24), pp.3269-3279.
Konrad, S.K. and Clark, D.H., 1998. Evidence for an early Neoglacial glacier advance from rock glaciers and lake sediments in the Sierra Nevada, California, USA. *Arctic and Alpine Research*, pp.272-284.
Kuhn, G. G., and Shepard, F. P., 1984, Sea Cliffs, Beaches, and Coastal Valleys of San Diego County: Some Amazing Histories and Some Horrifying Implications, Univ of California Press.
Kuwatani, T., Nagata, K., Okada, M., Watanabe, T., Ogawa, Y., Komai, T., and Tsuchiya, N., 2014, Machine-learning techniques for geochemical discrimination of 2011 Tohoku tsunami deposits: Scientific reports, v. 4.
Lafferty, K. D., 2005, Assessing estuarine biota in southern California: Planning for Biodiversity: Bringing Research and Management Together, p. 1.
Lajoie, K., Kern, J., Wehmiller, J., Kennedy, G., Mathieson, S., Sarna-Wojcicki, A., Yerkes, R., and McCrory, P., 1979, Quaternary marine shorelines and crustal deformation, San Diego to Santa Barbara, California: Geological Excursions in the Southern California Area. San Diego State Univ., San Diego, CA.
Lajoie, K. R., Sarna-Wojcicki, A. M., and Yerkes, R. F., 1982, Quaternary chronology and rates of crustal deformation in the Ventura area, California.
Lambeck, K., and Chappell, J., 2001, Sea level change through the last glacial cycle: Science, v. 292, no. 5517, p. 679-686.
Lambeck, K., Rouby, H., Purcell, A., Sun, Y. Y., and Sambridge, M., 2014, Sea level and global ice volumes from the Last Glacial Maximum to the Holocene: Proceedings of the National Academy of Sciences of the United States of America, v. 111, no. 43, p. 15296-15303.
Lambeck, K., Smither, C., and Johnston, P., 1998, Sea-level change, glacial rebound and mantle viscosity for northern Europe: Geophysical Journal International, v. 134, no. 1, p. 102-144.
Lavers, D. A., Allan, R. P., Wood, E. F., Villarini, G., Brayshaw, D. J., and Wade, A. J., 2011, Winter floods in Britain are connected to atmospheric rivers: Geophysical Research Letters, v. 38.

Le Dantec, N., Hogarth, L. J., Driscoll, N. W., Babcock, J. M., Barnhardt, W. A., and Schwab, W. C., 2010, Tectonic controls on nearshore sediment accumulation and submarine canyon morphology offshore La Jolla, Southern California: Marine Geology, v. 268, no. 1, p. 115-128.

Leeper, R., Rhodes, B., Kirby, M., Scharer, K., Carlin, J., Hemphill-Haley, E., Avnaim-Katav, S., MacDonald, G., Starratt, S., and Aranda, A., 2017, Evidence for coseismic subsidence events in a southern California coastal saltmarsh: Scientific Reports, v. 7.

Leonard, L. J., Hyndman, R. D., and Mazzotti, S., 2004, Coseismic subsidence in the 1700 great Cascadia earthquake: Coastal estimates versus elastic dislocation models: Geological Society of America Bulletin, v. 116, no. 5-6, p. 655-670.

Lindström, S., 1990. Submerged tree stumps as indicators of mid-Holocene aridity in the Lake Tahoe Basin. *Journal of California and Great Basin Anthropology*, *12*(2), pp.146-157.

Livsey, D., and Simms, A. R., 2013, Holocene sea-level change derived from microbial mats: Geology, v. 41, no. 9, p. 971-974.

Lohmar, J. M., Macdonald, K. B., and Janes, S. A., 1980, Late Pleistocene-Holocene Sedimentary Infilling and Faunal Change in a Southern California Coastal Lagoon.

Mantua, N.J. and Hare, S.R., 2002. The Pacific decadal oscillation. *Journal of oceanography*, *58*(1), pp.35-44.

Marshall, S. T., Funning, G. J., Krueger, H. E., Owen, S. E., and Loveless, J. P., 2017, Mechanical models favor a ramp geometry for the Ventura-pitas point fault, California: Geophysical Research Letters, v. 44, no. 3, p. 1311-1319.

Marshall, S. T., Funning, G. J., and Owen, S. E., 2013, Fault slip rates and interseismic deformation in the western Transverse Ranges, California: Journal of Geophysical Research: Solid Earth, v. 118, no. 8, p. 4511-4534.

Masters, P. M., 1988, Paleo-Environmental Reconstruction of San Diego Bay, 10,000 Years BP to Present: Five Thousand Years of Maritime Subsistence at Ballast Point Prehistoric Site SDI-48 (W-164), San Diego, California, by Dennis Gallegos and Carolyn Kyle, Section, v. 4.

Masters, P. M., 2006, Holocene sand beaches of southern California: ENSO forcing and coastal processes on millennial scales: Palaeogeography Palaeoclimatology Palaeoecology, v. 232, no. 1, p. 73-95.

McMillan, K., Vincent, M., and Lopez, W., Holocene stratigraphy and timing of sea level on-lap, Huntington Beach, California, *in* Proceedings XVI INQUA Congress, Session2003, p. 242.

McNeilan, T. W., Rockwell, T. K., and Resnick, G. S., 1996, Style and rate of Holocene slip, Palos Verdes fault, southern California: Journal of Geophysical Research: Solid Earth, v. 101, no. B4, p. 8317-8334.

Mensing, S. A., Sharpe, S. E., Tunno, I., Sada, D. W., Thomas, J. M., Starratt, S., and Smith, J., 2013, The Late Holocene Dry Period: multiproxy evidence for an extended drought between 2800 and 1850 cal yr BP across the central Great Basin, USA: Quaternary Science Reviews, v. 78, p. 266-282.

Meyer, J. A., New relative holocene sea-level curve for San Franicsco Bay, California, USA, *in* Proceedings 2014 GSA Annual Meeting in Vancouver, British Columbia2014.

Milker, Y., Horton, B. P., Vane, C. H., Engelhart, S. E., Nelson, A. R., Witter, R. C., Khan, N. S., and Bridgeland, W. T., 2015, Annual and seasonal distribution of intertidal

foraminifera and stable carbon isotope geochemistry, Bandon Marsh, Oregon, USA: Journal of Foraminiferal Research, v. 45, no. 2, p. 146-155.
Miller, D. M., Schmidt, K. M., Mahan, S. A., McGeehin, J. P., Owen, L. A., Barron, J. A., Lehmkuhl, F., and Löhrer, R., 2010, Holocene landscape response to seasonality of storms in the Mojave Desert: Quaternary International, v. 215, no. 1-2, p. 45-61.
Mitrovica, J. X., Gomez, N., Morrow, E., Hay, C., Latychev, K., and Tamisiea, M. E., 2011, On the robustness of predictions of sea level fingerprints: Geophysical Journal International, v. 187, no. 2, p. 729-742.
Mitrovica, J. X., Milne, G. A., and Davis, J. L., 2001, Glacial isostatic adjustment on a rotating earth: Geophysical Journal International, v. 147, no. 3, p. 562-578.
Mitrovica, J. X., and Peltier, W. R., 1991, On postglacial geoid subsidence over the equatorial oceans Journal of Geophysical Research-Solid Earth, v. 96, no. B12, p. 20053-20071.
Morton, R. A., and Sallenger, A. H., 2003, Morphological impacts of extreme storms on sandy beaches and barriers: Journal of Coastal Research, v. 19, no. 3, p. 560-573.
Moy, C.M., Seltzer, G.O., Rodbell, D.T. and Anderson, D.M., 2002. Variability of El Niño/Southern Oscillation activity at millennial timescales during the Holocene epoch. *Nature, 420*(6912), p.162.
Mudie, P. J., and Byrne, R., 1980a, Pollen evidence for historic sedimentation-rates in California coastal marshes: Estuarine and Coastal Marine Science, v. 10, no. 3, p. 305-316.
-, 1980b, Pollen evidence for historic sedimentation rates in California coastal marshes: Estuarine and Coastal Marine Science, v. 10, no. 3, p. 305-316.
Muhs, D. R., Simmons, K. R., Kennedy, G. L., Ludwig, K. R., and Groves, L. T., 2006, A cool eastern Pacific Ocean at the close of the last interglacial complex: Quaternary Science Reviews, v. 25, no. 3, p. 235-262.
Muhs, D. R., Simmons, K. R., Schumann, R. R., Groves, L. T., DeVogel, S. B., Minor, S. A., and Laurel, D., 2014, Coastal tectonics on the eastern margin of the Pacific Rim: late Quaternary sea-level history and uplift rates, Channel Islands National Park, California, USA: Quaternary Science Reviews, v. 105, p. 209-238.
Muhs, D. R., Simmons, K. R., Schumann, R. R., Groves, L. T., Mitrovica, J. X., and Laurel, D., 2012, Sea-level history during the Last Interglacial complex on San Nicolas Island, California: implications for glacial isostatic adjustment processes, paleozoogeography and tectonics: Quaternary Science Reviews, v. 37, p. 1-25.
Naftlay, M., 1998, 1998 Flood Report Santa Barbara County, *in* District, S. B. C. F. C. a. W. C., ed.
Nardin, T. R., Osborne, R. H., Bottjer, D. J., and Scheidemann, R. C., 1981, Holocene sea-level curvers for Santa Monica shelf, California, continental boderland Science, v. 213, no. 4505, p. 331-333.
Negrini, R.M., Wigand, P.E., Draucker, S., Gobalet, K., Gardner, J.K., Sutton, M.Q. and Yohe II, R.M., 2006. The Rambla highstand shoreline and the Holocene lake-level history of Tulare Lake, California, USA. *Quaternary Science Reviews, 25*(13-14), pp.1599-1618.
Nehring, R., 1975, Oil and Gas Supplies for California: Past and Future, Rand.org.
Nelson, A. R., 1992, Holocene tidal-marsh stratigraphy in south-central Oregon-Evidence for localized sudden submergence in the Cascadia subduction zone.

Nelson, A. R., Ota, Y., Umitsu, M., Kashima, K., and Matsushima, Y., 1998, Seismic or hydrodynamic control of rapid late-Holocene sea-level rises in southern coastal Oregon, USA?: The Holocene, v. 8, no. 3, p. 287-299.
Nelson, A. R., Shennan, I., and Long, A. J., 1996, Identifying coseismic subsidence in tidal-wetland stratigraphic sequences at the Cascadia subduction zone of western North America: Journal of Geophysical Research: Solid Earth, v. 101, no. B3, p. 6115-6135.
Nichols, F. H., Cloern, J. E., Luoma, S. N., and Peterson, D. H., 1986, The modification of an estuary: Science(Washington), v. 231, no. 4738, p. 567-573.
NOAA, 2009-2011, Coastal Conservancy Coastal Lidar Project: Hydro-flattened bare earth DEM.
Orme, A. R., 1990, The instability of Holocene coastal dunes: the case of the Morro dunes, California: Coastal dunes: form and process, p. 319-340.
Palacios-Fest, M., Homburg, J., Brevik, E., Orme, A., Davis, O., and Shelley, S., 2006, Paleoecología del Cuaternario Tardío en la Laguna de Ballona en el sur de California (Late Quaternary palaeoecology of Ballona Lagoon in southern California): Ciencias Marinas, v. 32, no. 3, p. 485-504.
Parnell, A. C., Haslett, J., Allen, J. R. M., Buck, C. E., and Huntley, B., 2008, A flexible approach to assessing synchroneity of past events using Bayesian reconstructions of sedimentation history: Quaternary Science Reviews, v. 27, no. 19-20, p. 1872-1885.
Patsch, K., and Griggs, G., 2006, Littoral cells, sand budgets, and beaches: understanding California's shoreline, Institute of Marine Sciences, University of California, Santa Cruz.
Paul, M. A., and Barras, B. F., 1998, A geotechnical correction for post-depositional sediment compression: examples from the Forth valley, Scotland: Journal of Quaternary Science, v. 13, no. 2, p. 171-176.
Peltier, W. R., 2002, On eustatic sea level history: Last Glacial Maximum to Holocene: Quaternary Science Reviews, v. 21, no. 1–3, p. 377-396.
Petersen, K. S., 1986, Marine molluscs as indicators of former sea-level stands, Springer.
Phantuwongraj, S., Choowong, M., Nanayama, F., Hisada, K. I., Charusiri, P., Chutakositkanon, V., Pailoplee, S., and Chabangbon, A., 2013, Coastal geomorphic conditions and styles of storm surge washover deposits from Southern Thailand: Geomorphology, v. 192, p. 43-58.
Pirazzoli, P. A., 1991, World atlas of Holocene sea-level changes: Elsevier Oceanography Series, v. 58, p. 1-280.
Plesch, A., Shaw, J. H., Benson, C., Bryant, W. A., Carena, S., Cooke, M., Dolan, J., Fuis, G., Gath, E., and Grant, L., 2007, Community fault model (CFM) for southern California: Bulletin of the Seismological Society of America, v. 97, no. 6, p. 1793-1802.
Porter, K., Wein, A., Alpers, C., Hughes, M., Neiman, P., and Ralph, F., 2011, Overview of the ARkStorm scenario.
Punt, W., Blackmore, S., Hoen, P., and Stafford, P., 1976-2009, The northwest European pollen flora, Elsevier.
Ralph, F. M., and Dettinger, M. D., 2011, Storms, floods, and the science of atmospheric rivers: Eos, Transactions American Geophysical Union, v. 92, no. 32, p. 265-266.

Ralph, F. M., Neiman, P. J., Wick, G. A., Gutman, S. I., Dettinger, M. D., Cayan, D. R., and White, A. B., 2006, Flooding on California's Russian River: Role of atmospheric rivers: Geophysical Research Letters, v. 33, no. 13, p. n/a-n/a.

Reeder-Myers, L., Erlandson, J. M., Muhs, D. R., and Rick, T. C., 2015, Sea level, paleogeography, and archeology on California's Northern Channel Islands: Quaternary Research, v. 83, no. 2, p. 263-272.

Reid, I. and Laronne, J.B., 1995. Bed load sediment transport in an ephemeral stream and a comparison with seasonal and perennial counterparts. *Water Resources Research*, *31*(3), pp.773-781.

Reille, M., 1992, Pollen et spores d'Europe et d'Afrique du Nord. Marseille: Lab: Bot. Hist. & Palynol. URA CNRS/Univ. Marseille III.

Reimer, P. J., Bard, E., Bayliss, A., Beck, J. W., Blackwell, P. G., Ramsey, C. B., Buck, C. E., Cheng, H., Edwards, R. L., Friedrich, M., Grootes, P. M., Guilderson, T. P., Haflidason, H., Hajdas, I., Hatte, C., Heaton, T. J., Hoffmann, D. L., Hogg, A. G., Hughen, K. A., Kaiser, K. F., Kromer, B., Manning, S. W., Niu, M., Reimer, R. W., Richards, D. A., Scott, E. M., Southon, J. R., Staff, R. A., Turney, C. S. M., and van der Plicht, J., 2013, INTCAL13 and MARINE13 radiocarbon age calibration curves 0-50,000 years cal BP: Radiocarbon, v. 55, no. 4, p. 1869-1887.

Reimer, P. J., Brown, T. A., and Reimer, R. W., 2004, Discussion: reporting and calibration of post-bomb 14C data: Radiocarbon, v. 46, no. 3, p. 1299-1304.

Reyes, A.V. and Clague, J.J., 2004. Stratigraphic evidence for multiple Holocene advances of Lillooet Glacier, southern Coast mountains, British Columbia. *Canadian Journal of Earth Sciences*, *41*(8), pp.903-918.

Reynolds, L. C., and Simms, A. R., 2015, Late Quaternary relative sea level in Southern California and Monterey Bay: Quaternary Science Reviews, v. 126, p. 57-66.

Richards, G., 1985, Fossil Mediterranean molluscs as sea-level indicators: Geological Magazine, v. 122, no. 4, p. 373-381.

Rick, T. C., Erlandson, J. M., Jew, N. P., and Reeder-Myers, L. A., 2013, Archaeological survey, paleogeography, and the search for Late Pleistocene Paleocoastal peoples of Santa Rosa Island, California: Journal of Field Archaeology, v. 38, no. 4, p. 324-331.

Rintoul, W., 1976, Spudding in: Recollections of pioneer days in the California oil fields, California Historical Society.

Rockwell, T. K., Clark, K., Gamble, L., Oskin, M. E., Haaker, E. C., and Kennedy, G. L., 2016, Large Transverse Range Earthquakes Cause Coastal Upheaval near Ventura, Southern California: Bulletin of the Seismological Society of America, v. 106, no. 6, p. 2706-2720.

Rose, N. L., 2008, Quality control in the analysis of lake sediments for spheroidal carbonaceous particles: Limnology and Oceanography-Methods, v. 6, p. 172-179.

-, 2015, Spheroidal Carbonaceous Fly Ash Particles Provide a Globally Synchronous Stratigraphic Marker for the Anthropocene: Environmental Science & Technology, v. 49, no. 7, p. 4155-4162.

Rose, N. L., Jones, V. J., Noon, P. E., Hodgson, D. A., Flower, R. J., and Appleby, P. G., 2012, Long-Range Transport of Pollutants to the Falkland Islands and Antarctica: Evidence from Lake Sediment Fly Ash Particle Records: Environmental Science & Technology, v. 46, no. 18, p. 9881-9889.

Rothwell, R., 1904, The Mineral Industry During 1903: The Engineering and Mining Journal, v. 12.

Ruppel, M., Lund, M. T., Grythe, H., Rose, N. L., Weckstrom, J., and Korhola, A., 2013, Comparison of Spheroidal Carbonaceous Particle Data with Modelled Atmospheric Black Carbon Concentration and Deposition and Air Mass Sources in Northern Europe, 1850-2010: Advances in Meteorology, p. 15.

Ruppel, M. M., Gustafsson, O., Rose, N. L., Pesonen, A., Yang, H., Weckstrom, J., Palonen, V., Oinonen, M. J., and Korhola, A., 2015, Spatial and Temporal Patterns in Black Carbon Deposition to Dated Fennoscandian Arctic Lake Sediments from 1830 to 2010: Environ Sci Technol, v. 49, no. 24, p. 13954-13963.

Rutz, J.J., Steenburgh, W.J. and Ralph, F.M., 2014. Climatological characteristics of atmospheric rivers and their inland penetration over the western United States. *Monthly Weather Review*, *142*(2), pp.905-921.

Ryan, G., 1994. *Climate of Santa Barbara, California*. US Department of Commerce, National Oceanic and Atmospheric Administration, National Weather Service Scientific Services Division, Western Region.

Ryan, K. J., Geist, E. L., Barall, M., and Oglesby, D. D., 2015, Dynamic models of an earthquake and tsunami offshore Ventura, California: Geophysical Research Letters, v. 42, no. 16, p. 6599-6606.

Sadro, S., Gastil-Buhl, M., and Melack, J., 2007, Characterizing patterns of plant distribution in a southern California salt marsh using remotely sensed topographic and hyperspectral data and local tidal fluctuations: Remote Sensing of Environment, v. 110, no. 2, p. 226-239.

Santschi, P. H., Li, Y.-H., Adler, D. M., Amdurer, M., Bell, J., and Nyffeler, U. P., 1983, The relative mobility of natural (Th, Pb and Po) and fallout (Pu, Am, Cs) radionuclides in the coastal marine environment: results from model ecosystems (MERL) and Narragansett Bay: Geochimica et Cosmochimica Acta, v. 47, no. 2, p. 201-210.

Schimmelmann, A., Hendy, I. L., Dunn, L., Pak, D. K., and Lange, C. B., 2013, Revised similar to 2000-year chronostratigraphy of partially varved marine sediment in Santa Barbara Basin, California: Gff, v. 135, no. 3-4, p. 258-264.

Schimmelmann, A., Lange, C. B., Roark, E. B., and Ingram, B. L., 2006, Resources for Paleoceanographic and Paleoclimatic Analysis: A 6,700-Year Stratigraphy and Regional Radiocarbon Reservoir-Age (ΔR) Record Based on Varve Counting and AMS Dating for the Santa Barbara Basin, Offshore California, U.S.A.: Journal of Sedimentary Research, v. 76, no. 1, p. 74-80.

Schmitt, R., Dugan, J., and Adamson, M., 2002, Industrial Activity and Its Socioeconomic Impacts: Oil and Three Coastal California Counties: Camarillo, CA: US Department of the Interior, Minerals Management Service, Pacific OCS Region. OCS Study MMS, v. 49.

Schroeder, I.D., Black, B.A., Sydeman, W.J., Bograd, S.J., Hazen, E.L., Santora, J.A. and Wells, B.K., 2013. The North Pacific High and wintertime pre-conditioning of California current productivity. Geophysical Research Letters, 40(3), pp.541-546.

Schwalbach, J.R. and Gorsline, D.S., 1985. Holocene sediment budgets for the basins of the California continental borderland. *Journal of Sedimentary Research*, *55*(6).

Scott, D. B., Mudie, P. J., and Bradshaw, J. S., 2011, Coastal evolution of Southern California as interpreted from benthic foraminifera, ostracodes, and pollen: Journal of Foraminiferal Research, v. 41, no. 3, p. 285-307.

Shennan, I., 1986, Flandrian sea-level changes in the Fenland. II: Tendencies of sea-level movement, altitudinal changes, and local and regional factors: Journal of Quaternary Science, v. 1, no. 2, p. 155-179.
Shennan, I., Garrett, E., and Barlow, N., 2016, Detection limits of tidal-wetland sequences to identify variable rupture modes of megathrust earthquakes: Quaternary Science Reviews, v. 150, p. 1-30.
Shennan, I., and Horton, B., 2002, Holocene land- and sea-level changes in Great Britain: Journal of Quaternary Science, v. 17, no. 5-6, p. 511-526.
Shimozono, T., Tajima, Y., Kennedy, A. B., Nobuoka, H., Sasaki, J., and Sato, S., 2015, Combined infragravity wave and sea-swell runup over fringing reefs by super typhoon Haiyan: Journal of Geophysical Research-Oceans, v. 120, no. 6, p. 4463-4486.
Shugar, D. H., Walker, I. J., Lian, O. B., Earner, J. B. R., Neudorf, C., McLaren, D., and Fedje, D., 2014, Post-glacial sea-level change along the Pacific coast of North America: Quaternary Science Reviews, v. 97, p. 170-192.
Simkin, T., Tilling, R., Vogt, P., Kirby, S., Kimberly, P., and Stewart, D., 2006, This dynamic planet: World map of volcanoes, earthquakes, impact craters, and plate tectonics: US Geological Survey Geologic Investigations Series Map I-2800, 1 two-sided sheet, scale 1: 30,000,000: SIPRE auger. Jon's Machine Shop (http://jonsmachine. com/), v. 350, p. 99712-91007.
Simms, A., Reynolds, L. C., Bentz, M., Roman, A., Rockwell, T., and Peters, R., 2016, Tectonic Subsidence of California Estuaries Increases Forecasts of Relative Sea-Level Rise: Estuaries and Coasts, v. 39, no. 6, p. 1571-1581.
Simms, A. R., Aryal, N., Yokoyama, Y., Matsuzaki, H., and Dewitt, R., 2009, Insights on a Proposed Mid-Holocene Highstand Along the Northwestern Gulf of Mexico from the Evolution of Small Coastal Ponds: Journal of Sedimentary Research, v. 79, no. 9-10, p. 757-772.
Simms, A. R., Lambeck, K., Purcell, A., Anderson, J. B., and Rodriguez, A. B., 2007, Sea-level history of the Gulf of Mexico since the Last Glacial Maximum with implications for the melting history of the Laurentide Ice Sheet: Quaternary Science Reviews, v. 26, no. 7-8, p. 920-940.
Slade, R. C., 1975, Hydrogeologic investigation of Carpinteria ground water basin, Santa Barbara County, California: University of Southern California.
Sloss, C. R., Jones, B. G., Murray-Wallace, C. V., and McClennen, C. E., 2005, Holocene sea level fluctuations and the sedimentary evolution of a barrier estuary: Lake Illawarra, New South Wales, Australia: Journal of coastal research, v. 21, no. 5, p. 943-959.
Sloss, C. R., Murray-Wallace, C. V., and Jones, B. G., 2007, Holocene sea-level change on the southeast coast of Australia: a review: Holocene, v. 17, no. 7, p. 999-1014.
Sommerfield, C. K., and Lee, H. J., 2003, Magnitude and variability of Holocene sediment accumulation in Santa Monica Bay, California: Marine environmental research, v. 56, no. 1, p. 151-176.
-, 2004, Across-shelf sediment transport since the Last Glacial Maximum, southern California margin: Geology, v. 32, no. 4, p. 345-348.
Sommerfield, C. K., Lee, H. J., and Normark, W. R., 2009, Postglacial sedimentary record of the Southern California continental shelf and slope, Point Conception to Dana Point: Geological Society of America Special Papers, v. 454, p. 89-115.

Sousa, W. P., 1983, Host life history and the effect of parasitic castration on growth: a field study of *Cerithidea californica* Haldeman (Gastropoda: Prosobranchia) and its trematode parasites: Journal of Experimental Marine Biology and Ecology, v. 73, no. 3, p. 273-296.

Spada, G., Antonioli, A., Cianetti, S., and Giunchi, C., 2006, Glacial isostatic adjustment and relative sea-level changes: the role of lithospheric and upper mantle heterogeneities in a 3-D spherical Earth: Geophysical Journal International, v. 165, no. 2, p. 692-702.

Special Research Collections, U. L., 1929, Flight C300, Frame L-49. [Aerial photograph], Fairchild Aerial Surveys, Volume 1:18,000: Santa Barbara, Calif., University of California Santa Barbara

Sperazza, M., Moore, J.N. and Hendrix, M.S., 2004. High-resolution particle size analysis of naturally occurring very fine-grained sediment through laser diffractometry. *Journal of Sedimentary Research, 74*(5), pp.736-743.

Stanley, D. J., and Warne, A. G., 1994, Worldwide initiation of Holocene marine deltas by deceleration of sea-level rise Science, v. 265, no. 5169, p. 228-231.

Steel, E., Simms, A. R., Warrick, J., and Yokoyama, Y., 2016, Highstand shelf fans: The role of buoyancy reversal in the deposition of a new type of shelf sand body: Geological Society of America Bulletin, v. 128, no. 11-12, p. 1717-1724.

Stine, S., 1994. Extreme and persistent drought in California and Patagonia during mediaeval time. *Nature, 369*(6481), p.546.

Stockmarr, J., 1971, Tablets with spores used in absolute pollen analysis: Pollen et spores.

Stockton, G., 1960, La Carpinteria, Carpinteria Valley Historical Society.

Swindles, G. T., Watson, E., Turner, T. E., Galloway, J. M., Hadlari, T., Wheeler, J., and Bacon, K. L., 2015, Spheroidal carbonaceous particles are a defining stratigraphic marker for the Anthropocene: Scientific Reports, v. 5, p. 6.

Takekawa, J., Thorne, K., Buffington, K., Freeman, C., and Block, G., 2014, Evaluation of subterranean subsidence at Seal Beach National Wildlife Refuge: Unpublished Data Summary Report, v. 24.

Toppozada, T. R., Branum, D. M., Reichle, M. S., and Hallstrom, C. L., 2002, San Andreas fault zone, California: M >= 5.5 earthquake history: Bulletin of the Seismological Society of America, v. 92, no. 7, p. 2555-2601.

Tornqvist, T. E., Gonzalez, J. L., Newsom, L. A., van der Borg, K., de Jong, A. F. M., and Kurnik, C. W., 2004, Deciphering Holocene sea-level history on the US Gulf Coast: A high-resolution record from the Mississippi Delta: Geological Society of America Bulletin, v. 116, no. 7-8, p. 1026-1039.

van de Plassche, O., 1986, Sea-level research: a manual for the collection and evaluation of data, Geo Books Norwich, England.

van Geel, B., and Aptroot, A., 2006, Fossil ascomycetes in Quaternary deposits: Nova Hedwigia, v. 82, no. 3-4, p. 313-329.

Viale, M., and Nuñez, M. N., 2011, Climatology of Winter Orographic Precipitation over the Subtropical Central Andes and Associated Synoptic and Regional Characteristics: Journal of Hydrometeorology, v. 12, no. 4, p. 481-507.

Waelbroeck, C., Labeyrie, L., Michel, E., Duplessy, J. C., McManus, J., Lambeck, K., Balbon, E., and Labracherie, M., 2002, Sea-level and deep water temperature changes derived from benthic foraminifera isotopic records: Quaternary Science Reviews, v. 21, no. 1, p. 295-305.

Wagner, J. D. M., 2006, Speleothem record of southern Arizona paleoclimate, 54 to 3.5 ka.
Waliser, D., and Guan, B., 2017, Extreme winds and precipitation during landfall of atmospheric rivers: Nature Geoscience, v. 10, no. 3, p. 179-183.
Wallace, R. E., 1990, The San Andreas fault system, California: US Geological Survey Professional Paper, v. 1515, p. 283.
Warrick, J. A., Hatten, J. A., Pasternack, G. B., Gray, A. B., Goni, M. A., and Wheatcroft, R. A., 2012, The effects of wildfire on the sediment yield of a coastal California watershed: Geological Society of America Bulletin, v. 124, no. 7-8, p. 1130-1146.
Warrick, J. A., Mertes, L. A., Washburn, L., and Siegel, D. A., 2004, A conceptual model for river water and sediment dispersal in the Santa Barbara Channel, California: Continental Shelf Research, v. 24, no. 17, p. 2029-2043.
Warrick, J. A., and Mertes, L. A. K., 2009, Sediment yield from the tectonically active semiarid Western Transverse Ranges of California: Geological Society of America Bulletin, v. 121, no. 7-8, p. 1054-1070.
Warrick, J. A., and Milliman, J. D., 2003, Hyperpycnal sediment discharge from semiarid southern California rivers: Implications for coastal sediment budgets: Geology, v. 31, no. 9, p. 781-784.
Watson, E. B., Wasson, K., Pasternack, G. B., Woolfolk, A., Van Dyke, E., Gray, A. B., Pakenham, A., and Wheatcroft, R. A., 2011, Applications from Paleoecology to Environmental Management and Restoration in a Dynamic Coastal Environment: Restoration Ecology, v. 19, no. 6, p. 765-775.
Weltje, G. J., and Tjallingii, R., 2008, Calibration of XRF core scanners for quantitative geochemical logging of sediment cores: theory and application: Earth and Planetary Science Letters, v. 274, no. 3, p. 423-438.
Westerling, A.L., Hidalgo, H.G., Cayan, D.R. and Swetnam, T.W., 2006. Warming and earlier spring increase western US forest wildfire activity. *science*, *313*(5789), pp.940-943.
Wilson, R., Hemphill-Haley, E., Jaffe, B., Richmond, B., Peters, R., Graehl, N., Kelsey, H., Leeper, R., Watt, S., and McGann, M., 2014, The search for geologic evidence of distant-source tsunamis using new field data in California: Chapter C in The SAFRR (Science Application for Risk Reduction) Tsunami Scenario: US Geological Survey, 2331-1258.
Yamane, M., Yokoyama, Y., Miyairi, Y., Suga, H., Matsuzaki, H., Dunbar, R. B., and Ohkouchi, N., 2014, Compound-specific C14 dating of IDOP expedition 318 core U1357A obtained off the wilkes land coast, Antarctica: Radiocarbon, v. 56, no. 3, p. 1009-1017.
Yokoyama, Y., Koizumi, M., Matsuzaki, H., Miyairi, Y., and Ohkouchi, N., 2010, Developing ultra small-scale radiocarbon sample measurment at the University of Tokyo Radiocarbon, v. 52, no. 2, p. 310-318.
Yokoyama, Y., Miyairi, Y., Matsuzaki, H., and Tsunomori, F., 2007, Relation between acid dissolution time in the vacuum test tube and time required for graphitization for AMS target preparation: Nuclear Instruments & Methods in Physics Research Section B-Beam Interactions with Materials and Atoms, v. 259, no. 1, p. 330-334.
Zedler, J. B., 1996, Coastal mitigation in Southern California: The need for a regional restoration strategy: Ecological Applications, v. 6, no. 1, p. 84-93.
Zhen, L., Saito, Y., Limi, M., Tamura, T., Bing, S., Yulan, Z., Anqing, L., Sieng, S., and Jie, L., 2012, Mid-Holocene mangrove succession and its response to sea-level change in

the upper Mekong River delta, Cambodia: Quaternary Research, v. 78, no. 2, p. 386-399.

Zhu, Y., and Newell, R. E., 1998, A proposed algorithm for moisture fluxes from atmospheric rivers: Monthly Weather Review, v. 126, no. 3, p. 725-735.

Appendix A: List of Supplementary Files

Chapter 2:

-Radiocarbon and RSL data for Southern California and Monterey Bay

-Rejected radiocarbon RSL data

Chapter 3:

-Full grain size statistics for core and modern samples

Chapter 4:

-Full radiocarbon data for Carpinteria Marsh

Chapter 5:

-CM46, 51, 20 grain size, XRF, and isotope data

Appendix B: Chapter 3 Supplementary Figures

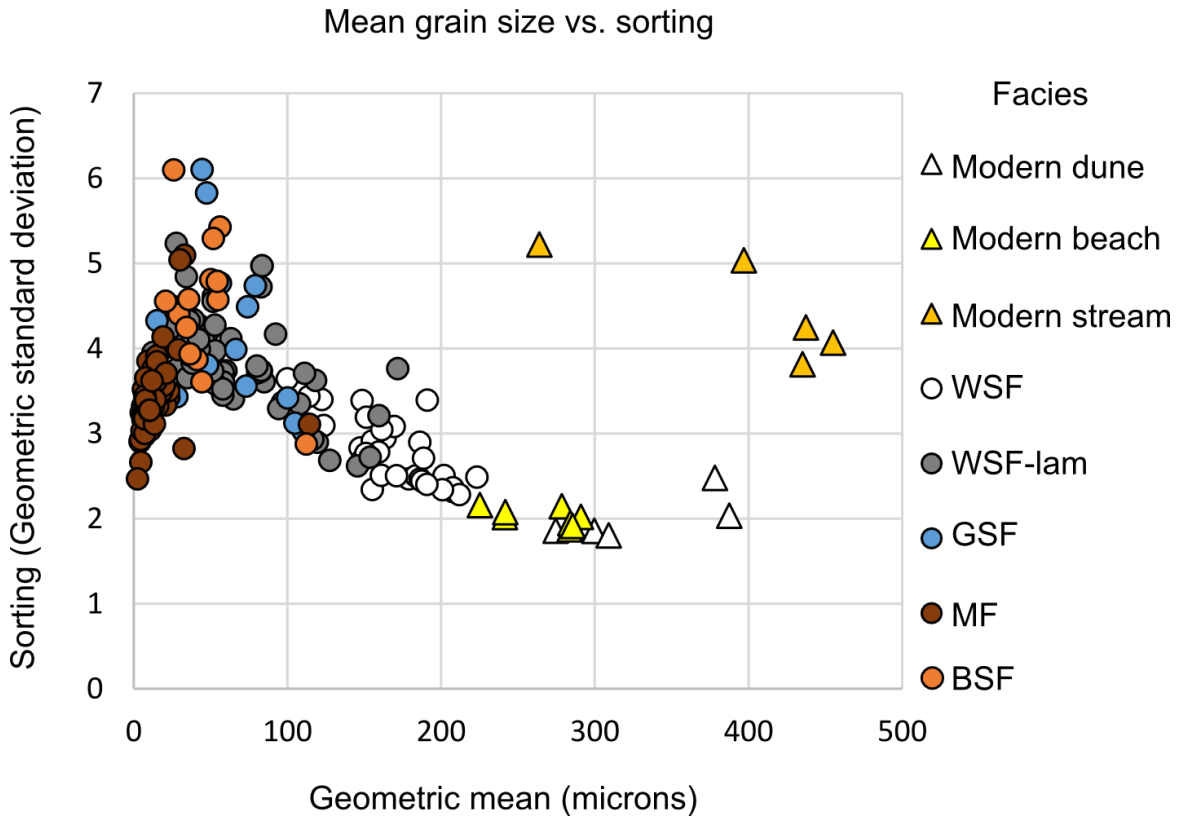


Figure 1. Sedimentary characteristics of facies. Grain size data of four facies and modern environments. Modern samples are sourced from Carpinteria Creek (stream samples), and Carpinteria State Beach (beach and dune samples).

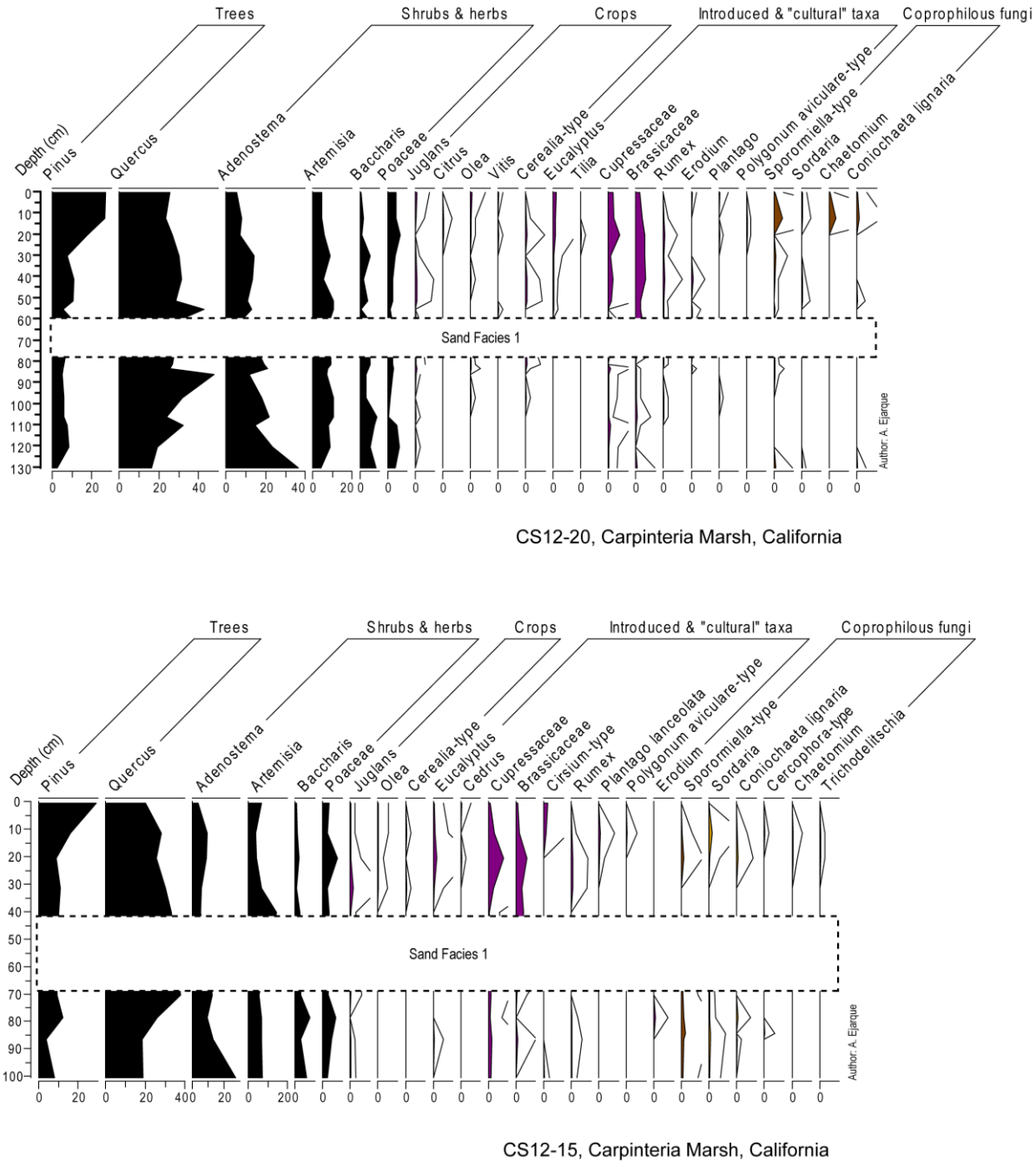


Figure 2. Full pollen diagrams for CM15 (CS12-15) and CM20 (CS12-20), by Ana Ejarque.

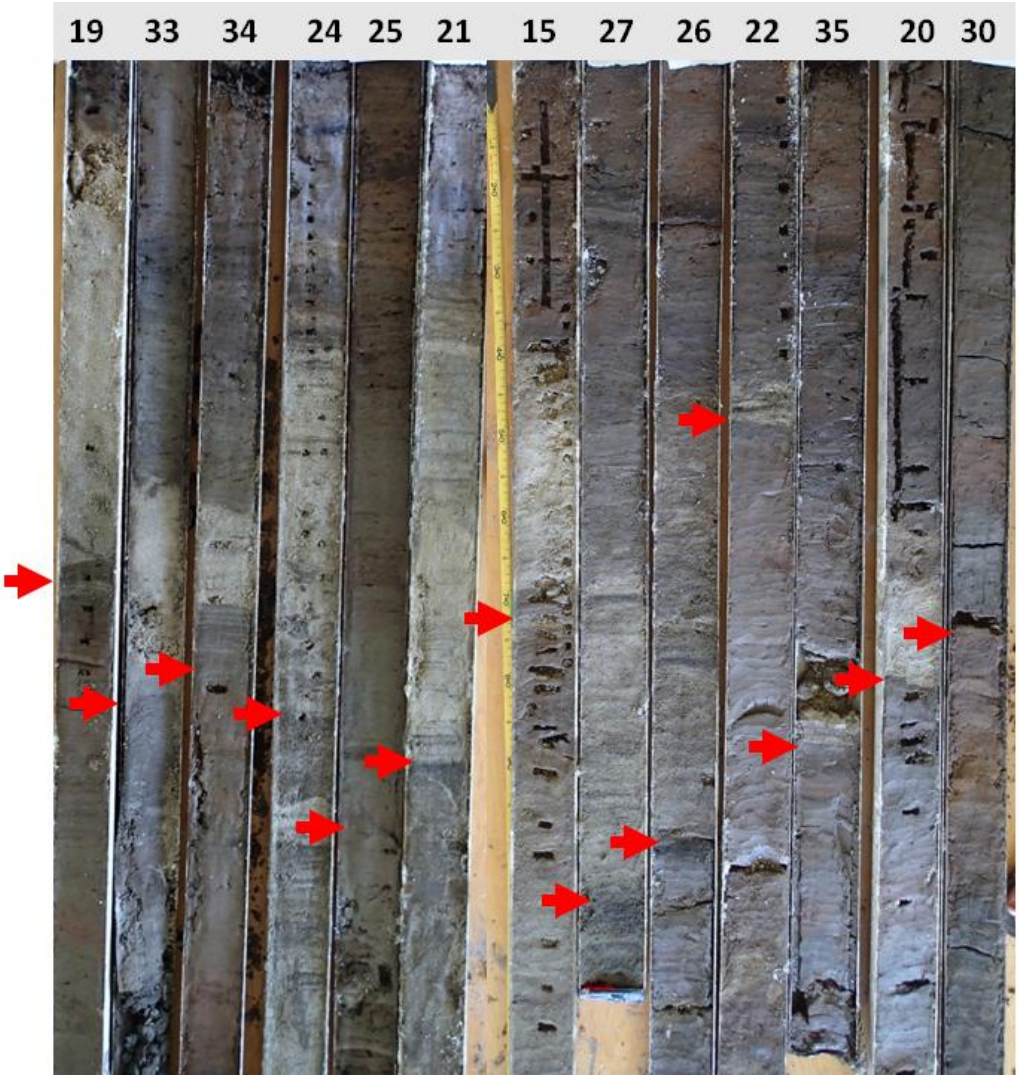


Figure 3. Core photographs showing beds of WSF. Core number is labeled at top of figure. Red arrows indicate erosional or sharp base of WSF bed overlying organic rich MF sediments in most cases. In CM21 and CM 24, the bed of WSF shown overlies SF2.

Appendix C: Carpinteria Radiocarbon Dates

Table of Carpinteria radiocarbon data (full table in supplementary data). Delta R used: 263 +/-77 for bivalves and oyster; 171 +/-154 for Cerithidea following Holmquist et al. 2015. Elevation error for core top elevations measured with lidar is assigned 0.15 (average difference from differential GPS measurement from Sadro et al., 2015). Samples which were removed for analysis are noted in Notes column of supplementary table. Radiocarbon samples with Lab No. starting in "Y" were processed at the Atmospheric and Ocean Research Institute, The University of Tokyo. All others were processed at the University of California Irvine Keck Carbon Cycle AMS Laboratory.

Lab No.	Sample name	Material Description	Core	Sample Depth BGS	Sample Elevation above NAVD88	14C age	14C error	lower cal range BP	upper cal range BP	median probability	Latitude	Longitude
Y-26704	CS12-3-282-sh	art bivalve	3	282	-138.43	1217	22	435	670	556	34.4004	-119.534
Y-26733	CS12-15-123-org	stems/roots and one piece charcoal mud break in SF2	15	123	17.6	19	39	255	-6	80	34.3998	-119.536
115623	CS12-15;40-41cm	Charcoal and insect parts	15	40	100.6	180	20	1	286	183	34.3998	-119.536
115624	CS12-15;69-70cm	Charcoal	15	69	71.6	5170	20	5905	5986	5926	34.3998	-119.536
169345	CS-12-16-117-org .17mgC	plant stem	16	117	41.868	1040	15	929	965	947	34.4037	-119.537
169346	CS-12-16-151-ch	single charcoal fragment	16	151	7.868	1510	20	1342	1515	1388	34.4037	-119.537
169347	CS-12-16-310-org	plant stem	16	310	-151.13	1850	15	1720	1859	1782	34.4037	-119.537
169348	CS-12-16-322-sh	Cerithidea californica	16	322	-163.13	2220	15	1290	1970	1626	34.4037	-119.537
169349	CS-12-16-168-ch .20mgC	multiple charcoal pieces	16	168	-9.132	1405	15	1292	1336	1308	34.4037	-119.537
153252	CS1219-370-ch .11mgC	charcoal	19	370	-202.33	2160	20	2067	2303	2160	34.4027	-119.542
153268	CS1219-400H-ch .28mgC	charcoal	19	400	-232.33	2180	15	2126	2305	2262	34.4027	-119.542
26703	CS12-20-270-sh	ridged bivalve, art	20	270	-111.22	1673	23	779	1152	961	34.4025	-119.54
Y-26706	CS12-20-265-sh	art ridged bivalve	20	265	-106.22	1481	26	635	923	770	34.4025	-119.54
Y-26723	CS12-20-270-sh-1	ridged bivalve	20	270	-111.22	1500	47	633	957	788	34.4025	-119.54
Y-26724	CS12-20-270-sh-2	ridged bivalve	20	270	-111.22	1513	29	651	949	798	34.4025	-119.54
Y-26725	CS12-20-270-sh-13	ridged bivalve	20	270	-111.22	1429	47	560	899	725	34.4025	-119.54
Y-26726	CS12-20-270-sh-15	ridged bivalve	20	270	-111.22	1785	100	797	1305	1075	34.4025	-119.54
Y-26729	CS12-20-270-sh-8	ridged bivalve	20	270	-111.22	1479	33	629	926	769	34.4025	-119.54
Y-26731	CS12-20-270-sh-28	ridged bivalve	20	270	-111.22	1501	31	644	940	788	34.4025	-119.54
Y-26732	CS12-20-270-sh-20	ridged bivalve	20	270	-111.22	1572	34	680	1026	850	34.4025	-119.54
115625	CS12-20;59-60cm	Charcoal	20	59	99.777	255	20	154	421	299	34.4025	-119.54
115626	CS12-20;86-87cm	Insect parts	20	86	72.777	185	20	1	287	181	34.4025	-119.54

153253	CS1220-380-org .029mgC	plant part	20	380	-221.22	2970	110	2855	3389	3134	34.4025	-119.54
Y-26735	CS12-21-272-org	root in mud clast between SF2 upper and lower	21	272	-115.05	510	50	487	645	536	34.4	-119.539
153254	CS1221-400-org	plant part	21	400	-243.05	1915	20	1820	1917	1863	34.4	-119.539
Y-26705	CS12-22-163-sh	art thin bivalve	22	163	-14.528	1426	29	565	893	721	34.4014	-119.538
Y-26737	CSV13-02-100-org	wood, not burnt	25	100	51.238	205	22	1	300	172	34.4003	-119.538
169363	CS-MF14-02-90-sh	oyster shell	31	90	16.2548	1625	15	724	1081	906	34.4033	-119.54
Y-26736	CS15-03-233-org	organic in SF2	41	233	-217.7	1819	27	1633	1824	1761	34.4012	-119.539
169360	CS-15-03-273-sh	limpet	41	273	-257.7	4090	15	3564	3985	3778	34.4012	-119.539
169361	CS-15-03-287-org	plant stem	41	287	-271.7	2275	15	2187	2346	2325	34.4012	-119.539
169362	CS-15-03-95-org	plant parts	41	95	-79.7	590	20	542	645	607	34.4012	-119.539
169339	CS-16-02-85-org	plant stem	43	85	-9.3	885	15	738	900	786	34.4025	-119.534
169340	CS-16-02-94-org .19mgC	plant stem	43	94	-18.3	785	15	681	728	702	34.4025	-119.534
169341	CS-16-02-121-sh	Cerithidea californica	43	121	-45.3	1200	15	334	902	614	34.4025	-119.534
169342	CS-16-02-274-org .24mgC	multiple plant parts	43	274	-198.3	885	15	738	900	786	34.4025	-119.534
169343	CS-16-02-275-org	partially burned stem	43	275	-199.3	835	15	700	781	740	34.4025	-119.534
169344	CS-16-02-281-org	plant stem	43	281	-205.3	1350	20	1266	1303	1288	34.4025	-119.534
Y-26708	GP02-65-755-sh	Cerithidea californica	46	755	-531.11	4038	26	3438	4262	3840	34.3989	-119.536
Y-26709	GP02-111-959-sh	Cerithidea californica	46	959	-735.11	4793	30	4438	5271	4849	34.3989	-119.536
Y-26711	GP02-168-1239-sh	Cerithidea californica	46	1239	-1015.1	6047	38	5930	6634	6293	34.3989	-119.536
Y-26712	GP02-62-745-sh	Cerithidea californica	46	745	-521.11	3737	30	3057	3860	3463	34.3989	-119.536
Y-26713	GP02-63-750-sh	Cerithidea californica	46	750	-526.11	3940	26	3340	4132	3715	34.3989	-119.536
Y-26716	GP02-97-907-sh	Cerithidea californica	46	907	-683.11	4455	33	3978	4811	4399	34.3989	-119.536
Y-26717	GP02-110-959-sh	Cerithidea californica	46	959	-735.11	4838	37	4478	5312	4915	34.3989	-119.536
Y-26718	GP02-161-1207-sh	Cerithidea californica	46	1207	-983.11	5866	28	5732	6418	6094	34.3989	-119.536
Y-26719	GP02-168-1239-sh	Cerithidea californica	46	1239	-1015.1	5929	34	5809	6514	6159	34.3989	-119.536
Y-26722	GP02-92-882-sh	Cerithidea californica	46	882	-658.11	4315	44	3767	4672	4209	34.3989	-119.536
129078	CSRC-01 673 C. californica	Cerithidea californica	46	1130	-906.11	5240	20	4970	5744	5406	34.3989	-119.536
129079	CSRC-02 1224 C. californica	Cerithidea californica	46	1224	-1000.1	5730	25	5612	6270	5953	34.3989	-119.536
129080	CSRC-03 789 C. californica	Cerithidea californica	46	789	-565.11	4020	20	3420	4233	3816	34.3989	-119.536
129081	CSRC-04 904 C. californica	Cerithidea californica	46	904	-680.11	4520	20	4052	4867	4489	34.3989	-119.536
129084	CSRC-05 673 Charcoal	charcoal	46	1130	-906.11	4645	20	5313	5458	5414	34.3989	-119.536
129085	CSRC-06 1224 Charcoal	charcoal	46	1224	-1000.1	5295	20	5994	6179	6083	34.3989	-119.536
129086	CSRC-07 789 Charcoal	charcoal	46	789	-565.11	3615	20	3866	3979	3924	34.3989	-119.536

129087	CSRC-08 904 Charcoal	charcoal	46	904	-680.11	3845	20	4155	4403	4254	34.3989	-119.536
129088	CSRC-09 1369 Charcoal	charcoal	46	1369	-1145.1	5850	20	6636	6734	6671	34.3989	-119.536
129089	CSRC-10 1363 Organics	organics	46	1363	-1139.1	5920	25	6672	6791	6739	34.3989	-119.536
151182	CS1302-568-pp	stem or wood part	46	568	-344.11	2730	20	2776	2862	2819	34.3989	-119.536
151183	CS1302-753-ch	charcoal	46	753	-529.11	3305	20	3475	3580	3524	34.3989	-119.536
151184	CS1302-807-pp	plant part	46	807	-583.11	3785	25	4090	4237	4163	34.3989	-119.536
151214	CS1302-551-cc	Cerithidea Californica shell	46	551	-327.11	1865	20	917	1567	1245	34.3989	-119.536
151185	CS1305-521-pp .10mgC	charcoal	49	521	-299.04	2035	25	1903	2103	1985	34.4011	-119.534
151186	CS1305-654-sd	seed	49	654	-432.04	3015	20	3084	3327	3205	34.4011	-119.534
151187	CS1305-687-pp	plant part	49	687	-465.04	3445	20	3638	3823	3697	34.4011	-119.534
151188	CS1305-828-pp .023mgC	plant part	49	828	-606.04	3960	100	4095	4811	4415	34.4011	-119.534
151189	CS1305-1090-pp .052mgC	plant part	49	1090	-868.04	4560	60	4980	5452	5194	34.4011	-119.534
151190	CS1305-1256-ch	charcoal	49	1256	-1034	5320	25	6002	6184	6091	34.4011	-119.534
151191	CS1305-1407-pp .035mgC	plant part	49	1407	-1185	5910	100	6487	6987	6738	34.4011	-119.534
151192	CS1305-1460-pp .040mgC	plant part	49	1460	-1238	5800	90	6403	6840	6601	34.4011	-119.534
151215	CS1305-928-cc	Cerithidea californica	49	928	-706.04	4430	20	3960	4797	4364	34.4011	-119.534
153269	CS1306-20-57-ch	charcoal	49	667	-445.04	3000	20	3079	3319	3187	34.4011	-119.534
153236	CS1306-40-20	organic	50	1239	-989	5190	20	5912	5989	5940	34.4019	-119.534
153248	CS1306-729-og	organic	50	729	-479	3240	20	3395	3555	3457	34.4019	-119.534
153249	CS1306-1352-ch .12mgC	charcoal	50	1352	-1102	5385	25	6028	6281	6213	34.4019	-119.534
153250	CS1306-1276-ch .23mgC	charcoal	50	1239	-989	5135	20	5765	5931	5909	34.4019	-119.534
153251	CS1306-1259-ch	charcoal	50	667	-417	3000	20	3079	3319	3187	34.4019	-119.534
151193	CS1307-363-pp	plant part	51	363	-113	845	20	702	789	752	34.4025	-119.534
151194	CS1307-663-pp	plant part	51	663	-413	3130	20	3258	3396	3361	34.4025	-119.534
151195	CS1307-718-pp .081mgC	plant part	51	718	-468	3325	30	3476	3635	3557	34.4025	-119.534
151196	CS1307-865-ch	charcoal-single piece, fragmented	51	865	-615	3210	20	3381	3459	3423	34.4025	-119.534
151197	CS1307-927-pp .054mgC	plant part	51	927	-677	3365	45	3477	3705	3607	34.4025	-119.534
151198	CS1307-1049-pp .14mgC	plant part	51	1049	-799	3765	25	4006	4235	4127	34.4025	-119.534
151199	CS1307-1229-pp .21mgC	plant part	51	1229	-979	4335	20	4850	4961	4879	34.4025	-119.534
151200	CS1307-1355-pp .16mgC	plant part	51	1355	-1105	4595	25	5088	5446	5316	34.4025	-119.534
151201	CS1307-1457-pp	plant part	51	1457	-1207	5235	20	5925	6167	5967	34.4025	-119.534

186401	CS12-20-225-org	organic	20	225	-66.223	1395	15	1289	1330	1303	34.4025	-119.54
186402	CS12-20-373-org .15mgC	organic	20	373	-214.22	2240	15	2159	2331	2222	34.4025	-119.54
186403	CS12-15-123-org	stem/roots/char within mud break in SF2	15	123	17.6	130	20	11	270	119	34.3998	-119.536
186404	CS12-15-399-org	wood in MF at base of SF2	15	399	-258.4	1255	20	1097	1275	1221	34.3998	-119.536
186405	CS12-19-129-org .050mgC	15cm above top SF2 in MFB	19	129	38.67	830	30	688	789	737	34.4027	-119.542
186406	CS12-19-67-org	stem, plants growing up from MF to SF1 at base of SF1	19	67	100.67	225	20	1	305	209	34.4027	-119.542
186407	CS12-20-110-org	organic	20	110	48.777	660	15	564	667	598	34.4025	-119.54
186408	CS12-15-224-org	organic	15	224	-83.4	130	20	11	270	119	34.3998	-119.536
186424	CS17-01-137 .058mgC	woody charcoal in TFG	44	137	-80.3	1465	30	1304	1400	1351	34.4022	-119.534
186425	CS17-01-169	organic	44	169	-112.3	910	20	768	913	857	34.4022	-119.534
186426	CS17-01-266 .18mgC	organic	44	266	-209.3	1560	15	1407	1522	1474	34.4022	-119.534
186427	CS17-01-320	organic	44	320	-263.3	1445	15	1304	1363	1332	34.4022	-119.534
186428	CS17-01-377 .17mgC	organic	44	377	-320.3	1590	15	1414	1532	1459	34.4022	-119.534
186429	CS17-01-395	organic	44	395	-338.3	1200	15	1070	1177	1125	34.4022	-119.534
186289	CS12-21-388-sh	cc in lower SF2 just above MF contact within mud clasts	21	388	-231.05	1835	15	900	1540	1213	34.4	-119.539

Appendix D: Carpinteria Core Info

Table of core information. Lat/Long and Elevations were determined using a Topcon differential GPS or with a hand held GPS and Lidar elevation (Lidar corrected for vegetation cover, as described in Sadro et al., 2007). Raw, uncorrected LiDAR elevations were used for cores taken on roads, in tidal channels, or in mudflats (where there is no vegetation cover). The error for Topcon elevations is ~ 0.03m. Depths to top and base of WSF and GSF are also indicated in cm. Elevation error for core top elevations measured with lidar is ~ 0.15m (average difference from differential GPS measurement from Sadro et al., 2015).

Old Core #	New Core #	Latitude	Longitude	Core Top Elevation Relative to NAVD88 (m)	Elevation Source	WSF Top BGS	WSF Base BGS	WSF Thick	GSF Top BGS	GSF Top BGS	Break in GSF	GSF Base BGS
CS12-01	1	34.40129	-119.534	1.3535	Topcon			0	125			>175
CS12-02	2	34.4004	-119.534	1.461	Topcon	49	76	27	145			>76
CS12-03	3	34.40039	-119.534	1.43575	Topcon			0	145			>355
CS12-04	4	34.40052	-119.534	0.734	Topcon	30	30	0	>50			>50
CS12-05	5	34.40049	-119.534	1.3225	Topcon	57	61	4	>85			>85
CS12-06	6	34.40048	-119.534	1.36925	Topcon	60	64	4	>90			>90
CS12-07	7	34.40046	-119.534	1.3705	Topcon			0	>90			>90
CS12-08	8	34.40043	-119.534	1.34375	Topcon	72	76	4	>100			>100
CS12-09	9	34.40041	-119.534	1.41025	Topcon	61	81	20	>90			>90
CS12-10	10	34.40075	-119.535	1.766	Topcon			0	40			>191
CS12-11	11	34.39825	-119.533	1.476	Topcon	65	154	89	154			>190
CS12-12	12	34.39916	-119.532	1.48	Topcon			0	118	135	248	>290
CS12-13	13	34.39965	-119.533	1.446	Topcon			0	86			>202
CS12-14	14	34.39932	-119.535	1.407	Topcon	50	56	6	115			>205
CS12-15	15	34.39983	-119.536	1.406	Topcon	39	68	29	88	212	350	393
CS12-16	16	34.40372	-119.537	1.58868	Lidar corr			0	>380			>380
CS12-17	17	34.40498	-119.541	1.60704	Lidar corr			0	>300			>300
CS12-18	18	34.40495	-119.544	1.7834	Lidar corr			0	100			>115
CS12-19	19	34.40273	-119.542	1.6767	Lidar corr	14	71	57	160			361
CS12-20	20	34.40252	-119.54	1.58777	Lidar corr	61	79	18	133	215	245	367
CS12-21	21	34.40003	-119.539	1.56954	Lidar corr	32	90	58	90	180	267	394
CS12-22	22	34.40135	-119.538	1.48472	Lidar corr	37	47	10	100	185	260	>390
CS12-23	23	34.40117	-119.532	1.82353	Lidar corr			0	>117			
CSV13-01	24	34.39995	-119.539	1.61856	Lidar corr	40	62	22	62	190	250	>263
CSV13-02	25	34.40035	-119.538	1.51238	Lidar corr	58	98	40	155	235		>295
CSV13-03	26	34.40071	-119.538	1.484	Topcon	42	97	55	152	202		250
CSV13-04	27	34.40117	-119.537	1.5399	Lidar corr	33	66	33	66			>267
CSV13-05	28	34.40193	-119.536	1.44046	Lidar corr			0	80			>130
CSV13-06	29	34.40252	-119.535	1.58378	Lidar corr			0	>100			>100
CSMF14-01	30	34.40308	-119.54	1.121871	Lidar-.11	80	81	1	81			>186

CSMF14-02	31	34.40325	-119.54	1.062548	Lidar Raw			0	105			>186
CSMF14-03	32	34.4035	-119.539	1.239451	Lidar -.11			0	102			>195
CSV14-01	33	34.40198	-119.541	1.192049	Lidar-.11	43	80	37	80	105		>187
CSV14-02	34	34.4023	-119.541	1.57307	Lidar corr	60	85	25	138			>240
CSV14-03	35	34.40292	-119.54	1.51014	Lidar corr	81	85	4	>175			>175
CSV14-04	36	34.4032	-119.539	1.525031	Lidar -.11			0	135			>180
CSV14-05	37	34.40372	-119.539	1.256495	Lidar -.11			0	152			>234
CSV14-06	38	34.40415	-119.538	1.55258	Lidar corr			0	>273			>273
CS15-01	39	34.40242	-119.541	1.5743	Lidar corr	10	67	57	156			>237
CS15-02	40	34.40214	-119.538	0.313	New Topcon		0	>				
CS15-03	41	34.40117	-119.539	0.153	New Topcon		0	<	60	285		
CS16-01	42	34.40261	-119.534	0.797	Topcon			0	>236			>236
CS16-02	43	34.40254	-119.534	0.757	Topcon			0	277	365		>371
CS17-01	44	34.40221	-119.534	0.567	Topcon			0	60	205	242	375
CSGP13-01	45	34.39896	-119.536	2.284	Topcon			0	<			
CSGP13-02	46	34.39894	-119.536	2.238874	Lidar Raw			0	<457			552
CSGP13-03	47	34.39953	-119.535	2.312425	Lidar Raw			0	<			
CSGP13-04	48	34.40031	-119.535	2.425349	Lidar Raw			0	<			<
CSGP13-05	49	34.40107	-119.534	2.21963	Lidar Raw			0	<457			610
CSGP13-06	50	34.40193	-119.534	2.5	Estimate Lidar		0	<				
CSGP13-07	51	34.40254	-119.534	2.5	Estimate Lidar		0	<		823		

Appendix E: Chapter 4 Discussion on Alternatives to subsidence

Large flood events are recorded in the Santa Barbara Channel sedimentary record at 1215 and 1339 cal years BP (Hendy et al., 2013), both of which may overlap with the emplacement of the upper subtidal sands in Carpinteria Marsh. However, the sand above the CSS contains bioturbation, variable sedimentary structures, and radiocarbon dates which span 500 years of deposition, indicating it represents a period of long-lasting environmental change, not a single event. Additionally, if it were storm driven deposition, the repetition of flood layers in the Santa Barbara Basin would suggest we should see multiple overwash events in the deeper cores, which we do not.

Tidal channel, mouth migration, or a transgressing shoreline would be expected to erode progressively through the marsh. For example, a transgressing shoreline would be expected to be more erosive ocean ward and less erosive landward, therefore being underlain by ages that young landward. Instead we see variable ages underlying the upper subtidal sand deposit, with no clear pattern relative to geography.

The erosion/non-deposition below the candidate subsidence contact could also represent a climate change that decreased sedimentation to the marsh for ~2000 years, before abruptly restarting sedimentation at 1.0 ka. At least four small streams pre-historically drained into Carpinteria marsh—a hiatus in sediment deposition by these streams would require all entering streams to avulse away from the marsh at once, which seems unlikely. If a large scale shift in climate were responsible, we would expect to see similar, contemporaneous responses from other estuaries in southern California—which does not appear to be the case from existing records (Cole and Wahl, 2000; Ejarque et al., 2015; Lohmar et al., 1980).

Finally, the contact at the CSS could be attributed to abrupt breaching of a sandy barrier, which previously sheltered the estuary from marine influence (Nelson, 1992). Any scenario that does not call on tectonic subsidence, such as this and all mentioned previously, would require that the mud below the CSS was deposited ~1-3 m below MSL to accommodate infilling after a barrier breach. However, geochemical data and the presence of *C. californica* suggest that the mud was deposited at or above MSL. Additionally, the environmental change represented by the CSS appears to be laterally continuous and synchronous across at least the entire modern day marsh, and possibly beyond its present boundaries, which would be difficult to accomplish with a single barrier breach. Therefore, we argue that abrupt subsidence at 1.0 ka is the most likely cause of the stratigraphic boundary marked by the CSS.